Self-Assembly and High-Rate Production of Colloids and Microprisms

by

Joseph A. Ferrar

A dissertation submitted in partial fulfillment
of the requirements for the degree of
Doctor of Philosophy
(Chemical Engineering)
in the University of Michigan
2017

Doctoral Committee:

Professor Michael J. Solomon, Chair
Professor L. Jay Guo
Professor Ronald G. Larson
Assistant Professor Xiaoming Mao

Dedication

To my mother and father, whose sacrifice and love have made this work possible

Acknowledgements

There are several people who have made this journey possible, whom I will forever be indebted too, and who I am grateful for the opportunity to acknowledge and thank.

First and foremost, I would like to thank my research advisor, Prof. Mike Solomon. Mike cared deeply about my professional development. His selfless contribution of his own time, effort, and resources in this area leave me humbled and forever grateful for all he has done for me, from permitting me to experience an industrial internship, to working with me numerous times in both 1-on-1 and group settings to develop both my technical and soft skills. Mike is uncommonly human and compassionate, and he put me in positions to capitalize on my strengths and develop my weaknesses. I am forever grateful for having had the opportunity to be his student and to have learned so much for him.

I would also like to thank my research collaborators. Asst. Prof. Xiaoming Mao, her graduate student Deshpreet Bedi, and her undergraduate student Shangnan Zhou are all phenomenal people and scientists to work with, and our complimentary technical skills were always mutually recognized and appreciated. Our collaboration yielded many exciting results, many of which are shared in chapter two of this dissertation. I want to thank my other committee members, Prof. Ron Larson and Prof. L. Jay Guo. Prof. Larson offered invaluable insights several times during my time at Michigan, and his influence and ideas are prominent in chapters two and four of this work. Discussing my results with Prof. Guo imparted broad

perspective to me that helped shape the written narratives of this dissertation. I also want to thank my labmate, Yanliang Liu, both as a collaborator and friend. Yan lent invaluable polymer science knowledge and intuition to our collaboration, but more importantly, she lent endless energy and drive to make our project successful. Her optimism was the perfect and much needed balance to my grounded pragmatism. Eric Viges's abilities and patience during our collaboration are also greatly appreciated; chapter four of this work would not be possible without both. Finally, my Genentech manager, Dennis Leung, was a phenomenal mentor. Dennis imparted both technical knowledge and honest, straightforward career advice, which proved invaluable during my job search and will continue to aid me in my industry career.

I also want to thank my Michigan ChE friends, particularly Megan Szakasits, who helped me look forward to coming into the lab each day, even when the temperatures were cold and the work was difficult, Aayush Shah, who showed me how to be a graduate student and may be the one person who appreciates Grizzly Peak as much as I do, Mahesh Ganesan, who is the definition of the words "good guy" and the best person you could ever get a beer with, and Youngri Kim, Ryan Franck, and Allison Franck, who were all friends when I needed one the most.

Finally, I want to thank my parents and my brother. My parents have sacrificed and given whatever has been necessary, without hesitation, for me to have opportunity in my life. All three have set an example for how to live life with integrity, overcome challenges, and selflessly give to those you love. My family has been there for me when I needed them the most, and I am truly fortunate to have them.

Thank you so much to all!

Table of Contents

List of Figures

List of Tables

Abstract

This dissertation examines the self-assembly of colloidal spheres at a ITO-coated glass substrate under an applied field, and also of thin, equilateral triangle microprisms at a flat air-water interface. Additionally, the dissertation also demonstrates a new two-step, continuous process for the fabrication of gram-scale quantities of colloidal ellipsoids in a single day of processing. The self-assembly of both colloids and microprisms has application for the design of new materials. Specifically, 3D colloidal crystals possess unique optical and photonic properties, and 2D open networks self-assembled from microprisms at fluid-fluid interfaces possess voids that can generate useful mechanical properties. High-rate, continuous processing of colloidal ellipsoids supports experimental studies of the self-assembly of colloidal gels, suspensions, and crystals.

The kinetics of direct current electric field-assisted assembly of colloidal spheres into crystal and glass structures are measured through a novel combination of confocal microscopy and image analysis. The kinetics of electrophoretic particle deposition in the electric field and subsequent osmotic pressure-driven relaxation upon removal of the field are characterized by measuring the spatiotemporal evolution of the colloidal volume fraction ($\phi(z,t)$) in the thin, 1 mm gap between parallel, transparent electrodes. Particle deposition occurs on the time-scale of hours; such time scales yield dense sediments tens of microns thick, and the particle volume fraction at the glass electrode substrate, $\phi(z=0,t)$, increases exponentially in time. At low Peclet numbers (Pe ~ 0.2), crystallinity is observed to propagate from the electrode surface at rates of

several hundred nm min^{-1}. Particle relaxation, which is driven by gradients in osmotic pressure between the dense sediment and the bulk fluid, occurs rapidly at early times and then proceeds very slowly after the initial tens of minutes; thus, $\phi(z=0,t)$ decays exponentially in time and is measured for the initial 90 minutes of relaxation, at which time a plateau in $\phi(z=0,t)$ is generally observed. $\phi(z,t)$ is then modeled with a one-dimensional colloidal transport model adapted from the sedimentation literature. Validation of the model at low Peclet numbers (Pe ~ 0.2) allows for predictions of the crystal growth rates, which propagate as a characteristic of constant colloidal volume fraction, consistent with an equilibrium crystalline phase transition. The model serves as a design equation for applications that make use of reconfigurable colloidal assembly.

The capillary-driven binding between thin, equilateral triangle microprisms (edge length, L, = 120 μm, thickness, T, varying between 2 and 20 μm) is observed at a flat air-water interface. Thin prisms ($T/L \leq 1/10$) are physically bowed, and interface-prism contact line pinning results in a capillary hexapolar interaction. Additionally, bowing yields two distinct polarity states; the prisms reside with the centers of mass either above or below the interface, depending on whether the bowed surface is concave up or down. The coupling of prism polarity and the capillary hexapole results in a tip-to-tip binding trajectory for pair binding prisms with the same polarity, and a tip-to-midpoint edge binding trajectory for pair binding prisms with the opposite polarity. Thicker prisms (T/L = 1/5) are not bowed, do not possess a capillary hexapole, and do not exhibit polarity. Prisms of all thicknesses self-assemble into open networks, with void structures that could be used to generate useful mechanical properties.

Finally, monodisperse colloidal ellipsoids of aspect ratio up to 4.32 $\pm$ 0.50 are fabricated via a two-step, continuous process at rates of 1.27 g per day, a 20x improvement on best-reported particle quantity yields from the traditional batch fabrication process. The first step continuously cures aqueous solutions poly(vinyl alcohol) (PVA) and polystyrene (PS) colloidal spheres into colloid-embedded PVA film (~150 μm thick). The second step continuously stretches the spheres and film, at temperatures exceeding their glass-transition temperature, via uniaxial extension between two cylindrical rollers. The order of magnitude increase in particle production rate will allow new avenues for functional characterization of gels, suspensions, and crystals comprised of colloidal ellipsoids.

Chapter 1

Introduction

1.1 Fundamentals of colloidal science: Brownian motion and pair potentials

Colloidal suspensions consist of particles that (a) range in size from ~ 10 nm – 5 μm and (b) are dispersed in a fluid medium. This particle size scale is not defined arbitrarily; rather, its bounds encompass particles small enough to exhibit Brownian motion, the thermally-driven diffusion of the particle over its own length scale, and yet sufficiently large to be solely governed by Newtonian mechanics. [1,2] Colloids interact via attractive van der Waal and depletion interactions and repulsive electrostatic interactions, whose aggregate effect may be quantified through the calculation of particle pair potentials. Pair potentials are primarily set by the material properties of the particles and solvent (as well as the size and shape of the particles), though the potentials may be selectively tuned via addition of surfactant stabilizers and dissolved electrolytes to the suspension. [3] Tuning pair potentials is essential in the formulation of industrial colloidal products. Numerous microbicide sprays and solutions, pharmaceutical nanosuspensions, paints and coatings, and consumer products are inherently colloidal systems whose stability and efficacy requires sufficient electrostatic and steric hindrance to particle agglomeration and phase separation. [4]

1.2 Colloidal assembly and crystalline phase transitions at equilibrium

In addition to serving as active ingredients in industrial formulations, colloidal particles may also act as building blocks that self-assemble into complex, macroscopic structures such as gels [5,6], glasses [7-9] and ordered crystals [10-12]. Such structures possess unique properties that are of interest in commercial applications. For example, colloidal gels support large yield stresses and find application in consumer products and advanced materials. [13-17] Colloidal crystals assembled from particles in specific size ranges possess photonic bandgaps and yield optical properties, such as structural color, owing to the Bragg diffraction of incident light. [18-20]

Crystalline phase transitions are a function of the suspension's thermodynamic state variables. Experimentally, a pragmatic variable to tune is a liquid suspension's colloidal volume fraction (ϕ), which, at constant temperature and volume, sets the suspension's osmotic pressure. Both simulations and experimental observations show that colloids with hard sphere interactions possess a fluid state at $\phi < 0.494$, a coexistence of fluid and crystalline states from $0.494 \leq \phi \leq 0.545$ and a fully crystalline state at $\phi > 0.545$. Experimentally, a fluid-to-glass transition may be observed beginning around $\phi \sim 0.58$. This glass transition is not an equilibrium phase, but rather a kinetically-arrested state that arises when equilibration is suppressed through particle jamming. [7,10,21] The addition of attractive, repulsive, and anisotropic pair interactions shifts the onset of phase transitions and makes phase behavior both richer and more complex. [22-26]

1.2.1 Field-assisted, reversible self-assembly of ordered colloidal crystals

Experimental studies of phase behavior at equilibrium are challenging due to the difficulty in dispersing particles at high concentration and particle jamming, which significantly

retards the kinetics of crystallization in homogeneous, dense suspensions. Alternatively to generating phase equilibrium under quiescent conditions, phase transitions may also be induced through application of external fields, such as gravitational [27-32], shear [33,34], and electric fields [3,35-40] to dilute colloidal suspensions. Such external fields act to induce ordered phase transitions through a variety of mechanisms.

In this dissertation, we will specifically explore one field-assisted crystallization mechanism: the concentration of initially dilute colloids, by one-dimensional convective transport, to the volume fraction needed for a crystalline phase transition to occur. The simplest example of this convection-induced crystallization is colloidal sedimentation in Earth's gravitational field; dilute colloids with a finite reduced mass settle into dense, crystalline sediments under the action of gravity. [27-32] Analogously, direct current electric fields are also capable of concentrating initially dilute colloids via electrophoresis, which is the migration of a charged species (in this case, the species is a colloidal particle) to an electrode of an opposite charge. [39-42] DC electric fields possess several advantages from a self-assembly perspective as compared to gravitational fields, all of which stem from the relative ease with which the strength and orientation of the electric field may be controlled. For example, the rate of particle convection, which determines the kinetics of crystal growth, may be controlled with a DC electric field by simply altering the applied current through the solution. To achieve the same control in gravitational sedimentation requires changing the size and/or materials of the colloids.

Additionally, DC electric fields yield self-assembly that is reversible; that is, application of a DC field to a dilute suspension yields a colloidal crystal, and subsequent removal of the DC field results in melting of the crystal back towards the dilute, fluid phase due to osmotic pressure gradients that arise during assembly. [36,43,44,] The ease with which a DC electric field's strength

and orientation may be controlled (literally, with the push of a button) make reversible assemblies pragmatically achievable in most cases.

Reversible colloidal assemblies find utility in applications where the unique properties of a colloidal crystal are desired at some times, but not at others. For example, paints or coatings may possess structural iridescence upon crystallization of their dispersed colloids, and opacity upon reversal of the crystallization. [44] Similar technologies have already demonstrated commercial utility in electronic inks and smart windows, which reflect or filter incident light with dense colloidal sediments reversibly assembled using low power, DC electric fields. [45,46]

In the design of such applications, an essential parameter that must be characterized is the rate at which such properties are switched between "on" and "off" state. Scientifically, characterization of this design parameter requires either measurement or modeling of the kinetics of reversible fluid-crystalline phase transitions. Until now, literature has lacked rigorous kinetic studies of DC electric field-assisted assembly; there are a few reported experimental measurements of the times needed to form steady-state crystals, [39,42] but little exists in the way of time-evolved measurements of crystal growth as a function of electric field strength, and, to our knowledge, no attempts have been made to model these kinetics. Chapter 2 of this dissertation reparametrizes a convection-diffusion model from the sedimentation literature to predict the kinetics of assembly with a DC electric field and further validates this model with rigorous experimental measurements using confocal microscopy.

1.3 Two-dimensional open networks

The assemblies discussed to this point are 3D structures formed in bulk solution, whose scientific and technological merit resides in their optical and photonic properties. There also exist a family of 2D structures called open networks, which are space spanning lattices that contain pores and voids, that possess enhanced mechanical and acoustic properties. For example, the ordered kagome lattice is an open structure formed from triangular building blocks that contains repeating hexagonal voids. The vibrational modes of the lattices bonds make the structure mechanically rigid and also capable of propagating sound waves, which may be exploited through reduction of turbulent drag. [47-49] A slight angular twist of the kagome lattice's bonds yield an open structure with a negative Poisson's ratio, which owes to internal buckling of the network's building block bonds when subjected to uniaxial planar compression. [50]

An open network's voids need not be regular or repeating for the network to possess enhanced mechanics. "Disordered" open networks – porous 2D lattices whose voids are variable in size and shape – assembled from capillary-driven attractions of colloidal ellipsoids at a fluid-fluid interface are approximately an order of magnitude more rigid than are close-packed arrays of colloidal spheres across a range of particle volume fractions. [51] Thus, capillary interactions at fluid-fluid interfaces represent a path to self-assembly of open networks from particle building blocks and are subsequently discussed in detail. [52,53]

1.3.1 Fluid-fluid interfaces as 2D templates for self-assembly of open networks

When a particle is placed at the interface between two immiscible fluids, the interface curves around the surface of the particle due to capillary action. This interface curvature comes

at an energetic cost, and thus particles at interfaces attract and bind in order to minimize both interface curvature and free energy. At particle size scales below one millimeter, calculation of the Bond number shows that gravitational forces are weak and capillary interactions dominate. Van der Waal and electrostatic interactions still have a significant effect on colloidal pair interactions at interfaces. [54,55,51,56,57]

1.3.2 Capillary interaction anisotropy

Capillary-driven attractions are long range (extending out to hundreds of μm), and their direction and strength are set by the material properties and geometry of the particle and interface. [54,57-59] For example, differences in colloidal pair binding can be observed at an air-water vs. an oil-water water interface due to differences in wetting of the particle surface and in the distribution of electrostatic interactions. Colloidal polystyrene ellipsoids form percolating open networks at an oil-water interface, and denser open networks without percolation at an air-water interface. Silica ellipsoids at an oil-water interface stack in a side-side conformation to form an even denser network. [51,60,61] These observations also illustrate the effect of particle shape on capillary-driven attraction; isotropic colloidal spheres interact with isotropic capillary interactions, and thus spheres self-assemble into close-packed structures with hexagonal packing (identical packing to that observed in planar slices of FCC and HCP unit cells). [62]

On the other hand, the anisotropic shape of the ellipsoid yields asymmetry in interface curvature around the surface of the ellipsoid, resulting in asymmetric capillary interactions. Specifically, ellipsoids possess a capillary quadrupole: the interface curves in opposite directions at the tips and sides of the ellipsoids, resulting in two symmetric poles at the ellipsoid tips and

two other symmetric poles at the ellipsoid sides. Because the interface curves in opposite directions at the tips and sides, interface curvature is minimized only by tip-tip and side-side attraction and binding; tip-side interactions are repulsive, and thus tip-side bonds are not observed. [56,59,60]

1.3.3 Microfabricated particles for enhanced control of shape anisotropy

Particle shape is difficult to control at the colloidal scale, and thus, so is capillary-anisotropy. More precise 2D control of particle shape is possible with clean room photolithography, a process by which photoresist is UV-cured into 2D patterns with ~10 μm resolution and with thicknesses ranging between a few and a few hundred microns. [56,59,63] Families of right cylinders, tens of microns long with aspect ratios (defined as the ratio of length of the cylinder's curved sides to the diameter of its flat ends) varying between 0.2 and 4.0, were fabricated via photolithographic processing of epoxy resin (SU-8 photoresist), and as observed with colloidal ellipsoids, capillary quadrapoles are induced at the curved sides and flat ends of the cylinders.

The cylinder's aspect ratio determines the strength of capillary attractions at its flat ends and curved sides. Specifically, the square root of the ratio of capillary-generated excess interface surface area at the cylinder's flat ends to its curved sides is equal to the cylinder aspect ratio; qualitatively, this means a higher amount of interface curvature, and thus stronger capillary attractions are generated, at whichever particle edge (either the flat ends or the curved sides) is shorter. Thus, control over end-to-end vs. side-to-side attraction and binding is achieved by varying the cylinder aspect ratio. [56] In addition to quadrapoles, more complex shapes and

interactions are possible through microfabrication. A combination of photolithography and polymer molding yields hexagram prisms which interact via a dodecapole between the hexagon's six tips and six indentations. Homogeneous hexagrams exhibit a mix of tip-tip and tip-flat edge binding. Variation of the hexagram composition through polymer molding offers precise control of particle wetting, and tip-flat edge binding may be eliminated. [63]

The enhanced control of complex capillary anisotropy afforded by microfabrication may yield the ability to target specific types of open network structures described above. In Chapter 3 of this dissertation, we explore capillary-driven binding thin, equilateral triangle prisms – the particle building blocks of the ordered kagome lattice – at a flat air-water interface.

1.4 Extending particle shape-anisotropy to colloids in bulk solution

The complex structures afforded by anisotropic pair interactions are demonstrated by the 2D open networks described above. The merits of particle anisotropy are also evident when studying colloids in bulk solution. In the realm of colloidal self-assembly, isotropic spheres are limited to forming simple face-centered and body-centered cubic (FCC and BCC) unit cells. [7,11,62] Anisotropic colloids self-assemble into more complex equilibrium structures; specifically, colloidal ellipsoids access a body-centered tetragonal (BCT) unit cell and have been predicted to be able to access a highly dense simple monoclinic (mc2) unit cell. [39,64] Similar unit cells from anisotropic particles exist in nature and produce complex structural iridescence, as seen in butterfly wings and in the camouflage of insects and aquatic species. [20] Thus, self-assembly of synthetic particles with shape anisotropy may result in biomimicry of such complex scattering patterns, which would likely find utility in optical and photonic applications. [18] Beyond dense unit cells, colloidal ellipsoids are likely more efficient gelators than colloidal spheres, and thus

better candidates to achieve minimal gelation, as suggested by experimental comparisons of the yield stresses supported by gelled colloidal spheres and ellipsoids. [15,16] Additionally, gelled and suspended anisotropic colloidal rods and ellipsoids serve as model systems of commercial soft matter systems, such as consumer products. [8]

1.4.1 Challenge in experimental studies of colloidal ellipsoids: Low particle yields

Traditionally, colloidal ellipsoids are fabricated by a series of batch processes. [16,24,39,51,60,61,65-68] Briefly, colloidal spheres are cured into a polymer matrix over the course of several days. The particles and matrix are then heated until both undergo a glass transition, and are subsequently stretched via uniaxial extension between pairs of clamps, which stretches the spherical colloids into a prolate ellipsoidal geometry. The particle-laden film is held under tension as it cools back to room temperature, in order to lock in the ellipsoidal shape. Particle aspect ratios between 1 and ~10 are achieved by means of this synthesis. This series of batch processes suffers from low particle quantity yields. At best, 200 mg of ellipsoids are produced over a 3-day batch processing period, yielding 67 mg of ellipsoids per day. [51] Additionally, most soft matter research groups fall short of these yields by as much as a factor of ten, due to equipment requirements and processing knowledge needed to achieve these yields.

This rate of colloidal ellipsoid fabrication is sufficient for studies of self-assembly, where only small, dilute sample volumes are needed. For characterization of rheological properties of minimal gels and dense dispersions of monodisperse colloidal ellipsoids, however, at least an order of magnitude increase in colloidal ellipsoid yield is required. Such an increase in production rate would also accelerate experimental progress in self-assembly studies, as less time

and resources would be required for particle fabrication. In chapter 4, we describe a two-step, continuous colloidal ellipsoid fabrication process, which achieves this order of magnitude scale-up in particle yield.

1.5 Organization of the dissertation

This dissertation explores self-assembly at two different particle size scales, the colloidal scale in bulk solution and the microscale scale at an air-water interface, and concludes by characterizing bulk polymer film curing and stretching mechanics to fabricate large quantities of colloidal ellipsoids.

In chapter 2, we characterize the kinetics of an established colloidal self-assembly process: the self-assembly of initially dilute colloidal spheres in DC electric fields. The kinetics of particle deposition in the electric field and relaxation upon removal of the electric field are measured through a novel combination of confocal microscopy and image analysis, and the rate of crystallinity propagation is measured by empirically tracking the time-evolved, 1D-evolution of a crystalline front. Both the kinetics of particle motion and crystallinity propagation are modeled through adaptation of a 1D convection-diffusion model from the sedimentation literature, and through literature reports of equilibrium phase behavior of our experimental poly(methyl methacrylate) (PMMA) colloid and cyclohexyl bromide (CHB)/decalin solvent system.

In chapter 3, we explore the capillary-driven binding of thin, equilateral triangle prisms at a flat air-water interface. Equilateral triangles are the fundamental building block of the ordered kagome lattice, and while self-assembly of the kagome lattice is found to be beyond our current

capabilities, unexpected and informative particle mechanics and pair potentials are observed. Specifically, the thinnest prisms (with thickness to length ratios of 1/10 or less) are physically bowed and exhibit a capillary hexapole, which result in two distinct pairwise binding trajectories. The prisms self-assemble into “disordered” open networks, with voids indicative of structural rigidity.

In chapter four, we describe a two-step, continuous colloidal ellipsoid fabrication process, which we use to produce 850 mg of sulfate-modified polystyrene (PS) colloidal ellipsoids of aspect ratios up to 4.32 ± 0.50 over 16 hours of processing – a 24-hour production rate of 1.27 g of ellipsoids. The first step continuously cures polystyrene spheres into a poly(vinyl alcohol) (PVA) matrix, and the second step continuously stretches the film and particles by uniaxial extension between two rotating cylinders at strains up to 7.8. Such quantity yields represent greater than an order of magnitude increase from traditional batch processing, and make possible comprehensive, rheological studies of minimal gels of colloidal ellipsoids. Additionally, this new semi-continuous process is inherently scalable.

We conclude by summarizing our results and suggesting future research directions to build upon these findings.

1.6 References

1. Israelachvili, J. N. *Intermolecular and Surface Forces, Third Edition* (Academic Press, 2011).
2. Russel, W. B., Saville, D. A. & Schowalter, W. R. *Colloidal Dispersions (Cambridge Monographs on Mechanics)* (Cambridge University Press, 1992).
3. Leunissen, M. E. Manipulating colloids with charges and electric fields. (2007).
4. Dong, J. et al. Effect of Triton X-100 on the stability of aqueous dispersions of copper phthalocyanine pigment nanoparticles. *Journal of Colloid and Interface Science* **362**, 33-41 (2011).
5. Eberle, A. P. R., Wagner, N. J. & Casta√±eda-Priego, R. Dynamical Arrest Transition in Nanoparticle Dispersions with Short-Range Interactions. *Physical Review Letters Phys. Rev. Lett. PRL* **106**, 105704 (2011).
6. Emanuela, Z. Colloidal gels: equilibrium and non-equilibrium routes. *Journal of Physics: Condensed Matter* **19**, 323101 (2007).
7. Pusey, P. N. et al. Hard spheres: crystallization and glass formation. *Philosophical Transactions of the Royal Society of London A: Mathematical, Physical and Engineering Sciences* **367**, 4993-5011 (2009).
8. Solomon, M. J. & Spicer, P. T. Microstructural regimes of colloidal rod suspensions, gels, and glasses. *Soft Matter Soft Matter* **6**, 1391-1400 (2010).
9. Wilkins, G. M. H., Spicer, P. T. & Solomon, M. J. Colloidal System To Explore Structural and Dynamical Transitions in Rod Networks, Gels, and Glasses. *Langmuir Langmuir* **25**, 8951-8959 (2009).
10. Cheng, Z. et al. Phase diagram of hard spheres. *Materials & Design* **22**, 529-534 (2001).
11. Pusey, P. N. & van, M., W. Phase behaviour of concentrated suspensions of nearly hard colloidal spheres. *Nature* **320**, 340-342 (1986).
12. Whitesides, G. M. & Grzybowski, B. Self-Assembly at All Scales. *Science* **295**, 2418-2421 (2002).
13. Lu, P. J. et al. Gelation of particles with short-range attraction. *Nature* **453**, 499-503 (2008).
14. Hsiao, L. C., Newman, R. S., Glotzer, S. C. & Solomon, M. J. Role of isostaticity and load-bearing microstructure in the elasticity of yielded colloidal gels. *Proceedings of the National Academy of Sciences* **109**, 16029-16034 (2012).
15. Manley, S. et al. Limits to Gelation in Colloidal Aggregation. *Physical Review Letters Phys. Rev. Lett. PRL* **93**, 108302 (2004).
16. Mohraz, A. & Solomon, M. J. Gelation and internal dynamics of colloidal rod aggregates. *Journal of Colloid and Interface Science* **300**, 155-162 (2006).

17. Dibble, C. J., Kogan, M. & Solomon, M. J. Structure and dynamics of colloidal depletion gels: Coincidence of transitions and heterogeneity. *Physical Review E Phys. Rev. E PRE* **74**, 041403 (2006).

18. Colvin, V. L. From opals to optics: Colloidal photonic crystals. *Mrs Bulletin* **26**, 637-641 (2001).

19. Arsenault, A. C., Puzzo, D. P., Manners, I. & Ozin, G. A. Photonic-crystal full-colour displays. *Nat Photon* **1**, 468-472 (2007).

20. Marlow, F., Muldarisnur, Sharifi, P., Brinkmann, R. & Mendive, C. Opals: Status and Prospects. *Angewandte Chemie International Edition Angewandte Chemie International Edition* **48**, 6212-6233 (2009).

21. Beltran-Villegas, D. J. & Bevan, M. A. Free energy landscapes for colloidal crystal assembly. *Soft Matter Soft Matter* **7**, 3280-3285 (2011).

22. Beltran-Villegas, D. J., Schultz, B. A., Nguyen, N. H. P., Glotzer, S. C. & Larson, R. G. Phase behavior of Janus colloids determined by sedimentation equilibrium. *Soft Matter Soft Matter* **10**, 4593-4602 (2014).

23. Glotzer, S. C. & Solomon, M. J. Anisotropy of building blocks and their assembly into complex structures. *Nat Mater* **6**, 557-562 (2007).

24. Shah, A. A., Schultz, B., Zhang, W., Glotzer, S. C. & Solomon, M. J. Actuation of shape-memory colloidal fibres of Janus ellipsoids. *Nat Mater* **14**, 117-124 (2015).

25. Damasceno, P. F., Engel, M. & Glotzer, S. C. Crystalline Assemblies and Densest Packings of a Family of Truncated Tetrahedra and the Role of Directional Entropic Forces. *ACS Nano ACS Nano* **6**, 609-614 (2012).

26. Damasceno, P. F., Engel, M. & Glotzer, S. C. Predictive Self-Assembly of Polyhedra into Complex Structures. *Science* **337**, 453-457 (2012).

27. Auzerais, F. M., Jackson, R. & Russel, W. B. The resolution of shocks and the effects of compressible sediments in transient settling. *Journal of Fluid Mechanics* **195**, 437-462 (1988).

28. Batchelor, G., K. Sedimentation in a dilute dispersion of spheres. *Journal of Fluid Mechanics* **52**, 245-268 (1972).

29. Davis, K. E. & Russel, W. B. An asymptotic description of transient settling and ultrafiltration of colloidal dispersions. *Physics of Fluids A: Fluid Dynamics (1989-1993)* **1**, 82-100 (1989).

30. Davis, K. E., Russel, W. B. & Glantschnig, W. J. Settling suspensions of colloidal silica: observations and X-ray measurements. *J. Chem. Soc., Faraday Trans.* **87**, 411-424 (1991).

31. Piazza, R., Bellini, T. & Degiorgio, V. V. Equilibrium sedimentation profiles of screened charged colloids: A test of the hard-sphere equation of state. *Phys Rev Lett* **71**, 4267-4270 (1993).

32. Piazza, R. Settled and unsettled issues in particle settling. *Reports on Progress in Physics* **77**, 056602 (2014).

33. Ackerson, B. J. & Pusey, P. N. Shear-induced order in suspensions of hard spheres. *Phys Rev Lett* **61**, 1033-1036 (1988).

34. Shereda, L. T., Larson, R. G. & Solomon, M. J. Local stress control of spatiotemporal ordering of colloidal crystals in complex flows. *Physical review letters* **101**, 038301 (2008).

35. Trau, M., Saville, D. A. & Aksay, I. A. Field-Induced Layering of Colloidal Crystals. *Science Science* **272**, 706 (1996).

36. Ferrar, J. A. & Solomon, M. J. Kinetics of colloidal deposition, assembly, and crystallization in steady electric fields. *Soft Matter Soft Matter* (2015).

37. Gangwal, S., Pawar, A., Kretzschmar, I. & Velev, O. D. Programmed assembly of metallodielectric patchy particles in external AC electric fields. *Soft Matter* **6**, 1413-1418 (2010).

38. Gong, T., Wu, D. T. & Marr, D. W. M. Electric Field-Reversible Three-Dimensional Colloidal Crystals. *Langmuir Langmuir* **19**, 5967-5970 (2003).

39. Shah, A. A. et al. Liquid crystal order in colloidal suspensions of spheroidal particles by direct current electric field assembly. *Small* **8**, 1551-1562 (2012).

40. Bard, A. J. & Faulkner, L. R. Electrochemical methods: fundamentals and applications, 2nd. *Hoboken: Wiley and Sons* (2001).

41. O'Brien, R. W. & White, L. R. Electrophoretic mobility of a spherical colloidal particle. *Journal of the Chemical Society, Faraday Transactions 2: Molecular and Chemical Physics* **74**, 1607-1626 (1978).

42. Rogach, A. L., Kotov, N. A., Koktysh, D. S., Ostrander, J. W. & Ragoisha, G. A. Electrophoretic deposition of latex-based 3D colloidal photonic crystals: A technique for rapid production of high-quality opals. *Chemistry of materials* **12**, 2721-2726 (2000).

43. Kim, Y., Shah, A. A. & Solomon, M. J. Spatially and temporally reconfigurable assembly of colloidal crystals. *Nat Commun* **5**, 3676 (2014).

44. Shah, A. A., Ganesan, M., Jocz, J. & Solomon, M. J. Direct current electric field assembly of colloidal crystals displaying reversible structural color. *ACS Nano* **8**, 8095-8103 (2014).

45. Jacobson, J. M. & Comiskey, B. Nonemissive displays and piezoelectric power supplies therefor. (1999).

46. Kwon, H.-K. et al. Optically Switchable Smart Windows with Integrated Photovoltaic Devices. *Advanced Energy Materials Adv. Energy Mater.* **5**, 1401347-n/a (2015).

47. Atwood, J. L. Kagome lattice: A molecular toolkit for magnetism. *Nat Mater* **1**, 91-92 (2002).

48. Chen, Q., Bae, S. C. & Granick, S. Directed self-assembly of a colloidal kagome lattice. *Nature* **469**, 381-384 (2011).

49. Paulose, J., Meeussen, A. S. & Vitelli, V. Selective buckling via states of self-stress in topological metamaterials. *Proceedings of the National Academy of Sciences* **112**, 7639-7644 (2015).

50. Sun, K., Souslov, A., Mao, X. & Lubensky, T. C. Surface phonons, elastic response, and conformal invariance in twisted kagome lattices. *Proceedings of the National Academy of Sciences* **109**, 12369-12374 (2012).

51. Madivala, B., Fransaer, J. & Vermant, J. Self-Assembly and Rheology of Ellipsoidal Particles at Interfaces. *Langmuir Langmuir* **25**, 2718-2728 (2009).

52. Bowden, N., Terfort, A., Carbeck, J. & Whitesides, G. M. Self-Assembly of Mesoscale Objects into Ordered Two-Dimensional Arrays. *Science* **276**, 233-235 (1997).

53. Bowden, N., Arias, F., Deng, T. & Whitesides, G. M. Self-Assembly of Microscale Objects at a Liquid/Liquid Interface through Lateral Capillary Forces. *Langmuir Langmuir* **17**, 1757-1765 (2001).

54. Binks, B. P. Particles as surfactants‚Äîsimilarities and differences. *Current Opinion in Colloid & Interface Science* **7**, 21-41 (2002).

55. Razavi, S. et al. Collapse of Particle-Laden Interfaces under Compression: Buckling vs Particle Expulsion. *Langmuir Langmuir* **31**, 7764-7775 (2015).

56. Lewandowski, E. P. et al. Orientation and Self-Assembly of Cylindrical Particles by Anisotropic Capillary Interactions. *Langmuir Langmuir* **26**, 15142-15154 (2010).

57. Aveyard, R. et al. Measurement of Long-Range Repulsive Forces between Charged Particles at an Oil-Water Interface. *Physical Review Letters Phys. Rev. Lett. PRL* **88**, 246102 (2002).

58. Cavallaro, M., Botto, L., Lewandowski, E. P., Wang, M. & Stebe, K. J. Curvature-driven capillary migration and assembly of rod-like particles. *Proceedings of the National Academy of Sciences* **108**, 20923-20928 (2011).

59. Lewandowski, E. P., Bernate, J. A., Tseng, A., Searson, P. C. & Stebe, K. J. Oriented assembly of anisotropic particles by capillary interactions. *Soft Matter Soft Matter* **5**, 886-890 (2009).

60. Loudet, J. C., Alsayed, A. M., Zhang, J. & Yodh, A. G. Capillary Interactions Between Anisotropic Colloidal Particles. *Physical Review Letters Phys. Rev. Lett. PRL* **94**, 018301 (2005).

61. Madivala, B., Vandebril, S., Fransaer, J. & Vermant, J. Exploiting particle shape in solid stabilized emulsions. *Soft Matter Soft Matter* **5**, 1717-1727 (2009).

62. Solomon, T. & Solomon, M. J. Stacking fault structure in shear-induced colloidal crystallization. *J Chem Phys* **124**, 134905 (2006).

63. Kang, S.-M. et al. Capillarity-induced directed self-assembly of patchy hexagram particles at the air-water interface. *Soft Matter Soft Matter* **12**, 5847-5853 (2016).

64. Pfleiderer, P. & Schilling, T. Simple monoclinic crystal phase in suspensions of hard ellipsoids. *Physical Review E Phys. Rev. E PRE* **75**, 020402 (2007).

65. Ho, C. C., Keller, A., Odell, J. A. & Ottewill, R. H. Preparation of monodisperse ellipsoidal polystyrene particles. *Colloid Polym Sci* **271**, 469-479 (1993).

66. Keville, K. M., Caruthers, J. M. & Franses, E. I. Characterization of dimensions of ellipsoidal microparticles via electron microscopy. *Journal of Microscopy* **142**, 327-340 (1986).

67. Mohraz, A. & Solomon, M. J. Direct Visualization of Colloidal Rod Assembly by Confocal Microscopy. *Langmuir Langmuir* **21**, 5298-5306 (2005).

68. Mukhija, D. & Solomon, M. J. Translational and rotational dynamics of colloidal rods by direct visualization with confocal microscopy. *Journal of colloid and interface science* **314**, 98-106 (2007).

Chapter 2

Kinetics of colloidal deposition, assembly, and crystallization in steady electric fields

2.1 Abstract

We quantify and model the deposition and crystallization kinetics of initially dilute colloidal spheres due to application of a steady, direct current electric field in the thin gap between parallel electrodes. The system studied is poly(12-hydroxystearic acid) (PHSA)-stabilized poly(methyl methacrylate) (PMMA) spheres dispersed in a mixture of cyclohexylbromide (CHB), decalin, and a low concentration of the partially disassociating salt tetrabutylammonium chloride (TBAC). The temporal and spatial evolution of the colloidal volume fraction in the ~ 1 mm gap between the electrodes is quantified under conditions of both deposition and relaxation by confocal laser scanning microscopy (CLSM). During deposition assembly, the spatial dependence of the colloid volume fraction approaches steady state at times between hundreds of minutes at the lowest electric field strength (as characterized by a Peclet number, Pe) and at tens of minutes at higher field strengths. During disassembly, the volume fraction relaxes nearly exponentially. The kinetics are modeled by adapting a treatment for sedimentation (Davis and Russel, *Phys. Fluids A*, **1**, 82, 1989) to the case of steady electric

fields. The model's predictions show good agreement with the measured kinetics at low Pe; however, agreement progressively deteriorates with increasing Pe. At low Pe the deposits are initially disordered. After an initial delay, 1D crystal growth propagates from the electrode surface at rates of several hundred nm/min. The sharp crystal boundary propagates as a characteristic of constant colloidal volume fraction, consistent with an equilibrium crystalline phase transition. The results inform operational ranges for devices that produce active colloidal matter by reversible assembly.

2.2 Introduction

Colloidal crystal arrays with long-range positional order possess useful functional properties such as a photonic band gap, [1] iridescence, [1] and controllable porosity. [1,2] Steady external fields – electric, [3,4] gravitational, [5-8] and shear [9,10] – assist self-assembly by either concentrating particles to the point of a disorder-to-order phase transition or by accelerating the kinetics of this transition. Steady, direct current (DC) electric fields are of particular interest in this assembly process due to the fact that they are non-invasive, require only low power, and yield 3D assemblies. [3] This method has recently been applied to generate reversible structural color in latex colloidal suspensions. [11-15]

When a steady, uniform electric field, as generated by a Faradaic current, is applied to a dilute suspension of charged particles, the particles migrate toward an oppositely charged electrode via electrophoresis. [3,16] The concentrated colloids form either ordered assemblies or amorphous deposits depending on the initial volume fraction of the suspension, [6] the Peclet number, [3,6] the suspension's compressibility and hydrodynamic interactions, and the time. [3,9,10]

Here the Peclet number is defined as $Pe = (2U_0R)/D_0$, where U_0 is the free particle electrophoretic velocity, R is the sphere radius, and D_0 is the Brownian diffusivity. Here $U_0 = f_0\varepsilon\varepsilon_0\zeta E/\eta$, where ε is the dielectric constant of the solvent, ε_0 is the vacuum permittivity, ζ is the particle zeta potential, E is the strength of the electric field, and f_0 is a constant that ranges between 0.67 (Debye layer, κ^{-1}, >> 2R) and 1 (κ^{-1} << 2R). [17] E is equal to the field's current density (i) divided by the electrical conductivity (λ_0) of the solvent; η is the viscosity of the solvent. Pe is the ratio of the electrophoretic velocity of a free particle, scaled by its characteristic length, to Brownian diffusivity.

Under the action of the uniform electric field, particles migrate toward the electrode and self-organize into deposits with a colloid volume fraction, ϕ, that varies with distance from the electrode. The spatially varying volume fraction generates a gradient in osmotic pressure. In the presence of the steady electric field, forces originating from both the applied field and the induced gradient in osmotic pressure therefore act upon the particles; it is their time-dependent balance that determines the kinetics of assembly. If the steady-state electric field is removed, the now unbalanced gradient in compressibility drives a flux of particles away from the electrode and back into the bulk region. The specific aim of this paper is to quantify and model the spatiotemporal behavior of the colloidal volume fraction during these two processes. Because of its relevance to applications, we pay special attention to the kinetic requirements for colloidal crystallization during the assembly process.

The rationale for the initial volume fraction, field strengths, Peclet numbers, and device gap that we select for study is that colloidal crystallization is induced rapidly (t ~ tens to hundreds of minutes) in thin regions ($h_{crystal}$ ~ tens of microns) in geometries of small thickness (h ~ 1 mm). These parameters define a range that is useful for applications. [1,2] In addition, the

thin geometries typical of direct current electric field assembly are an advantage for reversible assembly, [3,13,15,18,19] because the smaller scales leaded to accelerated assembly kinetics, which might potentially be exploited in applications such as switchable structural color, [11-15] photonic materials, [1] or in sensing. [20] To produce these crystals at such conditions, it has been found that Pe ~ 0.1 – 1.0 are needed. [3,6] These physical parameters and deposition conditions contrast significantly with another common experiment – gravitational sedimentation – for which field-effects on colloidal crystallization have been studied. In sedimentation, colloidal crystallization is induced in thick regions ($h_{crystal}$ ~ 1 cm) from much larger initial heights ($h_{initial}$ ~ 10^1 cm and greater) and at much longer times (t ~ several months). [7,21,22]

The steady-state density profile deduced from either sedimentation (of thick samples) or direct current electric fields (of thin samples) has been used to characterize the equation of state of different colloidal systems, including spheres at different electrolyte concentrations and rods of different aspect ratio. [3,8,23] In these cases, measurements were performed at low Peclet numbers, experimental durations were long, and assembly kinetics were neither studied nor modeled. In addition, deposition kinetics has been studied in thick geometries over a range of Peclet numbers so as to understand conditions at which colloidal crystallization occurs. [22]

There is thus an unstudied parameter space of thin sample thicknesses, short deposition times, and small-applied field strengths that is of both scientific and technological interest. In this space, there is a potential operating window in which deposition would occur rapidly but colloidal crystallization would still be induced. The aim of this paper is to study this operating regime, and learn if the deposition and crystallization kinetics in it can be modeled by transport theory. Scientific questions in this regime are: (i) whether or not the continuum approximation implicit in colloidal transport theory can be applied in a regime in which the deposits are ~ 50

μm in final height; (ii) whether or not applied field strengths are large enough to generate sufficient osmotic pressure to induce crystallization, yet small enough to avoid non-equilibrium effects such as jamming and vitrification; (iii) if available methods to parameterize the thermodynamic and hydrodynamic functions necessary to apply the transport theory are sufficient to model the complex kinetics that is observed for the times and field strengths of interest.

In this paper, the process in which particles move toward the electrode under the action of the applied field is called deposition. The process in which the colloids disassemble when the field is removed is called relaxation. We characterize the electric-field induced colloidal deposition and relaxation by measuring the spatial and temporal evolution of the volume fraction (ϕ) and the crystal thickness of the colloids from CLSM image analysis. [24] The model system studied is an initially dilute suspension of poly(methyl methacrylate) spheres dispersed in a density and refractive index-matched solvent of cyclohexylbromide (CHB) and decalin. This system is commonly applied for direct visualization studies by confocal microscopy and is a model system for study of the phase behavior and dynamics of colloids. [9,25,26] We predict the evolution of ϕ and crystallinity by adapting a one-dimensional model for sedimentation [21,22] in a gravitational field in thick geometries (tens of cms) to the related case of an applied DC electric field in a thin geometry (1.15 mm). The comparison supports the applicability of the model, and indicates that optimal colloidal crystals are accessible by this simple technique if deposition is conducted at Pe ~ 0.2 for durations on the order of an hour. Relaxation experiments and modeling show that this colloidal crystallization is rapidly reversible – with the accumulated deposits returning to an amorphous state within tens of minutes after the applied field is released.

The results suggest that cycling between crystalline and amorphous states can be accomplished on scales of ~ 120 min or longer by this method.

2.3 Materials & Methods

2.3.1 Colloidal suspensions

Poly(12-hydroxystearic acid) (PHSA)-stabilized poly(methyl methacrylate) (PMMA) spheres of diameter 736 nm (+ 7.7% polydispersity) were synthesized following the methods of Antl et al. [27] The particles contain Nile Red fluorescent dye and are imaged with a Nikon A1Rsi Confocal Laser Scanning Microscope (CLSM) (100x NA = 1.4 oil immersion objective). To ensure the presence of sufficient particle charge for deposition in the solvents of interest, a restabilization procedure was undertaken in which the particles were re-equilibrated with a concentration of PHSA ranging from equivalent to the concentration of particles to slightly greater than the concentration of particles over a period ranging from 2 to 3 days. [28] The restabilized particles maintained their charge for several weeks. As needed, the procedure was repeated to reestablish the charge. After restabilization, the particles were dispersed in a density- and refractive index-matched mixture of 66 vol. % cyclohexylbromide (CHB) and 34 vol. % decalin at a volume fraction of 0.02.

Solution conductivity, through tetrabutylammonium chloride (TBAC) electrolyte concentration, and applied current density were adjusted to produce four solutions whose direct current electric field assembly could be conducted at constant Pe of 0.14, 0.22, 0.80, and 1.07. These conditions bracket the operating range that yields both rapid deposition and high quality crystallization. The measured applied current density, particle zeta-potential, solvent electrical

conductivity, TBAC concentration, and Debye length (κ^{-1}) for each of the systems are reported in Table 1.

Other values reported in Table 1, and which are needed for the modeling are: (i) the free particle electrophoretic mobility (U_0/E); (ii) K_2, the estimated $O(\phi)$ correction to the particle velocity, $U(\phi) = U_0(1 + K_2(\phi))$ for the deposition and for the relaxation portions of the experiments. [29-31] K_2 accounts for the effects of hydrodynamic interactions on field-induced particle convection, including the effects of backflow. We experimentally measure U_0 for all deposition conditions from data collected at short times when the particle concentration is low; details of these measurements are included in the SI. The electric field strength (E) is characterized by the current density (i) and the solution conductivity, λ_0, by $E = i/\lambda_0$. The current density is the applied current per electrode cross-sectional area. The large ζ and κ^{-1} suggest that suspensions of the particles at high volume fraction might strongly interact thorough screened Coulombic interactions.

In electrophoresis, theory and experiment suggest that the effect of particle concentration on mobility is weaker than in sedimentation. Specifically, experiments suggest that $K_2 = -1$ rather than $K_2 = -6.55$ as for hard spheres in sedimentation, as indicated in Table 1. When the electric field is turned off, during relaxation, electrophoresis is no longer active. The particle mobility in this case is given by $K_2 = -6.55$. Electrostatic interactions between the charged colloids do affect the concentration-dependent mobility; the estimated magnitude of this effect is explored in Fig. 2-11. [32,33]

2.3.2 DC electric field device for colloidal deposition

Fig. 1a is a schematic of the device used for DC electric field assembly of the colloids. The device consists of two plane parallel, glass electrodes, coated with indium tin oxide (ITO) as per Shah et al. [3] and separated by a 1.15 mm thick glass spacer. The ITO coated surfaces are in contact with the suspension. A 5 mm circular hole is drilled into the center of the spacer to create a colloidal suspension chamber. This chamber holds approximately 23 μL of colloidal suspension and is sealed on either side by the electrodes with UV-curable glue. 19.6 mm^2 of each electrode are exposed to the colloidal suspension.

The device is placed onto the stage of the CLSM (Nikon A1 Piezo z-drive) for direct visualization of deposition and disassembly. Both electrodes are connected to an Autolab PGSTAT 128N potentiostat/galvanostat. For deposition, we use galvanostatic (constant current, variable voltage) operation because it yields experiments at constant Pe. Then, the applied voltage progressively increases with time to compensate for the depletion of different electrochemically active species within the solvent. [34] Upon completion of the deposition process, the current is turned off, and a constant electric potential of 0 Volts (V) is applied. This condition approximates the application of no power to the system, as the cell's (measured) open circuit voltage is very small (0.03V). The voltage-current behavior observed for a particular experiment is shown in Fig. 1b and 1c.

Electrophoretic deposition and subsequent relaxation were imaged in a 2D plane oriented perpendicular to the device's electrodes. (Time-resolved 3D imaging was not possible because the large electrophoretic velocity of the particles caused sufficient displacement that particles locations could not be accurately determined by 3D image analysis.) To capture changes in colloidal volume fraction and crystallization with axial distance above the electrode, a time-series of images is acquired in a plane perpendicular to the electrode surface. The excitation was

at 561 nm and the emission was collected from 570-620 nm. The image, of resolution 512 x 1593, is acquired as a set of line scans of length 15.93 mm, each separated by a vertical distance of 0.031 mm. The pixel size is 0.031 x 0.031 mm^2, the image size is 15.93 x 49.50 um^2, and the frame rate is one every three seconds.

2.3.3 Image analysis, colloid volume fraction, and crystallization height

Fig. 2a is a typical image acquired during the electric field assembly. In this image the electrode surface is visible as a line at the bottom below which there are no colloids. In Fig. 2a, as is characteristic with all experiments performed, the colloidal volume fraction, ϕ, varies with distance above the electrode. There is little variability in ϕ along lines parallel to the electrode. The spatial dependence of the volume fraction, $\phi(z,t)$, is determined from the image time series, of which Fig. 2a represents one instance. Image analysis is by the algorithm of Crocker and Grier. [24] Briefly, after a filtering step to smooth high frequency noise, pixels of the highest intensity in a spatial region of a dimension of approximately the particle diameter are identified as particle centroids. Thus, the image analysis yields the location of every particle identified within the image.

Fig. 2b shows the particle centroids identified by the image analysis of Fig. 2a (the black dots represent identified particle centroids and are overlayed on top of a grayscale rendering of the original CLSM image). These centroids are located to precision of ± 20 nm and ± 77 nm in the tangential and axial directions, respectively, as found from image analysis of a specimen immobilized by photopolymerization. A check of the overlay image indicates the volume fraction found by image analysis is within 6% of the volume fraction expected based on the

volume of the particles relative to the size of the imaged volume. Although we image ~40 μm above the electrode, we limit our analysis to a region 20 μm above the electrode, due to imaging effects that may cause inaccuracies in particle identification at distances far from the coverslip.

The identified particles centroids are resolved into bins centered on different heights above the electrode. We take the distance of 4 layers of close-packed FCC particle layers (bin height = 4*0.767D = 2.26 μm) as the bin width and there are 10 of these vertical bins per image. The result is shown in Fig. 2c, which is the measure N(z)/A, or the number of particles per unit image area centered on each vertical height z. We transform N(z)/A to f(z) by means of a calibration generated by CLSM measurements on 12 specimens of known volume fraction, as shown in Fig. 2d. To implement the calibration, we fit the Fig. 2d calibration curve to a high order polynomial. This method avoids the need to estimate the uncertain optical depth of field of the acquired 2D images.

Fig. 2e shows the final result of $\phi(z)$ for the colloidal suspension imaged in Fig. 2a. To observe the evolution of $\phi(z)$ in time, we repeat the image analysis and conversion from N(z)/A to $\phi(z)$ for each of the images in the time series used to capture the kinetics. To address noise in the time series, we take $\phi(z,t_i)$ as the average of images in the time from $\phi(z, 0.9t_i)$ to $\phi(z, 1.1t_i)$. (For example, $\phi(z, t = 300$ seconds) is an average of $\phi(z, 270 \leq t \leq 330$ seconds).) We also report the standard deviation of frames as error bars on $\phi(z,t)$ plots. To capture any error associated with specimen-to-specimen variability, we also performed five replicate trials at the condition Pe = 1.07. The error bars reported on $\phi(z,t)$ plots at this condition therefore establish the contribution of replication error.

2.3.4 Kinetic modeling of deposition and relaxation

To model field-induced deposition and subsequent relaxation in a steady electric field, we adopt a one-dimensional colloidal transport model from the sedimentation literature. [7] Specifically, the convective-diffusion equation for the volume fraction field is:

$$\frac{\partial \phi}{\partial t} + U_0 \frac{\partial}{\partial z}\left(\phi K(\phi)\right) = D_0 \frac{\partial}{\partial z}\left(K(\phi)\frac{d}{dz}[\phi Z(\phi)]\frac{\partial \phi}{\partial z}\right) \qquad (1)$$

Here U_0 is the electric field-induced free particle electrophoretic velocity. The compressibility, $Z(\phi)$, is directly measured by the method discussed in the next section. $K(\phi)$ accounts for concentration effects on the colloidal mobility, $U(\phi)/U_0 = K(\phi)$. D_0 is the Stokes-Einstein diffusivity, and $Z(\phi)$ is the compressibility factor of the suspension. In colloidal suspensions, $Z(\phi) = \Pi(\phi)/nkT$, which is a ratio of the suspension's ϕ-dependent osmotic pressure to the osmotic pressure of an ideal solution. Here, $n = \phi/V_{particle}$, or the number of particles per volume of suspension. Eqn. (1) quantifies the effect the electric field (convective term) and gradients in osmotic pressure (diffusion term) have on $\phi(z,t)$. To model the retardation of particle mobility with concentration, we use the empirical function $K(\phi) = (1-\phi)^{-K_2}$, with K_2 as assigned in Table 1. Note that K_2 varies between deposition (field on) and relaxation (field off) experiments because of the effect of the steady electric field on the concentration dependent mobility. [29-31] The concentration-dependent mobility for the relaxation experiments is taken as that of amorphous hard spheres. Crystallinity and charge is known to affect the concentration-dependent mobility, and these effects have been studied by both experiment and theory. [32,33,35] Fig. S5 explores how these effects change model predictions. Their effects are small for the systems and conditions studied here. Note that during relaxation, no electric field is applied and therefore $U_0 = 0$; eqn (1) thus reduces to the diffusion equation.

Eqn (1) is solved numerically by the finite element method (FEM), implemented in *COMSOL Multiphysics*, for 1D transport with ϕ-dependent rates of convection and diffusion. The spatial domain is the gap between the device's electrodes (1.15 mm). There are two time domains: the time of particle deposition, t_{dep}, and the time of particle relaxation, t_{rel}, which begins as soon as t_{dep} ends. The initial condition is the initial volume fraction profile ($\phi(z, t = 0)$) of the suspension, and the boundary conditions are no particle flux at either electrode. For deposition, $\phi(z, t_{dep} = 0) = 0.02$ at all positions within the sample. For relaxation, the initial condition $\phi(z, t_{rel} = 0)$ is as predicted by the model at the end of deposition – just before the field is turned off and the relaxation begins.

The spatial domain is divided into either 1,000 or 10,000 elements, the time domains use steps of either 0.1 or 1 s, and the relative tolerance is varied between 0.01 and 0.05, depending on which of the above numerical parameter values allow for convergence of the numerical method. A coarser mesh in both time and space, as well as a greater relative tolerance, is needed for convergence as Pe increases. We assessed the effects of grid element number, time step, and tolerance on simulation results by changing grid element number and time step size by set factors (i.e. a factor of 10 at Pe = 0.14) and tolerance step sizes by a set factor (i.e. a factor of 5 at Pe = 0.14) and saw negligible differences in solutions to eqn (1).

2.3.5 Compressibility Factor of Charged Colloidal Suspensions

Modeling the kinetics of deposition and relaxation from eqn (1) requires $Z(\phi)$ for the charged suspensions studied. Recall that $Z(\phi) = \Pi(\phi)/nkT$. $\Pi(\phi)$ can be directly inferred from the equilibrium sedimentation profile as per the method of Piazza. [8] For sedimentation, particles

with a buoyant mass settle to a steady-state profile determined by hydrostatic equilibrium. For direct current electric field assembly, the equivalent expression is:

$$\Pi(n) = F_E \int_z^h n(z)dz \qquad (2)$$

Where n(z) is the particle number density as a function of axial position within the sample, and the limits of integration extend from an axial point z in the assembly to the top of the sample (z = h). Here F_E is the force of the electric field on the particle at steady-state. To measure Π(n) for the charged colloidal system studied, we subjected a suspension to a constant-current electric field until a steady state in ϕ(z,t) was achieved. Fig. 3a is the steady-state structure of the specimen. By numerically integrating this density profile per eqn (2) we obtain Π(z), and thus Π(n). As n(z) is simply ϕ(z) scaled on the volume of a particle, this method yields Z(ϕ), as plotted in Fig. 3b.

In eqn (2), the force of the electric field on the particle, F_E, depends on the Debye layer thickness relative to the particle size. In the Debye-Huckel limit for κD << 1, F_E is balanced by Stokes drag and is equal to $4\pi\varepsilon\varepsilon_0\zeta RE$ where ε is the solvent dielectric constant, ε_0 is the permittivity of free space, and E is the magnitude of the electric field.[36] Here, F_E in eqn (2) is directly characterized from the limiting behavior of the compressibility at vanishing volume fraction: Z(ϕ = 0) = 1. From this limiting behavior we characterize F_E to be a factor of 1.86 less than the Debye-Huckel limit. That is, we implicitly use the ideal solution limit of the compressibility, as measured at equilibrium, to characterize the force of the electric field on a particle in the system.

To model the experimental Z(ϕ), we adopt the following continuous, differentiable function given by Peppin et al. [37]

$$Z(\phi) = \frac{1+a_1\phi+a_2\phi^2+a_3\phi^3+a_4\phi^4}{1-\phi/\phi_p} \quad (3)$$

where a_1=4-1/ϕ_p, a_2 = 10-4/ϕ_p, a_3 = 18-10/ϕ_p, and a_4 = α/ϕ_p^5 -18/ϕ_p. Here α and ϕ_p are model parameters. Peppin's original model, developed for hard spheres, diverges at 0.64. To account for the different divergence volume fraction of the charged spheres used in this study, the model parameters are taken as α = 0.3 and ϕ_p = 0.55, respectively. The fit of eqn (3) to the measured Z(ϕ) data points is plotted in Fig. 3.

2.4 Results

2.4.1 Colloidal deposition and relaxation under a steady electric field

Fig. 4 reports images of colloidal deposition at a constant current density of 0.51 nA/mm^2 (Pe = 0.22; Fig. 4a - 4e), as well as the subsequent relaxation of the assembled structure (Fig. 4f - 4j). A movie of the image time series is in the Supporting Information (Movie S1). Prior to application of the electric field (Fig. 4a), particles are homogeneously dispersed at an initial volume fraction of 0.02. Fig. 4b shows the sample after 30 minutes of electrophoretic deposition. A dense, amorphous deposit is observed at the electrode; the particle density decays with increasing distance from it. Fig. 4c shows the sample after 1 hour of deposition; colloidal crystallization is observed at this time. A sharp disorder-to-order transition is observed; the boundary spans the width of the entire image at a z-position of ~ 7 microns above the electrode. Above this boundary, ϕ(z) varies rapidly with distance above the electrode. After two hours of deposition (Fig. 4d), the crystallization phase boundary has now propagated nearly to the top of the image and the particle density appears constant with distance above the bottom electrode.

Fig. 4e shows the sample after 3 hours of particle deposition; an ordered crystal fills the entire imaged region. The density of this crystal appears slightly greater than the crystal observed at t = 2 hr.

The steady electric field is removed in the moments between Fig. 4e and 4f, and thus Fig. 4f shows the suspension at the onset of relaxation. In the absence of the applied electric field (Fig. 4g – 4j), particles diffuse away from the electrode toward the bulk solution. Fig. 4g shows the suspension after 5 minutes of relaxation. The deposit appears more disordered relative to the one observed in Fig. 4f; however, some order is still apparent throughout the sample. Fig. 4h shows the suspension after 15 minutes of relaxation. The particle number density is less than in the earlier frames, and crystalline order has vanished. Fig. 4i and j shows the sample after 30 and 90 minutes of relaxation – disorder and dilution due to diffusion of the particles away from the near-electrode region continues. During relaxation (field off), the particle density remains more uniform with distance above the electrode than during deposition, as evidenced by comparison of early time images of deposition (e.g. Fig. 4b) and late time images of relaxation (e.g. Fig. 4i).

Images of deposition and relaxation at the other Pe conditions studied are shown in Figs. 5-7. In each case, the deposition was continued until $\phi(z,t)$ attained steady state within the image area, which was approximately 40 μm above the electrode. This criterion yielded 420 minutes of deposition at Pe = 0.14, 180 minutes of deposition at Pe = 0.22, 90 minutes at Pe = 0.80, and 30 minutes at Pe = 1.07. Thus, particles deposit faster at higher Pe numbers.

The following qualitative effects are noted by comparing Fig. 4 and Figs. 5-7. First, appreciable colloidal crystallization is observed at Pe = 0.14 (Fig. 5) and Pe = 0.22 (Fig. 4 and SI

movie 1). In both cases, crystallization is first observed at the electrode boundary. A front with crystal below and amorphous liquid above is established. The front propagates upward from the electrode surface. At Pe = 0.14, we observe high quality order of the crystal on a local scale; however, long-range order is imperfect – grain boundaries and stacking faults are observed. Comparable ordering is observed at Pe = 0.22. By comparison, little to no ordering was observed at Pe = 0.80 (Fig. 6) and Pe = 1.07 (Fig. 7).

2.4.2 Electrostatic and electric field characterization of the particle-solvent systems

Colloidal sedimentation theory was adapted to deposition in steady electric fields to infer the electrophoretic velocity of dilute colloids (U_0) at each Pe condition studied, as well as for the characterization of the electric field force for the characterization of the equation of state of the charged colloids. As described by Russel et al. [36] and as applied by Kim et al., [25] mass conservation connects the time rate of change in colloidal volume during sedimentation to a flux in particle density. Under dilute conditions, the relationship is:

$$\frac{h_{electrode}}{t_{electrode}} = U_0 \frac{\phi_0 K(\phi_0)}{\phi_{electrode} - \phi_0} \qquad (4)$$

Here, $t_{electrode}$ is the time required to achieve a given volume fraction ($\phi_{electrode}$) of height $h_{electrode}$, and ϕ_0 is the initial volume fraction of the colloids. Here we take $h_{electrode}$ to be four colloidal layers, consistent with the resolution used elsewhere in the paper. $K(\phi)$ is given in the main text of the paper. From eqn. (4), plotting $t_{electrode}$ versus $\frac{h_{electrode}}{K(\phi_0)}\left(\frac{\phi_{electrode}}{\phi_0} - 1\right)$ yields a proportional relationship, the inverse of which is the free particle electrophoretic velocity (U_0). This characterization was carried out at early times ($t_{electrode} \leq 0.15 t_{SS}$) at each condition. Initial

volume fractions were 0.02 at all Pe conditions and 0.01 for the equation of state characterization. Linear regression of the data to eqn. (4) is shown in Fig. 8. U_0 values are reported in Table 1.

2.4.3 Colloidal deposition and relaxation kinetics

Fig. 9 shows $\phi(z = 0, t)$, hereafter referred to as $\phi_{electrode}(t)$, for all Pe conditions. $\phi_{electrode}(t)$, is the largest particle density in the deposit at that time, and therefore is a characteristic measure of the deposition and relaxation dynamics. Data points represent experimental measurements, while curves represent solutions to eqn (1). The error bars represent the standard deviation of these time-averaged measurements. Recall that the Pe = 1.07 condition was replicated five times in order to quantify the error associated with sample-to-sample variability; in this case the data points are an average of these five separate, time-averaged measurements.

The colloids deposit very rapidly at the onset of the steady electric field, and a corresponding increase in $\phi_{electrode}$ at early deposition times is observed in all cases. Consistent with the images of Figs. 4-7, we observe a plateau of measured $\phi_{electrode}$ profiles at later deposition times, indicating that a steady state in $\phi(z,t)$ is approached. The solid curves are the solution to eqn (1) at each Pe using the average measured value of U_0 for each condition from Table 1. The dotted curves are the solutions to eqn (1) for the upper and lower limits of the standard deviation in U_0, also as reported in Table 1. Recall that U_0 is the velocity of a dilute colloid at the applied field strength (Pe). It was characterized by direct measurement at early-time conditions, as described in section 2.4.2.

Especially when the uncertainty in U_0 is considered, the measured deposition kinetics are modeled to a fair degree by eqn (1). Specifically, the rapid deposition at high Pe is captured, and the steady-state volume fraction is well modeled except at the highest Pe studied. At low Peclet number, the experiments show a somewhat faster deposition than the model predicts, even allowing for the uncertainty in U_0. In addition, at the highest Peclet number, the steady-state volume fraction predicted by the transport model is greater than the measured steady-state volume fraction by a factor of 1.2. The effect of the error in U_0 is more significant at Pe = 0.14 and Pe = 0.22 than at Pe = 0.80 and Pe = 1.07 even though, as can be seen in Table 1, the standard deviation of U_0 measurements was similar across all Pe conditions. This sensitivity arises from the steepness of $Z(\phi)$ at high ϕ. As Pe increases, $Z(\phi)$ increases. In this region, a unit change (error) in $Z(\phi)$ has just a small effect on ϕ. Consequently, at low Pe modeling errors in ϕ are ~ 5%. These errors reduce to ~ 1% at the higher Pe number conditions. Thus, the effect of the uncertainty in U_0 measurements has a greater effect on eqn (1)'s performance at lower Pe numbers than at higher Pe number.

There is a significant disagreement between the steady-state results for experiment and model at Pe = 1.07. A systematic difference between the equation of state (EOS), $\Pi(\phi)$, for the experiment and model is possible for this case. Specifically, the Debye length of the suspension from which the EOS was obtained is identical to the Debye length of the Pe = 0.22 and 0.80 conditions (62 nm), and very similar to the Pe = 0.14 conditions (42 nm) (Table 1). However, the Debye length of the Pe = 1.07 suspension system is more than three times larger (199 nm). It is likely that the significant difference in Debye lengths between the Pe = 1.07 and the other systems explains some of the discrepancy between model and measurements at Pe = 1.07. That is, the larger diffuse double layer in the experiments would prevent the particles from packing as

densely as the model – parameterized with a smaller diffuse double layer – would predict. (This effect is not accounted for by using an effective volume fraction based on the double layer thickness for the modeling. This approach likely fails because of the effects of double layer compression at high volume fraction.) Additionally, non-equilibrium effects, as addressed in the Discussion, might also lead to a discrepancy between model and experiment.

In Fig. 9, the electrode volume fraction declines during relaxation. Relaxation occurs very rapidly at the boundary between the dense deposit and the dilute bulk solution due to the large gradient in osmotic pressure at this boundary. Particles buried within the deposit remain kinetically trapped until the particles layered on top of them have diffused into the bulk solution. Once the deposit is sufficiently diluted by this initial mechanism, relaxation is slow because of the reduction in the magnitude of the osmotic pressure gradient. At long times, the volume fraction returns to the initial value of 2%; however, in all cases the relaxation volume fraction never decays below 15% in duration over which images were recorded. The transport modeling supports this initial fast relaxation followed by a slow return to homogeneity.

At Pe = 0.14 and 0.22, the measured relaxation kinetics are well modeled by eqn (1). The model's predictions reside near the upper limit of the error at early and intermediate times at Pe = 0.22, and are in good agreement at late times. At Pe = 0.80, the model lags the measured kinetics at early and intermediate times, but predictions and measurements are in better agreement at late times. At Pe = 1.07, the model significantly lags measured kinetics at all times, although the discrepancy is moderated at late times.

The model lags the measured kinetics at Pe = 1.07 due to the discrepancy in the initial condition. For the model, the $\phi(z, t_{rel} = 0)$ initial condition is as predicted by the model at the end of deposition – just before the field is turned off and the relaxation begins. The accuracy of this

initial condition therefore depends on the accuracy of the model at late deposition times, which is itself in error, as discussed previously. The larger model initial condition has two effects that contribute to error in the relaxation. First, the number of colloids in the near wall region that must now diffuse away into the bulk is larger in the model than the experiment. Second, the osmotic pressure gradient available to drive colloids away from the near wall region is lower in the model than in the experiment because of the flat volume fraction profile in this region.

An interesting feature of the Fig. 9 results is the time scale required for appreciable deposition to occur. This time scale varies with Pe number. To further quantity this aspect of the deposition, Fig. 10 plots the time needed for $\phi_{electrode}$ to reach 95% of its final value for each Pe condition, here called, t_{SS}. This characteristic time is plotted for both the experiments and model. t_{SS} decreases with Pe by approximately an order of magnitude from Pe = 0.14 to Pe = 1.07 for both experimental measurements and the model. At high Pe (Pe = 0.80 and 1.07), experiments and theory both predict a characteristic steady-state time between 10 and 20 minutes. At low Pe (Pe = 0.14 and 0.22), there is a discrepancy between the measured and modeled characteristic steady-state time. Measurements predict t_{SS} = 65 minutes and 105 minutes for Pe = 0.14 and 0.22, respectively, while eqn (1) predicts t_{SS} = 136 minutes and 360 minutes.

The discrepancy in the model at low Pe potentially identifies errors in the characterization of the three material properties and functions that control the time scale for the field-assisted assembly. These parameters are the equation of state ($\Pi(\phi)$), the sedimentation function, $K(\phi)$, and the electrophoretic velocity, U_0. The first and last parameters were directly measured; $K(\phi)$ was taken from the literature. The agreement in measured Debye lengths between the particle-solvent systems used at low Pe (where there is a discrepancy in t_{SS}) and at

Pe = 0.80 (where the t_{SS} prediction is accurate) indicate that $\Pi(\phi)$ is unlikely to be the cause of this discrepancy. To test if uncertainty in $K(\phi)$ might explain the discrepancy at low Pe, we varied $K(\phi)$ by varying the exponent, K_2 , and found only a small effect of this variation on the eqn (1) solutions (c.f. Fig. 11). However, as shown in Fig. 9, uncertainty in U_0 has a significant effect on the performance of eqn (1) at low Pe numbers. Thus, small errors in U_0 can significantly affect the t_{SS} characterization at low Pe.

Fig. 12 and 13 report the spatial variation in the volume fraction at different time points and Pe conditions, for the cases of deposition and relaxation, respectively. The spatial range is $0 \leq z \leq 20$ μm. Similar to $\phi_{electrode}$ behavior observed in Fig. 9, particles accumulate very rapidly in the near-electrode region, especially at high Pe. The rate of deposition then slows due to a) an increase in osmotic pressure as more particles deposit, and b) retardation of particle mobility in the concentrated deposits. Specifically, significant increases in ϕ are seen across all positions within the first hour of deposition at Pe = 0.14 and 0.22, yet negligible changes in ϕ are seen in the last hour. Likewise, significant increases in ϕ are seen across all positions within the first 15 minutes of deposition at Pe = 0.80 and Pe = 1.07, yet little change in ϕ is observed in the last 30 minutes at Pe = 0.80 and in the last 10-15 minutes at Pe = 1.07. As a result of this kinetic behavior, $\phi(z)$ profiles become nearly flat at later times, especially at the lowest Pe. This behavior is a consequence of the divergent behavior of $Z(\phi)$ at high ϕ (Fig. 2b).

The model's solutions (curves) show good agreement with experimental measurements (data points) at Pe = 0.14 (Fig. 12a) and Pe = 0.22 (Fig. 12b) at all positions and times. At Pe = 0.80 they agree with the experiments at low z-positions and all times (Fig. 12c). However, the agreement is only fair at higher z-positions and later times. At Pe = 1.07, the model's solutions

are in good agreement with experimental measurements only at very early times – t_{dep} = 1 minute – but then overshoot the measurements at all later positions and times (Fig. 12d).

Fig. 13 shows $\phi(0 \leq z \leq 20\ \mu m, t_{rel})$ at all Pe conditions. $\phi(z)$ profiles are relatively flat, independent of z-position, at all times during relaxation, as compared to their shape at early times during deposition. The measured volume fraction across all z-positions drops much more significantly in the first five minutes than in the remaining tens of minutes of relaxation, at Pe = 1.07. By comparison, the $\phi(z)$ profile at Pe = 0.14, 0.22, and 0.80 after 5 minutes of relaxation differs only marginally from the initial condition, because the top-most portion of deposits at these conditions (z ~ 20 microns) are much denser at the onset of relaxation than are deposits at Pe = 1.07. Therefore, less time is required for particles to be released into the bulk fluid region at Pe = 1.07 than at the other Pe conditions. In Fig. 13, measured $\phi(z)$ profiles are somewhat noisy (i.e. jagged), at initial times, likely due to discretization effects; however, the level of agreement between model and experiment can still be assessed at later times.

The driving force for relaxation is the gradient in osmotic pressure between the dense deposit and the bulk fluid. As relaxation proceeds, this gradient diminishes, and thus, so does the rate of relaxation. At low volume fraction, a characteristic time scale for this relaxation is $t \sim H^2/D_0$, where H is the ~ 1 mm gap between the electrodes. The initial volume fraction in the electrode gap (2%), the ~ 20% volume fraction after the initial rapid volume fraction depletion, and the 1 mm electrode gap suggest a deposit height that decays from h ~ 100 microns in this slow relaxation period. Thus, given the free particle diffusivity of ~ 0.265 $\mu m^2/s$, the second step of the relaxation, when osmotic pressure gradients are low, requires a duration on the order of tens of days.

2.4.4 Propagation of crystallinity during deposition

The propagation of long-range, crystalline ordering is observed at Pe = 0.14 and 0.22. Little to no long-range order was observed at Pe = 0.80 or 1.07. At Pe = 0.14 and 0.22, the order is generated by the propagation of a crystalline front along an axis perpendicular to the electrode surface, as shown in Fig. 14a-e for Pe = 0.22. The dotted line indicates the position of the crystalline front. Such one-dimensional (1D) propagation of crystallization has been previously reported for the case of gravitational sedimentation. [22] After the electric field is turned off, crystallinity persists near the electrode surface for tens of minutes. By 90 minutes, disorder has been reestablished at all axial positions.

The position of the crystalline transition front (marked by the dotted line in Fig. 14a - 14e) – henceforth called h_{front} – is plotted in Fig. 15a,b for the Pe = 0.14 and 0.22 conditions, respectively. For both conditions, there is an onset period, of duration tens of minutes, during which crystallization is not observed, likely because the particles must concentrate sufficiently before crystal growth can occur. After this onset period, h_{front} grows at a nearly constant rate. Linear regression of the measurements yields a growth rate of 95 nm/min at Pe = 0.14 and 198 nm/min at Pe = 0.22. These rates are comparable to growth rates of ~100 - 300 nm/min reported for sedimentation. [22] Davis et al. modeled this propagation with classical nucleation theory. In this treatment, the rate at which amorphous particles add to the growing crystal depends on the difference in chemical potential between the crystalline and amorphous regions and the Brownian dynamics of the colloids at the conditions of the front.

The solid curves in Fig. 10a,b are loci in time and height of constant colloid volume fraction for the two Pe studied, as predicted by eqn (1). These model curves can be used to evaluate if the time-height dependence of the experiments correspond to a characteristic, constant volume fraction. At Pe = 0.14, the experimental $h_{front}(t)$ is largely bounded by propagation characteristics of $\phi = 0.35$ and $\phi = 0.37$. At Pe = 0.22, $h_{front}(t)$ approximately tracks the characteristic curve for $\phi \underline{=} 0.33$. Combining the two conditions, the crystal front maintains a volume fraction between $\phi = 0.33$ and $\phi = 0.37$.

To further investigate the possibility that the crystalline front propagates at a condition of nearly constant volume fraction, ϕ at each measured h_{front} position and time is plotted in Fig. 15c (Pe = 0.14) and d (Pe = 0.22) for the cases of both direct experimental characterization by image analysis (data points) and by the transport model (curves). The data points end at 20 μm, the upper limit at which ϕ was measured by image processing. Except at the initial point, the experimentally measured volume fraction of the crystal front is relatively flat for Pe = 0.14 and slightly decreasing for Pe = 0.22.

Fig. 15 therefore suggests that the volume fraction of colloids at the crystal front is constrained in a relatively narrow band centered on about $\phi = 0.34$. This result is consistent with: (i) equilibrium fluid-crystalline phase transitions reported for PHSA-PMMA spheres of $\kappa R \sim 6$ in literature ($\phi \sim 30\%$) [38]; (ii) our own equilibrium crystallization measurements for this colloid-solvent system, conducted in rectangular capillaries for a duration of two months.

The crystal front thus propagates along a characteristic of nearly constant volume fraction that is within the equilibrium coexistence region. Therefore, the rate of 1D crystalline growth can be predicted in DC electric field assembly by means of eqn (1) if this crystallization volume

fraction has been independently measured. The crystallization comparison thus demonstrates the scope for using the model to directly predict the kinetics of time-dependent colloidal assembly by steady electric fields. What is required is measurement of the colloid equation of state (Fig. 3), the electrophoretic mobility at the condition of deposition (Table 1), and the coexistence volume fraction of the system. Independent characterization of these material functions therefore yields, by means of eqn (1), a no adjustable parameter prediction of the deposition, assembly, and crystallization of the colloids in steady-electric fields.

2.5 Discussion & Conclusions

The results of this study address questions about the kinetics of colloidal assembly in steady electric fields, including the scope for their modeling by transport theory. Here we address: (i) if the continuum approximation inherent in eqn (1) is valid for the case of the thin ~ 50 μm deposits generated here; (ii) if the operating window for deposition comprises a region in which crystallization can occur; (iii) if the available characterizations of the equation of state and electrophoretic velocity are sufficient to model the experimentally observed deposition structures.

The continuum description of eqn (1) is potentially at odds with the fact that thin deposits were produced. Such thin deposits facilitate reconfiguration between crystalline and non-crystalline states, with cycle times ~ 120 minutes observed in the experiments reported here. For these thin deposits, colloid volume fractions were determined as an average of intervals that were four particle layers deep. At this resolution scale it is arguable that effects of the discrete layers might invalidate continuity of the osmotic pressure and its gradients, which appear as terms in

eqn (1). However, both the measured and modeled volume fraction profiles were found to vary smoothly, and the agreement between the two is fair to good. Thus, even though the deposits modeled are never more than about 100 particle layers thick, the continuum descriptions of eqns (1) – (3) are sufficient to capture the deposition and relaxation kinetics, even when crystalline deposits are formed at low Pe number. One case for which the ~ four layer resolution limit might complicate interpretation of the measurements is for the behavior of the crystal front. The volume fraction of the front was consistent with reports of the equilibrium coexistence region. However, the spatial resolution of the volume fraction characterization is such that both amorphous and crystalline sides of the boundary contribute to the front volume fraction plotted in Fig. 15 c,d. That is, the spatial resolution of the experiments was not sufficient to observe a discontinuity in the volume fraction at the front boundary, as would be expected for local equilibrium, and as has been seen for the case of sedimentation in thick specimens. [8,23]

The weakest electric fields applied (Pe = 0.14 and 0.22) were still large enough to generate sufficient osmotic pressure for crystallization. Eqn (1) predicts even greater propensity for crystallization at the two higher Pe studied, Pe = 0.80 and Pe = 1.07, because the osmotic pressures generated at the electrode by these applied field are even greater than the low Pe experiments. However, this expectation was not borne out by the experiments, because little to no colloidal crystallization was observed at these two high Pe number conditions. The presence of long-range crystalline ordering at low Pe numbers is consistent with other field-assisted assembly observations. [3,6,9,22]

For the higher Pe number experiments, the volume fraction of the deposit is lower than theory would predict. Moreover, although the measured volume fraction is in a region for which crystallization is observed at equilibrium, no order was found in the deposits. Non-equilibrium

effects could modify the deposition in two ways. First, non-equilibrium effects could generate (metastable) structures that do not conform to the Fig. 3 equation of state. This effect would contribute to, for example, an observed volume fraction that was lower than predicted by eqn (1). Second, jamming or vitrification could prevent the initially amorphous deposits from transforming into crystalline structures at the volume fraction at which they are deposited. Fig. 9d appears to indicate that both effects are relevant to explaining the results at high Pe number.

The comparison between the measurements and model relies on the availability of accurate functions used by the model - U_0, $\Pi(\phi)$, and $K(\phi)$. We first consider possible errors in $K(\phi)$. At low Pe the deposition leads to colloidal crystals; $K(\phi)$ in this case would differ from the functions used, which were taken as those for amorphous conditions. However, switching $K(\phi)$ to one appropriate for a periodic arrays of spheres has a negligible effect on the modeling solutions (c.f. Fig. 11).[35] In addition, model results are comparatively insensitive to the parameterization of $K(\phi)$ during deposition because varying this function has little effect on eqn (1) solutions during deposition. However, the model results *are* sensitive to the functional form of $K(\phi)$ during relaxation (c.f. Fig. 11). Specifically, the K_2 appropriate for electrophoretically deposited spheres (K_2 = -1.0) captures the initial fast relaxation in density that is observed experimentally better than the value that should apply in the absence of an electric field (K_2 = -6.55). This result is surprising, because voltage is not applied during relaxation. Either this agreement is coincidental or, alternatively, in the early period after the voltage is removed, there might be a residual electrophoretic driving force colloids away from the substrate, because of charged ionic species that would have accumulated at the surface.

Measurement errors in determining the equation of state, $\Pi(\phi)$, from the steady-state results such as Fig. 3 are, on the other hand, an important consideration for accurate modeling.

Specifically, in the thin deposits (~ 50 μm and less) of interest here, $\phi(z)$ decays from a high to low value in a very small region at the top of the deposit, as shown qualitatively in Fig. 3a. This physics translates into a sparse characterization of the equation of state at low volume fractions, as shown by the spacing of the datum points in Fig. 3b. The volume fraction region with high osmotic pressure does not suffer from this problem – this region of the equation of state is more densely populated with data. However, a different concern arises in this case – because the osmotic pressure is such a rapidly varying function here, the precision of the colloid volume fraction, as determined by the image analysis, could affect the accuracy of the equation of state. Additionally, the measured equation of state does not show evidence of a phase transition; it was probably not observed because of the rapid variation of $\Pi(\phi)$ in the thin sediment. Eqn (3)'s continuous behavior, as is required for our numerical methods, also does not show evidence of a phase transition. Model results are sensitive to the steepness of the divergence of $Z(\phi)$ at high volume fraction (c.f. Fig. 16), and this degree of steepness likely depends on the exact location of the phase coexistence boundary. These effects on the quality of the equation of state characterization are an important factor in the performance of the modeling.

Finally, direct measurement of U_0 (c.f. section 2.4.2) from the deposition experiments themselves is recommended because it yields a characterization of U_0 under the exact conditions of the field-assisted assembly. Even given this characterization, however, the sensitivity analysis plotted in Fig. 9 indicates that modest errors in the characterization of the particle's electrophoretic velocity become an important determinant of model performance at low Pe number conditions. Nevertheless, the fair to good agreement between modeling and experiments supports use of these methods to parameterize $K(\phi)$, $\Pi(\phi)$, and U_0 in eqn (1) so as to predict deposition, relaxation, and crystallization kinetics by steady-electric fields.

The crystalline deposits produced at Pe = 0.14 and 0.22 were tens of microns thick; other work has shown that this thickness is sufficient for applications such as sensing and structural color. [11-15,20] The time scales for deposition and relaxation, as well as for crystallization are also potentially sufficient for such applications. Dense deposits were achieved in tens or hundreds of minutes, and crystallization was observed in tens of minutes. Moreover, the strength of the steady electric field can be varied to control these times scales. The time needed to switch between crystalline and noncrystalline deposits is a key design parameter for applications of reversible assemblies. Our work shows that the steady-state electric fields used here can cycle between order and disorder on time scales ~ 90 min. This work therefore delineates parameter ranges in which direct current electric field assembly can be used to generate time-dependent colloidal crystallization. It furthermore shows that eqn (1) may be used to model assembly dynamics in such devices and processes. Our method of characterizing crystallinity propagation through the position of h_{front}, while successful in quantifying crystal growth rates, does not characterize the quality of the crystalline structure. In future work, the application of local measures of bond orientation would be a possible way to address this question. [9,39-41]

We have therefore measured the assembly kinetics of charged colloids in steady electric fields. A one-dimensional transport model yields fair to good agreement with the measurements. Whereas little to no crystallization was observed at Pe = 0.80 and 1.07, crystalline order propagated upwards from the electrode at Pe = 0.14 and 0.22. The propagation was along a characteristic of constant volume fraction; the particular volume fraction of propagation was consistent with equilibrium measurements of fluid-crystal coexistence. By establishing operating ranges for colloidal deposition, assembly, and crystallization, and by demonstrating the connection of these phenomena to equilibrium thermodynamics and one-dimensional transport

theory, the experiments and modeling inform the design of processes to generate colloidal materials that are active and reversible**.**

System	[TBAC] (mM)	λ_0 (S/m)	U_0/E ($m^2/s/V$)	ζ (mV)	κ^{-1} (nm)	i (nA)	$K_{2,\ deposition}$	$K_{2,\ relaxation}$
Pe = 0.14	2	$1.0 * 10^{-5}$	$(9.65 \pm 2.61)*10^{-10}$	90	42	10	-1	-6.55
Pe = 0.22	1	$4.5 * 10^{-6}$	$(7.16 \pm 1.03)*10^{-10}$	65	62	10	-1	-6.55
Pe = 0.80	1	$4.5 * 10^{-6}$	$(8.48 \pm 1.36)*10^{-10}$	65	62	30	-1	-6.55
Pe = 1.07	1	$4.4 * 10^{-7}$	$(3.33 \pm 0.62)*10^{-10}$	25	199	10	-1	-6.55
$Z(\phi)$	1	$4.5 * 10^{-6}$	$(6.92 \pm 1.49)*10^{-10}$	118	62	30	-1	-6.55

Table 2-1. Parameters of particle-solvent systems used at each condition of Pe number. A_2 and K_2 determined from Russel et al. (1989) Chapters 10 and 12, respectively. [36]

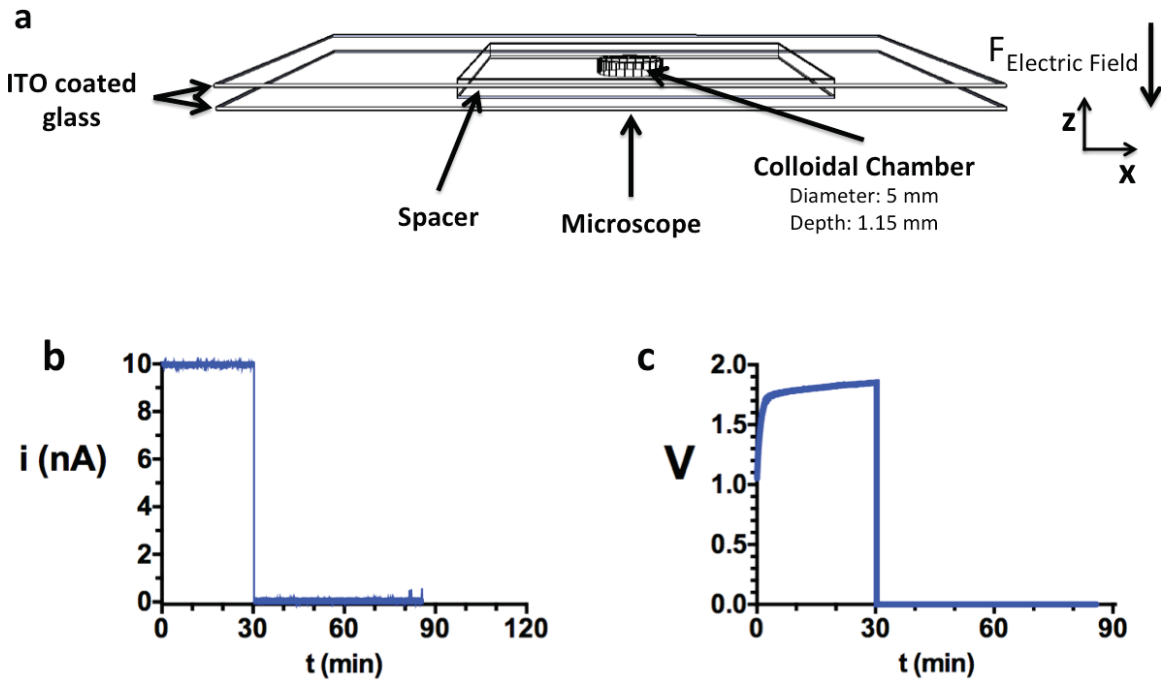

Figure 2-1. Schematic and operating plots of DC electric field device. a) Schematic of device used to apply DC electric fields to initially uniform suspensions of colloidal spheres. The device, developed by Shah et al., [3] has an electrode gap of 1.15 mm. b) current vs time and c) voltage vs time plots for a galvanostatic electric field applied from 0-30 minutes and then removed from 30-90 minutes.

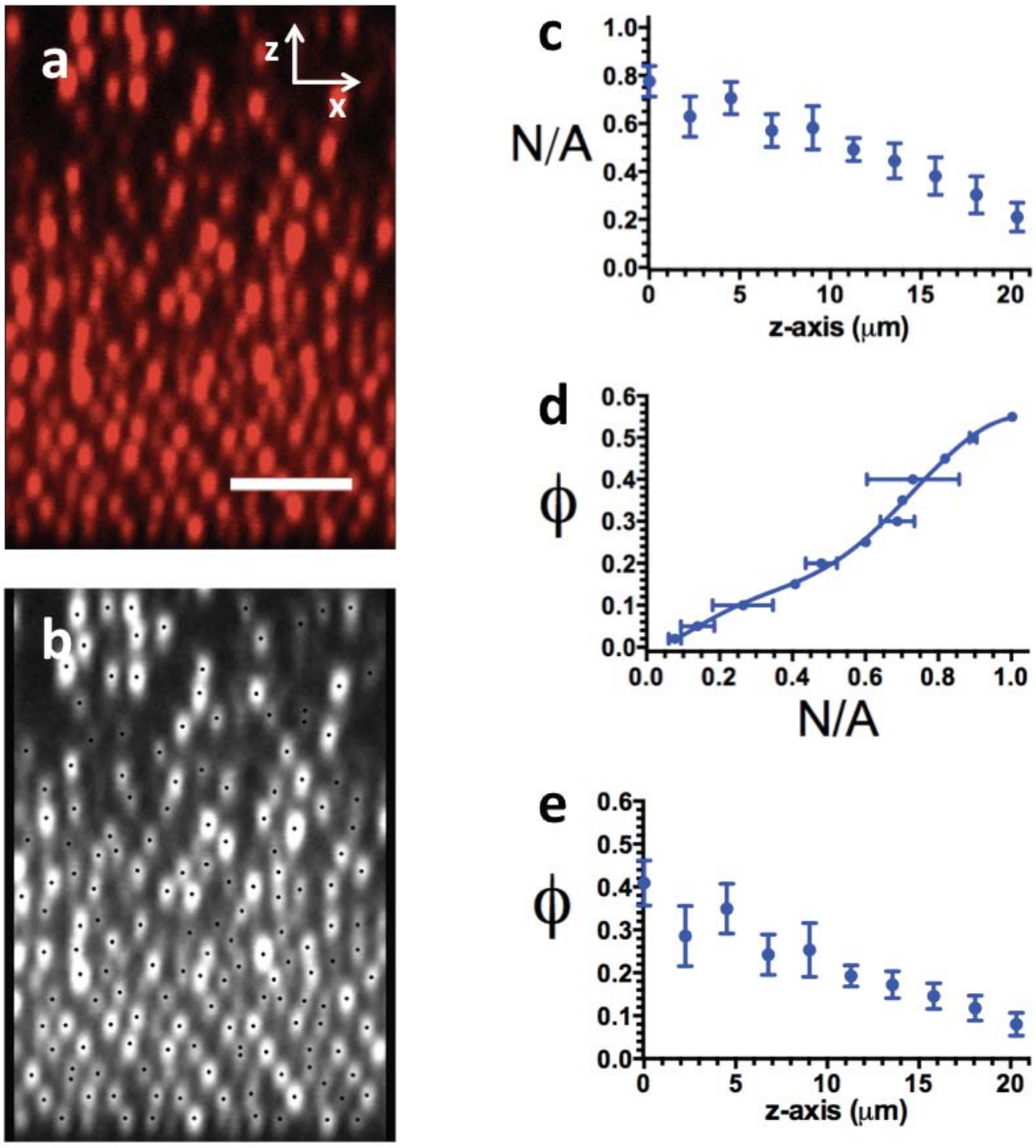

Figure 2-2. Determination of ϕ(z) from 2D CLSM images. a) Raw 2D CLSM image and b) particle centroids identified from it by image analysis. c) Particle number density in number of particles/μm^2 (N/A) is plotted vs distance along the discretized z-axis, where z = 0 corresponds to the electrode surface. d) Calibration of N/A to ϕ was fit with a polynomial function from which ϕ(z) was determined and plotted in (e). Scale bar is 5 μm.

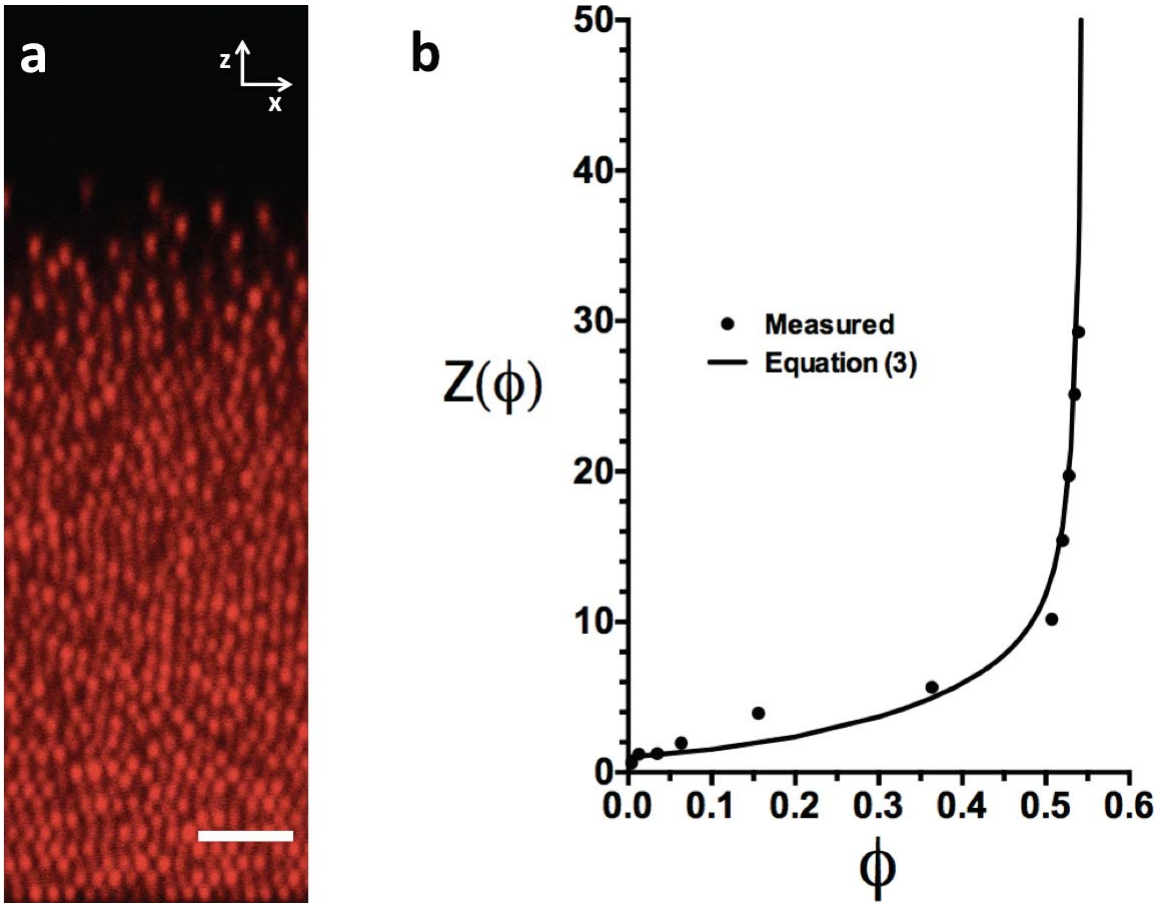

Figure 2-3. Z(ϕ) from steady-state profile of ϕ(z). a) PMMA spheres at ϕ_0 = 0.01 were deposited in a steady (E = 340 V/m) until a steady state in ϕ(z,t) was achieved. Scale bar is 5 μm. Eqn (2) was applied to these data to obtain Π(z), which is plotted as Z(ϕ) in b. The curve is the fit to eqn (3) with parameters as given in the text.

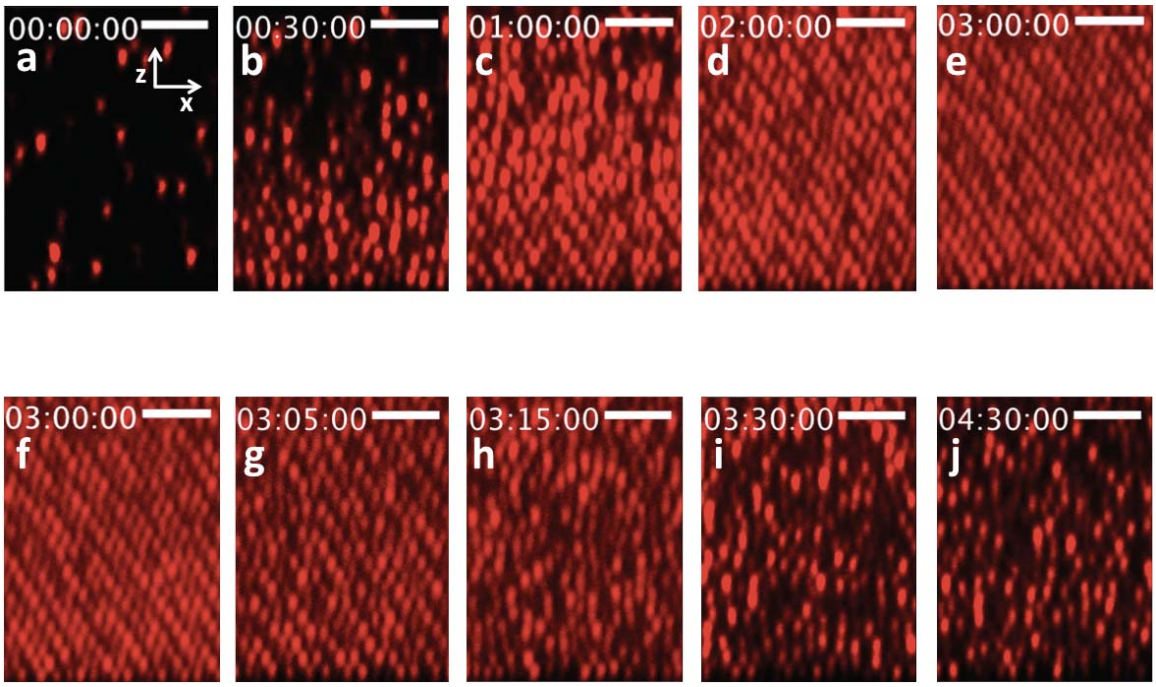

Figure 2-4. CLSM images of DC electric field-assisted colloidal assembly at Pe = 0.22. Deposition (a-e) and subsequent relaxation of this structure upon removal of the field (f-j). a) just prior to application of the steady field; b) 30 minutes after application; c) 1 hour; d) 2 hours; e) 3 hours. f) relaxation at the moment of field removal; g) 5 minutes after removal of field; h) 15 minutes; i) 30 minutes; j) 90 minutes. Scale bar is 5 μm.

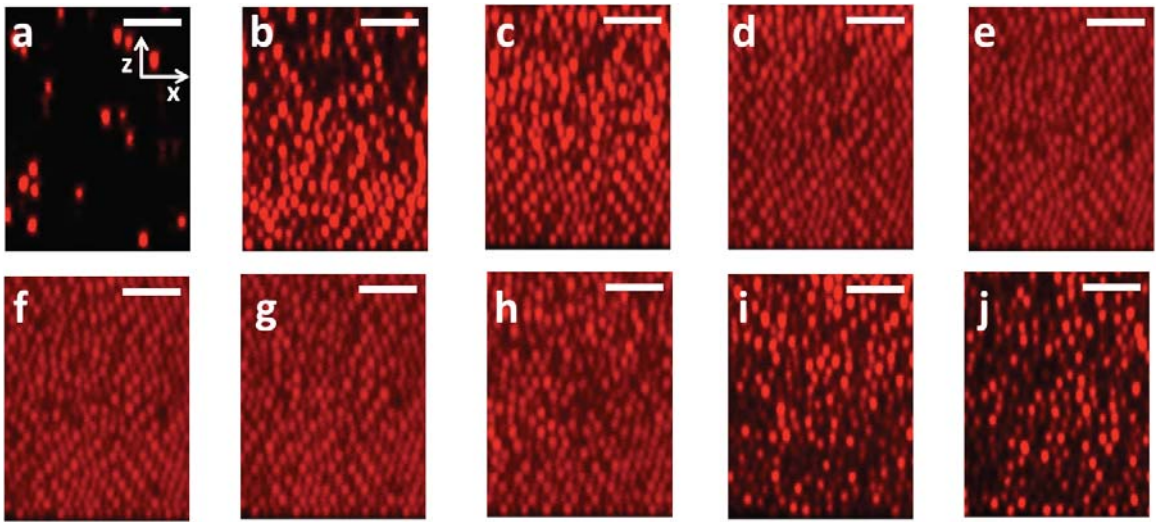

Figure 2-5. CLSM images of DC electric field-assisted colloidal assembly at Pe = 0.14. Deposition (a-e) and subsequent relaxation of this structure upon removal of the field (f-j). a) just prior to application of the steady field; b) 30 minutes after application; c) 1 hour; d) 2 hours; e) 3 hours. f) relaxation at the moment of field removal; g) 5 minutes after removal of field; h) 15 minutes; i) 30 minutes; j) 90 minutes. Scale bar is 5 μm.

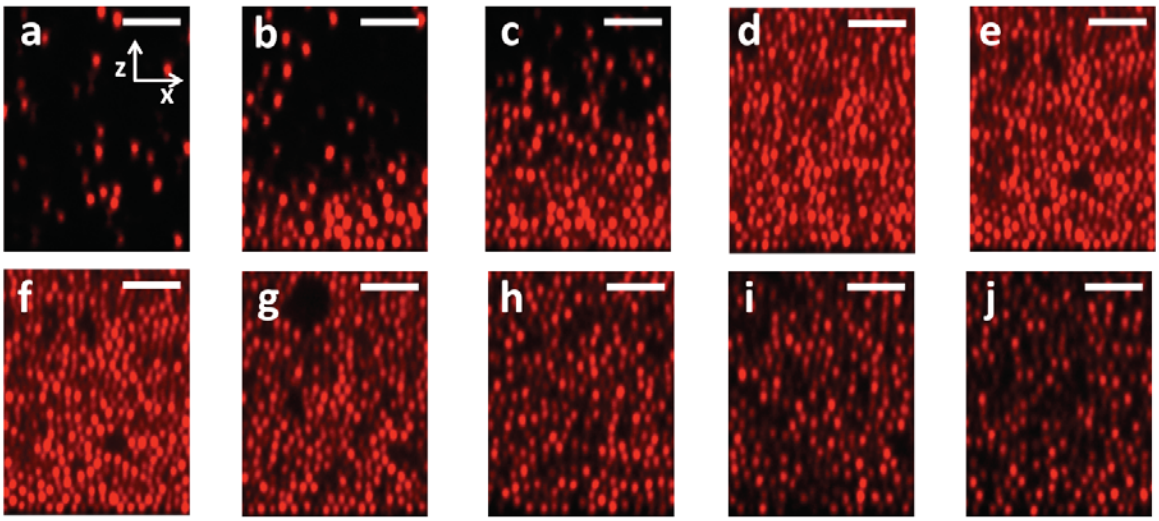

Figure 2-6. CLSM images of DC electric field-assisted colloidal assembly at Pe = 0.80. Deposition (a-e) and subsequent relaxation of this structure upon removal of the field (f-j). a) just prior to application of the steady field; b) 30 minutes after application; c) 1 hour; d) 2 hours; e) 3 hours. f) relaxation at the moment of field removal; g) 5 minutes after removal of field; h) 15 minutes; i) 30 minutes; j) 90 minutes. Scale bar is 5 μm.

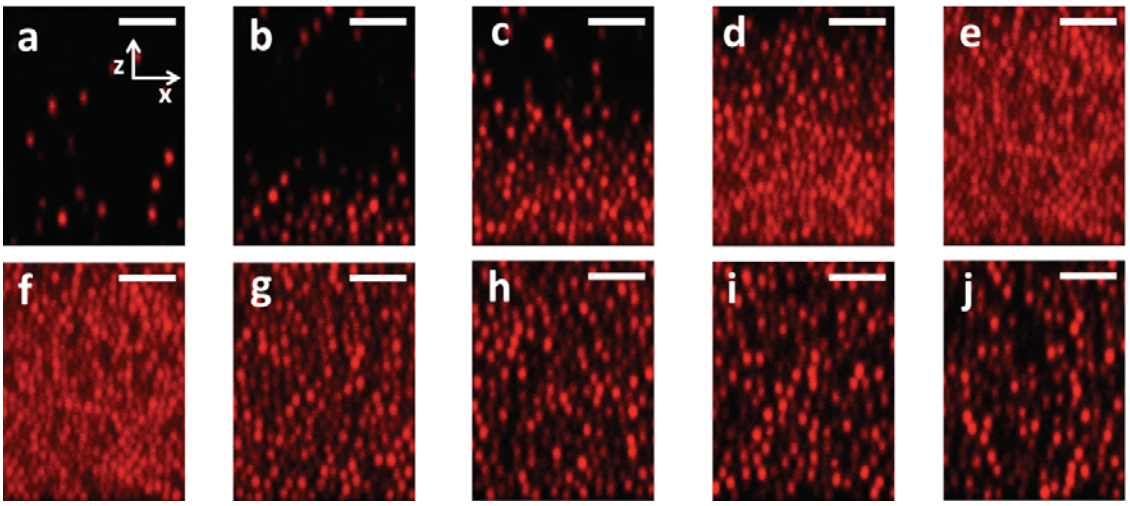

Figure 2-7. CLSM images of DC electric field-assisted colloidal assembly at Pe = 1.07. Deposition (a-e) and subsequent relaxation of this structure upon removal of the field (f-j). a) just prior to application of the steady field; b) 30 minutes after application; c) 1 hour; d) 2 hours; e) 3 hours. f) relaxation at the moment of field removal; g) 5 minutes after removal of field; h) 15 minutes; i) 30 minutes; j) 90 minutes. Scale bar is 5 μm.

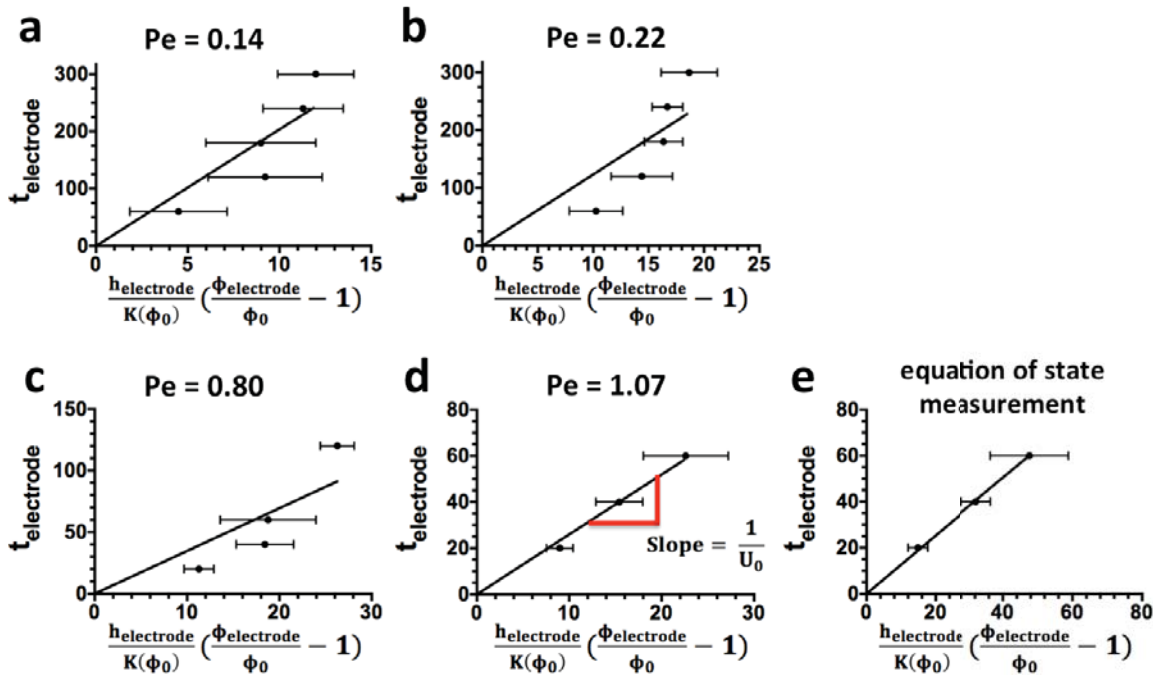

Figure 2-8. Analysis of early time deposition results to determine U_0. a) Pe = 0.14, b) Pe = 0.22, c) Pe = 0.80, d) Pe = 1.07, and e) the equation of state characterization.

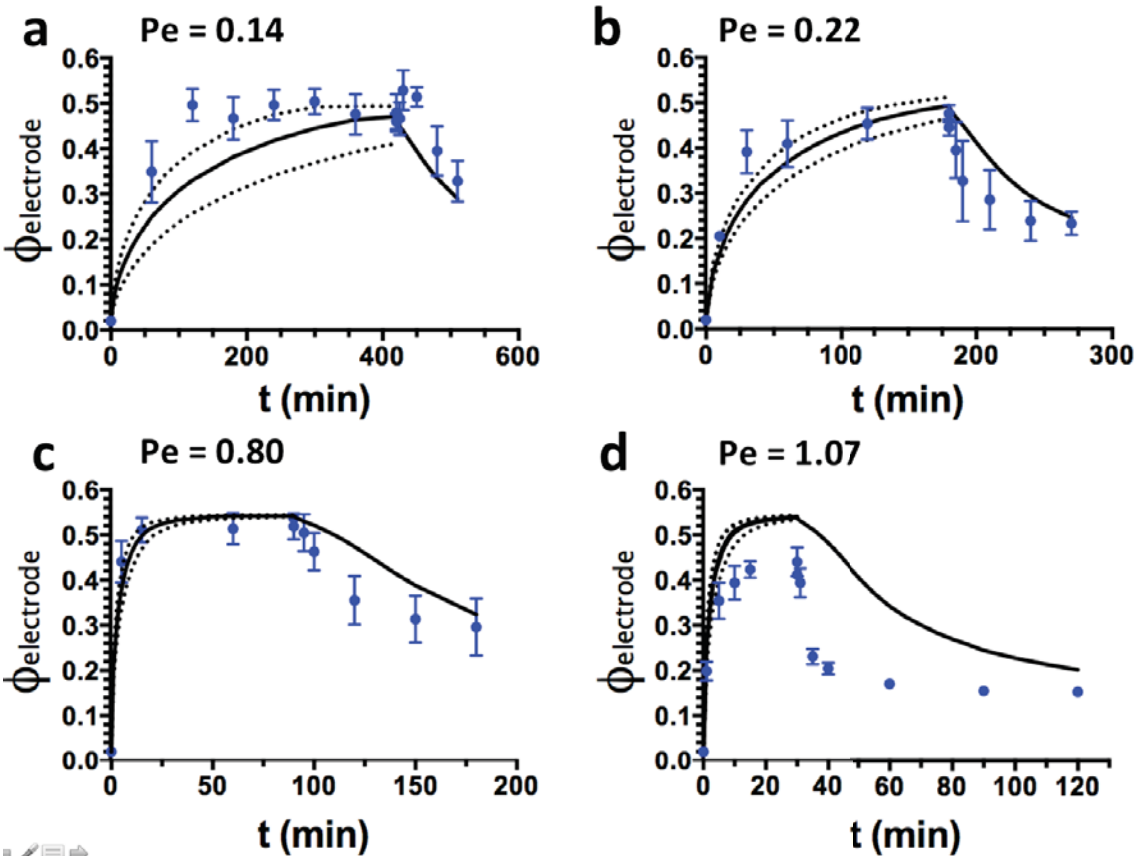

Figure 2-9. Electrode volume fraction, $\phi_{electrode}$, as a function of time. a) Pe = 0.14 b) Pe = 0.22 c) Pe = 0.80 and d) Pe = 1.07. Data points are measured values and curves are solutions to eqn (1). Dotted curves are model solutions for a standard deviation above and below the measured colloidal velocity in the steady electric field, U_0.

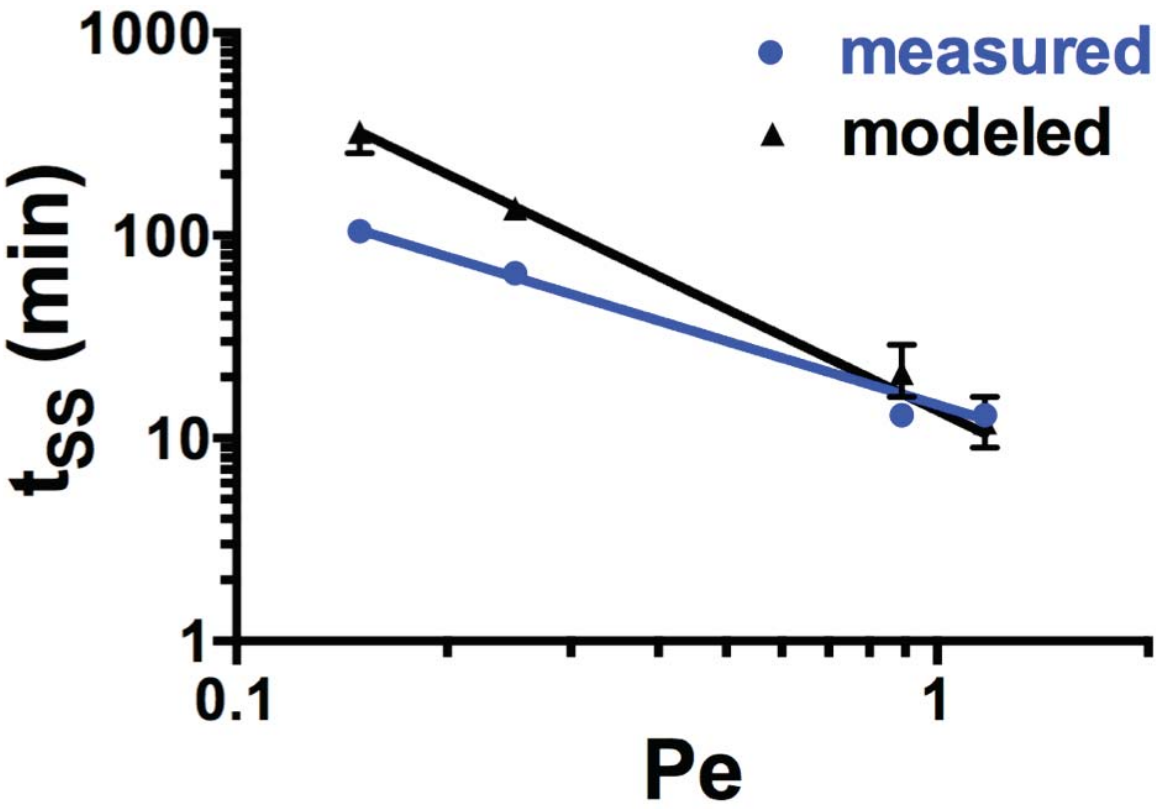

Figure 2-10. Characteristic times of deposition (t_{SS}) as a function of Pe. t_{SS} is the time needed for $\phi_{electrode}$ to reach 95% of its final value during deposition, as assessed from the results of Fig. 9. Blue data points are characteristic times for measurements, black data points are characteristic times for modeling. The curves are power laws: $t_{SS}(Pe) = 13.5 \times Pe^{-1.091}$ for the measurements and, $t_{SS}(Pe) = 16.2 \times Pe^{-1.568}$ for the model.

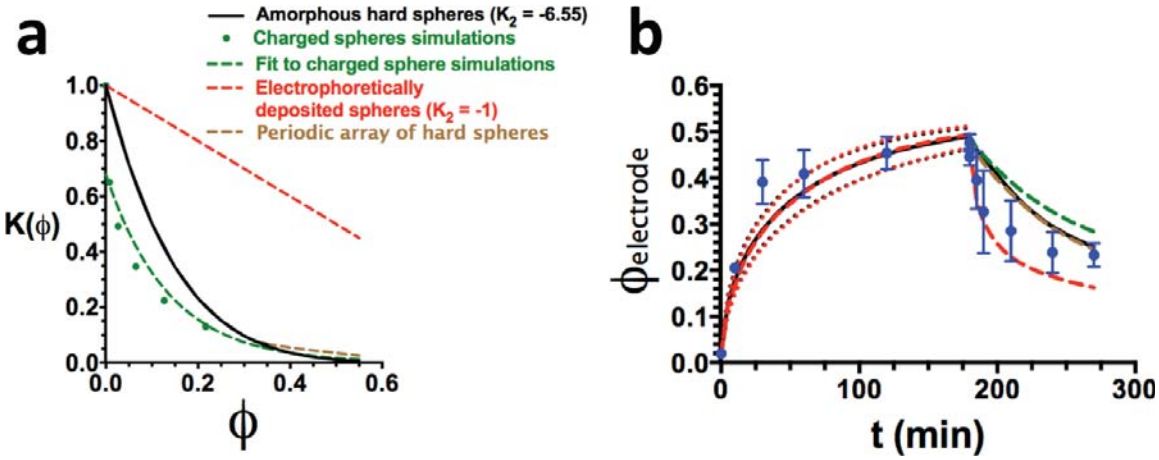

Figure 2-11. Comparison of mobility functions available for modeling, as parameterized by Table 1. a) $K(\phi)$ for hard spheres in the absence of an electric field (black, solid curve, $K(\phi) = (1-\phi)^{-K_2}$, $K_2 = -6.55$), for electrophoretically deposited spheres (red, dashed curve, $K(\phi) = (1-\phi)^{-K_2}$, $K_2 = -1$), for spheres in a periodic array (brown, dashed curve) as per the function reported in Sangani and Acrivos, [35] and charged spheres in the high charging limit (green data points) as reported in Gilleland et al., [32] and an empirical fit to these simulation points (green, dashed curve). b) Figure 2-9b ($\phi_{electrode}(t)$, Pe = 0.22) reports eq. (1) deposition predictions for various mobility functions appropriate to this Pe. Note that deposition predictions are relatively insensitive to the mobility formulation; however, the fast initial decay of volume fraction in the relaxation portion of the experiment is well modeled by $K_2 = -1$. Predictions for $K(\phi)$ for crystalline and for charged spheres differ only to small degree from those for amorphous hard spheres.

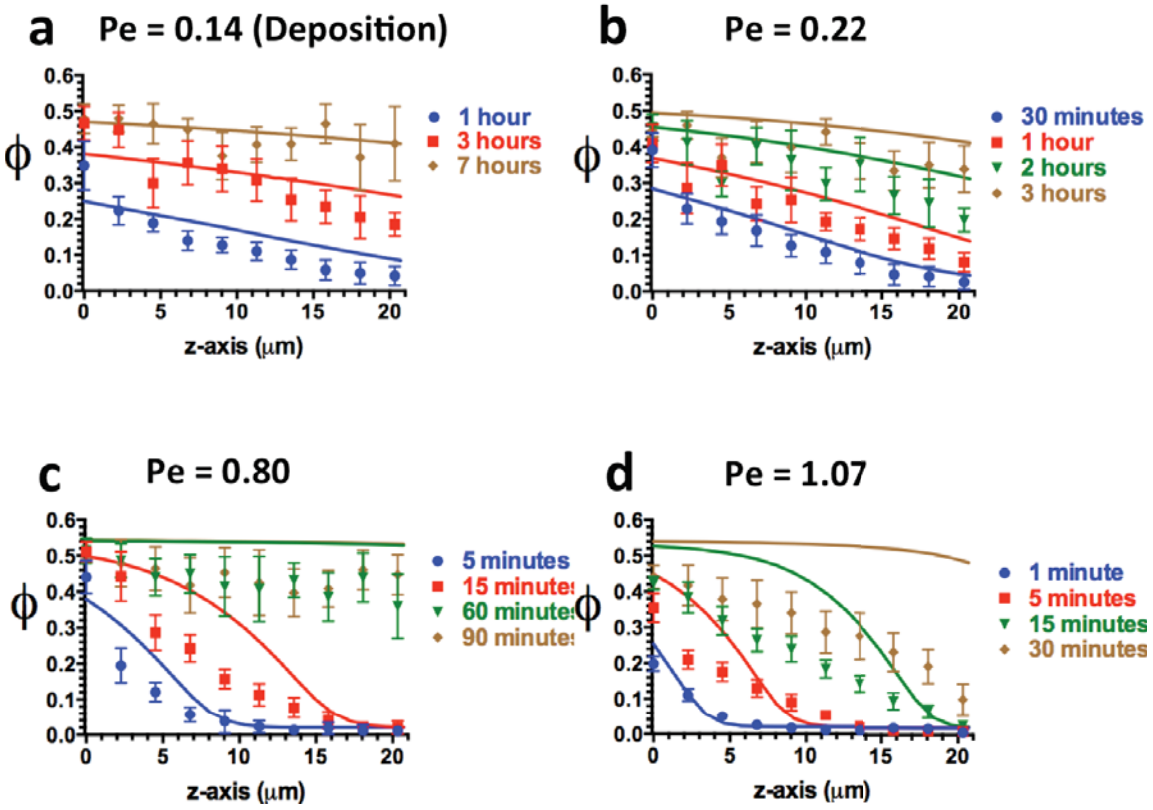

Figure 2-12. ϕ(z,t) during deposition. a) Pe = 0.14 b) Pe = 0.22 c) Pe = 0.80 and d) Pe = 1.07. The curves are solutions to eqn (1).

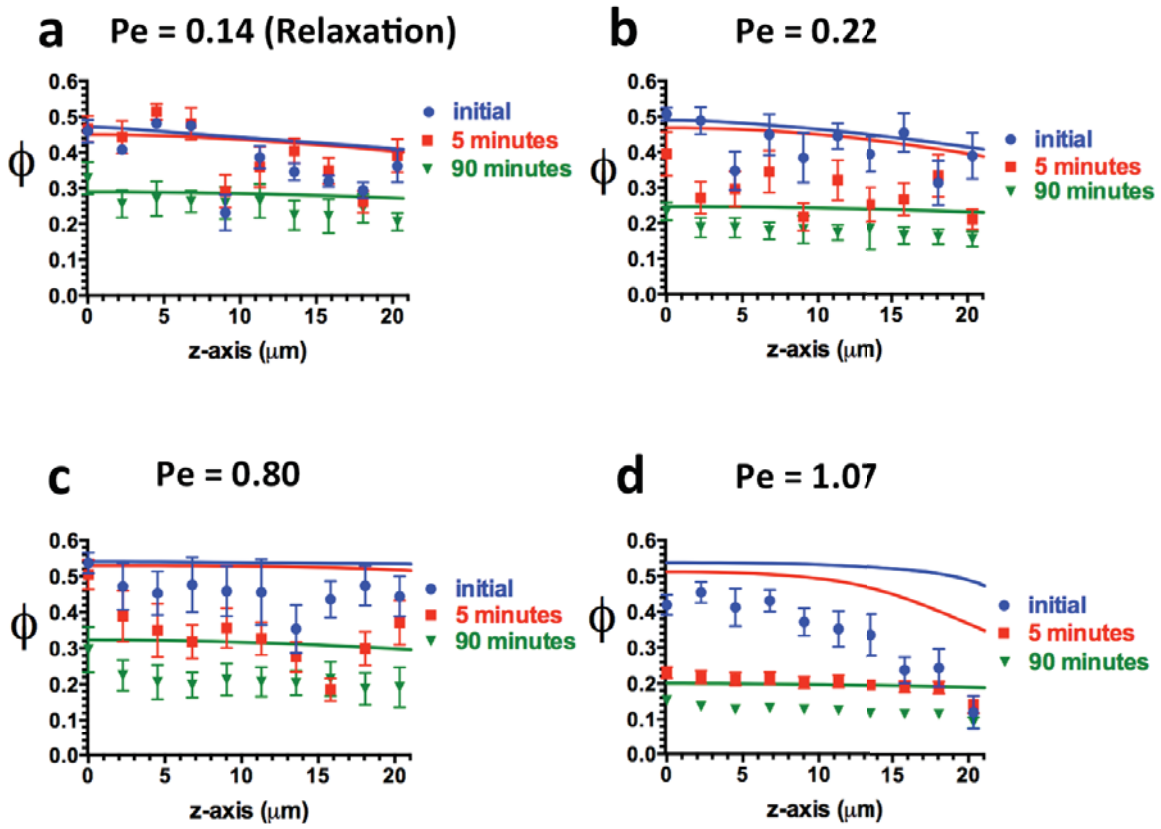

Figure 2-13. ϕ(z,t) during relaxation. a) Pe = 0.14 b) Pe = 0.22 c) Pe = 0.80 and d) Pe = 1.07. The curves are solutions to eqn (1).

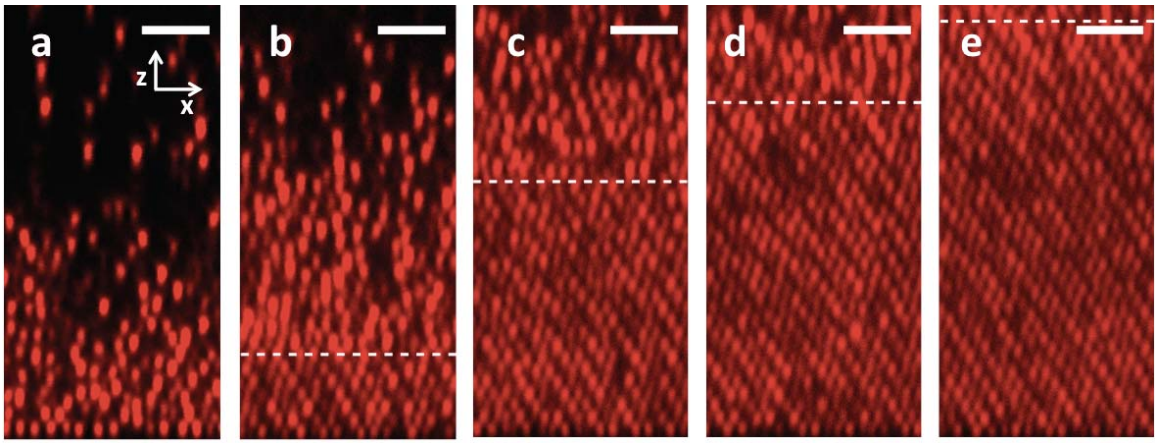

Figure 2-14. Propagation of crystallinity at Pe = 0.22. a) after 30 minutes of deposition; b) after 1 hour of deposition; c) 2 hours; d) 2.5 hours; e) 3 hours. The time-dependent location of the crystal front (h_{front}) is indicated.

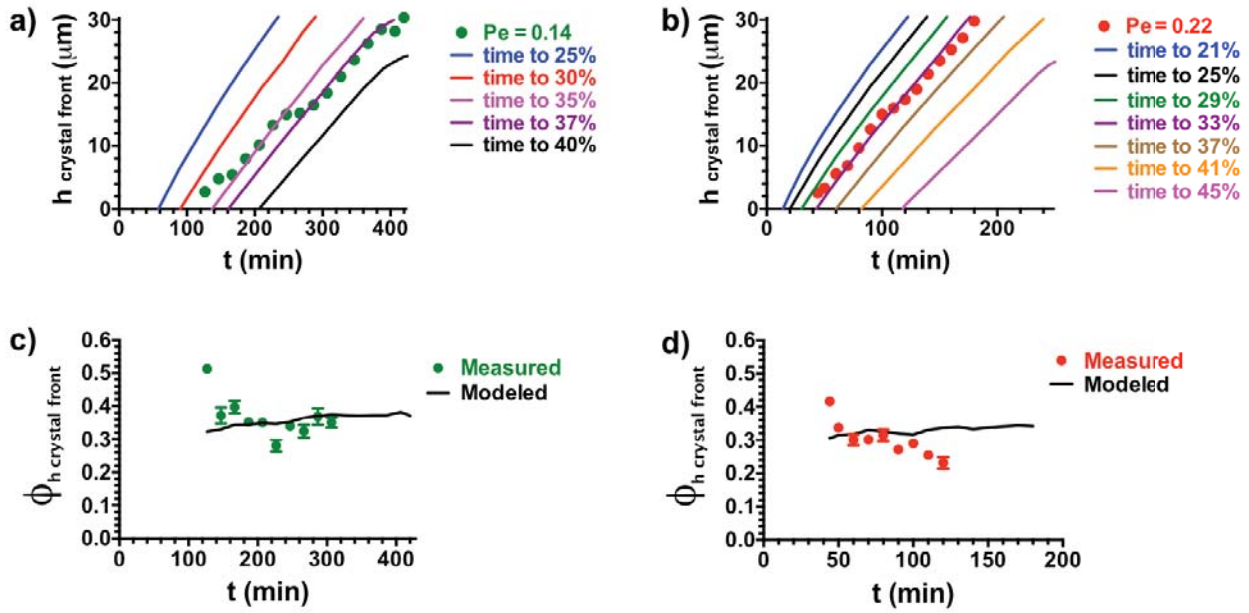

Figure 2-15. Time-evolution of h_{front} and $\phi_{crystalline}$. Time dependence of h_{front} compared lines of constant volume fraction, as predicted from the model for a) Pe = 0.14 and b) Pe = 0.22. The measured volume fraction, compared to the model, at the crystalline front boundary for Pe = 0.14 and Pe = 0.22 is plotted in c and d, respectively.

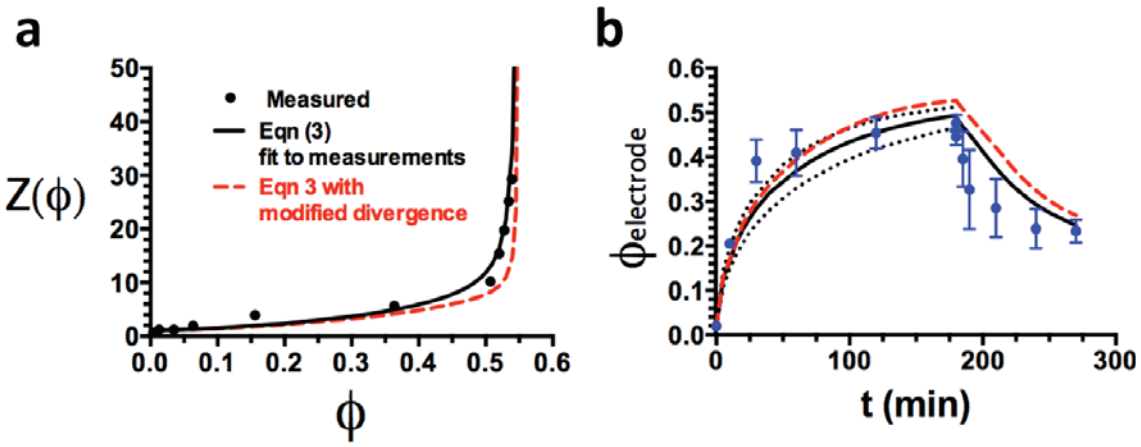

Figure 2-16. Sensitivity of model results to changes in Z(ϕ). a) Comparison of experimentally derived Z(ϕ) with an alternative functional form with a steeper divergence (dashed curve) so as to better approximate the crystalline branch of a phase transition. b) Predictions of eqn (1) for $\phi_{electrode}(t)$ for deposition and relaxation at Pe = 0.22 with the two compressibility models reported in (a). The different divergence behavior has modest effect on the predictions, particularly for the late stage of the deposition. The model parameter in eqn (3) for the alternative Z(ϕ) is $a_1=4-1.4/\phi_p$, where $\phi_p = 0.55$.

2.6 References

1. Colvin, V. L. From opals to optics: Colloidal photonic crystals. *Mrs Bulletin* **26**, 637-641 (2001).
2. Zhang, H., Yu, X. & Braun, P. V. Three-dimensional bicontinuous ultrafast-charge and -discharge bulk battery electrodes. *Nat Nanotechnol* **6**, 277-281 (2011).
3. Shah, A. A. et al. Liquid crystal order in colloidal suspensions of spheroidal particles by direct current electric field assembly. *Small* **8**, 1551-1562 (2012).
4. Gangwal, S., Pawar, A., Kretzschmar, I. & Velev, O. D. Programmed assembly of metallodielectric patchy particles in external AC electric fields. *Soft Matter* **6**, 1413-1418 (2010).
5. Mukhija, D. & Solomon, M. J. Translational and rotational dynamics of colloidal rods by direct visualization with confocal microscopy. *Journal of colloid and interface science* **314**, 98-106 (2007).
6. Jensen, K. E., Pennachio, D., Recht, D., Weitz, D. A. & Spaepen, F. Rapid growth of large, defect-free colloidal crystals. *Soft Matter* **9**, 320-328 (2013).
7. Davis, K. E. & Russel, W. B. An asymptotic description of transient settling and ultrafiltration of colloidal dispersions. *Physics of Fluids A: Fluid Dynamics (1989-1993)* **1**, 82-100 (1989).
8. Piazza, R. Settled and unsettled issues in particle settling. *Reports on Progress in Physics* **77**, 056602 (2014).
9. Shereda, L. T., Larson, R. G. & Solomon, M. J. Local stress control of spatiotemporal ordering of colloidal crystals in complex flows. *Physical review letters* **101**, 038301 (2008).
10. Ackerson, B. J. & Pusey, P. N. Shear-induced order in suspensions of hard spheres. *Phys Rev Lett* **61**, 1033-1036 (1988).
11. Arsenault, A. C., Puzzo, D. P., Manners, I. & Ozin, G. A. Photonic-crystal full-colour displays. *Nat Photon* **1**, 468-472 (2007).
12. Fudouzi, H. & Sawada, T. Photonic Rubber Sheets with Tunable Color by Elastic Deformation. *Langmuir Langmuir* **22**, 1365-1368 (2005).
13. Gong, T., Wu, D. T. & Marr, D. W. M. Electric Field-Reversible Three-Dimensional Colloidal Crystals. *Langmuir Langmuir* **19**, 5967-5970 (2003).
14. Marlow, F., Muldarisnur, Sharifi, P., Brinkmann, R. & Mendive, C. Opals: Status and Prospects. *Angewandte Chemie International Edition Angewandte Chemie International Edition* **48**, 6212-6233 (2009).
15. Shah, A. A., Ganesan, M., Jocz, J. & Solomon, M. J. Direct current electric field assembly of colloidal crystals displaying reversible structural color. *ACS Nano* **8**, 8095-8103 (2014).

16. Rogach, A. L., Kotov, N. A., Koktysh, D. S., Ostrander, J. W. & Ragoisha, G. A. Electrophoretic deposition of latex-based 3D colloidal photonic crystals: A technique for rapid production of high-quality opals. *Chemistry of materials* **12**, 2721-2726 (2000).

17. Kirby, B. J. *Micro- and Nanoscale Fluid Mechanics: Transport in Microfluidic Devices* (Cambridge University Press, 2013).

18. Bertone, J. F., Jiang, P., Hwang, K. S., Mittleman, D. M. & Colvin, V. L. Thickness dependence of the optical properties of ordered silica-air and air-polymer photonic crystals. *Physical review letters* **83**, 300 (1999).

19. Jiang, P., Bertone, J. F., Hwang, K. S. & Colvin, V. L. Single-crystal colloidal multilayers of controlled thickness. *Chemistry of Materials* **11**, 2132-2140 (1999).

20. Holtz, J. H. & Asher, S. A. Polymerized colloidal crystal hydrogel films as intelligent chemical sensing materials. *Nature* **389**, 829-832 (1997).

21. Auzerais, F. M., Jackson, R. & Russel, W. B. The resolution of shocks and the effects of compressible sediments in transient settling. *Journal of Fluid Mechanics* **195**, 437-462 (1988).

22. Davis, K. E., Russel, W. B. & Glantschnig, W. J. Settling suspensions of colloidal silica: observations and X-ray measurements. *J. Chem. Soc., Faraday Trans.* **87**, 411-424 (1991).

23. Piazza, R., Bellini, T. & Degiorgio, V. V. Equilibrium sedimentation profiles of screened charged colloids: A test of the hard-sphere equation of state. *Phys Rev Lett* **71**, 4267-4270 (1993).

24. Crocker, J. C. & Grier, D. G. Methods of digital video microscopy for colloidal studies. *Journal of colloid and interface science* **179**, 298-310 (1996).

25. Kim, Y., Shah, A. A. & Solomon, M. J. Spatially and temporally reconfigurable assembly of colloidal crystals. *Nat Commun* **5**, 3676 (2014).

26. Hsiao, L. C., Newman, R. S., Glotzer, S. C. & Solomon, M. J. Role of isostaticity and load-bearing microstructure in the elasticity of yielded colloidal gels. *Proceedings of the National Academy of Sciences* **109**, 16029-16034 (2012).

27. Antl, L. et al. The preparation of poly (methyl methacrylate) latices in non-aqueous media. *Colloids and Surfaces* **17**, 67-78 (1986).

28. Zhang, Z., Pfleiderer, P., Schofield, A. B., Clasen, C. & Vermant, J. Synthesis and directed self-assembly of patterned anisometric polymeric particles. *J Am Chem Soc* **133**, 392-395 (2011).

29. Marlow, B. J. & Rowell, R. L. Acoustic and electrophoretic mobilities of coal dispersions. *Energy & Fuels Energy Fuels* **2**, 125-131 (1988).

30. Reiber, H. et al. Salt concentration and particle density dependence of electrophoretic mobilities of spherical colloids in aqueous suspension. *Journal of Colloid and Interface Science* **309**, 315-322 (2007).

31. Zukoski, I. V., C.F & Saville, D. A. Electrokinetic properties of particles in concentrated suspensions. *Journal of Colloid and Interface Science* **115**, 422-436 (1987).

32. Gilleland, W.T., Torquato, S. & Russel, W.B. New bounds on the sedimentation velocity for hard, charged and adhesive hard-sphere colloids. *Journal of Fluid Mechanics* **667**, 403-425 (2011).

33. Thies-Weesie, D.M.E., Philipse, A.P., Nagele, G., Mandl, B., & Klein, R. Nonanalytical Concentration Dependence of Sedimentation of Charged Silica Spheres in an Organic Solvent: Experiments and Calculations. *Journal of Colloid and Interface Science* **176**, 43-54 (1995).

34. Bard, A. J. & Faulkner, L. R. Electrochemical methods: fundamentals and applications, 2nd. *Hoboken: Wiley and Sons* (2001).

35. Sangani, A. S. & Acrivos, A. Slow flow through a periodic array of spheres. *International Journal of Multiphase Flow* **8**, 343-360 (1982).

36. Russel, W. B., Saville, D. A. & Schowalter, W. R. *Colloidal Dispersions (Cambridge Monographs on Mechanics)* (Cambridge University Press, 1992).

37. Peppin, S. S. L., Elliott, J. A. W. & Worster, M. Solidification of colloidal suspensions. *Journal of Fluid Mechanics* **554**, 147-166 (2006).

38. Yethiraj, A. & van Blaaderen, A. A colloidal model system with an interaction tunable from hard sphere to soft and dipolar. *Nature* **421**, 513-517 (2003).

39. Beltran-Villegas, D. J. & Bevan, M. A. Free energy landscapes for colloidal crystal assembly. *Soft Matter Soft Matter* **7**, 3280-3285 (2011).

40. Brewer, D. D. & Kumar, S. Dynamic simulation of sediment films of Yukawa-stabilized particles. *Physical Review E Phys. Rev. E PRE* **91**, 022304 (2015).

41. Solomon, T. & Solomon, M. J. Stacking fault structure in shear-induced colloidal crystallization. *J Chem Phys* **124**, 134905 (2006).

Chapter 3

Capillary-driven binding of thin triangular prisms at fluid interfaces for self-assembly of open networks

3.1 Abstract

We observe capillary-driven binding between thin, equilateral triangular prisms at a flat air-water interface. The triangles are fabricated from epoxy resin via SU-8 photolithography. The edge length of the equilateral triangle face is 120 μm, and the thickness of the prism is varied between 2 and 20 μm. For thickness to length (T/L) ratios of 1/10 or less, the pairs of triangles preferentially bind in either a tip-to-tip or tip-to-midpoint edge configurations; for pairs of particles of large thickness, the tip of one triangle binds to any position along the other triangle's edge. Optical and environmental scanning electron microscopy (eSEM) demonstrate that the distinct binding configurations for small T/L ratios result from physical bowing of the prisms, which is an inherent property that arises during their fabrication. When bowed prisms are placed at the air-water interface, two distinct polarity states arise: prisms either sit with their center of mass above or below the interface. For both polarity states, the concave face of the bowed prisms faces the interface. The interface pins to the edge of the prism's concave face, resulting in a capillary hexapole. The coupled polarity and hexapole are the source of the

dichotomy in binding configurations: prisms with the same polarity bind tip-to-tip, and prisms with the opposite polarity bind tip-to-midpoint edge. Given sufficient time and rotational mobility, tip-to-tip binding collapses to a side to side configuration with the two edges in registry; tip-to-midpoint edge binding collapses to a side to side configuration in which the two edges are offset. When the T/L ratio grows to 1/5, prism bowing, polarity, and capillary hexapoles are not observed, indicating that prism bowing is the source of both the polarity and the hexapole. Prisms of all T/L ratios self-assemble into space-spanning open networks; the results suggest design parameters for the fabrication of building blocks of ordered open structures such as the Kagome lattice.

3.2 Introduction

Attractive, long-range capillary interactions arise between particles at an air-liquid or liquid-liquid interface because they minimize the free energy generated by the particle-induced curvature of the interface. [1,2,3,4] Self-assembly of colloidal, granular, and millimeter-scale particles has been observed at both air-water and oil-water interfaces due to such capillary-induced pair attractions. At the colloidal scale, short-range electrostatic repulsions also influence self-assembly. [5-7] Recently, spatially anisotropic capillary attractions have been used to produce ordered particle chains and complex open networks at fluid interfaces. For example, colloidal ellipsoids at oil-water and air-water interfaces form such structures. Particle configurations that arise at the interface are dependent on particle surface geometry, chemistry, and wettability. [7,8] For example, cylinders and related anisotropic shapes assemble into chains at an oil-water interface, with the specific particle faces that bind determined by the curvature of the particle face. In these cases, the spatial anisotropy of the capillary interaction is a consequence of

differences in the local curvature of the particle. [9,10] For example, cylindrical particles at an oil-water interface generate a quadrapolar interaction: the interface deforms in one direction at the flat ends of the cylinder and the opposite direction at the curved edges. These deformations yield attractive capillary interactions between faces with like-curvature and repulsions between faces with opposite-curvature. [9,10]

Capillary-driven self-assembly therefore is a path to the bottom-up assembly of open and network structures. Such structures are targets for self-assembly due to interesting and potentially useful properties – primarily mechanical – that arise from the incorporation of voids into material structures. [11] These networks and voids deform non-affinely in ways that can lead to mechanical properties such as enhanced rigidity and negative Poisson's ratio. For example, open networks of colloidal ellipsoids assembled at a fluid-fluid interface exhibited a significantly enhanced low frequency modulus as compared to close-packed networks of colloidal spheres at similar particle concentrations. These colloidal networks can evolve over time, becoming increasing heterogeneous. [7]

Current methods to fabricate open networks include the above described capillary-driven assembly of colloidal ellipsoids [7,8] and polymer-molded microhexagram prisms, [12] self-assembly of patchy colloidal spheres, [13] and top-down approaches on the granular and millimeter-scale such as polymeric 3D-printing, [14] quasi-2D-polymer molding [15] and lithography. [16] Bottom-up self-assembly methods can be advantageous compared to these top-down methods, because of the potential scalability of self-assembly processes. [17,18]

Here we investigate the possibility of using a hexapolar interaction generated between pairs of thin, triangular microprisms to self-assemble space-spanning open networks at low particle concentrations. Assembly of such a rigid, stabilizing network by control of such lateral

interactions could yield complex fluids with useful bulk and interfacial rheology properties of interest in a variety of fields and industries, such as food science, drug delivery, and petroleum processing. [19,20]

Thin prisms – quasi-2D shapes with finite but small thickness – can generate capillary interactions at fluid-fluid interfaces if sufficient interface deformation is induced at the prism edges. The symmetry of thin, triangular prisms is such that bonds at the vertices of these particles might yield ordered structures such as the kagome lattice - an isostatic structure with a unit cell of two inverted triangles. These kagome lattices are known to display non-linear mechanical properties such as a negative Poisson's ratio. [13-15,21,22] To improve the prospects for assembling such complex open structures – either ordered or disordered – the pair-binding behavior of thin homogenous microprisms at interfaces should be investigated. Better understanding of the transient and steady-state binding can identify conditions which ordered and/or disordered networks might occur; each structural family might itself exhibit interesting mechanical properties. [7] Open, planar networks – both disordered and ordered – are therefore attractive targets for interfacial self-assembly.

Here, we observe capillary-driven binding of thin, triangular prisms, with edge lengths ~120 μm and thicknesses between 2.5 and 20 μm at an air-water interface. The pairwise interaction between prisms is measured and connection with modeling efforts are made. The particles are produced by polymeric photolithography; the anisotropic, directional interactions are introduced by the unexpected generation of a capillary hexapole, which arises due to the 2D triangular shape and contact line curvature induced by edgewise bowing of the prisms that is introduced at the time of synthesis. We record the different types of binding events observed between the vertices and flat edges of the interacting prisms. The type of binding event is

predictable from the up/down polarity of particle attachment to the interface, which is well characterized via out-of-plane imaging and environmental scanning electron microscopy. From the particle thickness and bowed radius of curvature, we contribute to the parameterization of a hexapolar pairwise potential. These results inform the design of complex open networks from interfacial building blocks, of which some initial instances are reported.

3.3 Materials & Methods

3.3.1 Particle Fabrication

Particles are fabricated via SU-8 photolithography methods. [9,10,23] First, a sacrificial release layer of Omnicoat (Microchem Corp.) is spun onto a glass wafer (D-263 borosilicate glass, Precision Glass & Optics) and baked at 200 C until cured to a thickness of tens of nanometers (1-2 minutes). After cooling to room temperature, SU-8 2000 series photoresist (Microchem Corp.) is spun on top of the Omnicoat layer to the desired prism thickness and baked at 95 C until cured (~2-5 minutes depending on resist thickness). Next, the wafer is exposed to UV light (365 and 405 nm) through a chrome photomask that encodes the particle pattern (Fineline Imaging) until exposure energies of 60-150 mJ (depending on resist thickness) are achieved. The wafer is then heated at 95 C for 2-5 minutes (depending on resist thickness) to ensure adequate cross-linking of the exposed photoresist.

The wafer is immersed in SU-8 developer solution (Microchem Corp.) until the non-photopolymerized SU-8 is washed away (~1-5 minutes depending on resist thickness), leaving the cross-linked particles immobilized on top of the release layer. The wafer is exposed to oxygen plasma for 20 minutes, which facilitates release of the particles into isopropanol. The

particles are stored in isopropanol, where they remain stable for several weeks. This process yields approximately 10^6 particles per fabrication. Fig. 1 shows the 4 types of equilateral triangular prisms fabricated. All prisms have an edge length of 120 μm, and thickness of: (a) 2.5 μm, (b) 5 μm, (c) 12 μm, and (d) 20 μm. The ratio of the thickness (T) to length (L) of the prisms is a characteristic parameter; we hereafter refer to each type of prism as: (a) T/L = 1/50, (b) T/L = 1/25, (c) T/L = 1/10, and (d) T/L = 1/5.

3.3.2 Placement of particles at the air-water interface

A flat interface is formed between air and deionized water in a chamber (Thermo Scientific Lab-Tek II, 2 Chamber, coverslip 0.13-0.17 μm thick, type 1.5) of dimension 2.0 x 2.0 cm, mounted on to the stage of a Nikon A1Rsi confocal microscope. The chamber's large experimental area and acrylic walls allow for a flat air-water interface to form – without the need for surface modification of the chamber – through careful placement of water in the chamber with a transfer pipette. The walls of the chamber are manually wet prior to filling the center of the chamber with water, in order to prevent uneven attachment of the interface to the walls of the chamber. 10 μL of the particle stock solution is gently placed in one or two drops at the air-water interface using a gas-tight Hamilton 100 μL syringe.

3.3.3 Observation of binding events with optical and reflection microscopy

The interface is imaged with the transmission and 488 nm reflection channels of a Nikon A1Rsi confocal microscope (10x objective, NA = 0.25) in a square region of 1270 x 1270 μm.

Images of pair binding and assembly are acquired at frame rates of 15 frames per second (fps) for prisms of T/L $\geq$ 1/25 and 30 fps for T/L = 1/50. For pair binding experiments, particle positions, relative orientations, and trajectories are tracked using ImageJ software (available at https://fiji.sc/).

3.3.4 Quantifying capillary attraction energies through observation of interface deformation with environmental SEM

Environmental SEM (eSEM, FEI Quanta 3D) is used to observe interface deformation and curvature around the edges of the particles. A gel trapping technique is used to immobilize particles at the interface. [10,24] Briefly, gellan gum, which was generously supplied as a gift from CP Kelco, (low acyl Kelcogel, 2 wt. %) is dissolved in deionized water at 95 °C. The gellan solution remains fluid at temperatures greater than 50 °C. The gellan solution is placed into an eSEM imaging chamber at 70 °C, and prisms are spread at the interface. The imaging chamber is at room temperature, a condition at which the gellan solution crosslinks, immobilizing the prisms for later imaging. Identical prism-prism capillary-driven binding is observed at the gellan solution-air interface as is observed at the pure water-air interface, suggesting that the gellan solution has a negligible effect on the capillary-binding mechanism, consistent with reports of right cylinders at gellan interfaces. [10]

3.4 Results

3.4.1 Capillary-driven binding of triangular prisms at a flat air-water interface

Prisms of all T/L ratios undergo lateral capillary-driven binding at a flat air-water interface. Capillary attractions yield particle-particle binding immediately upon particle attachment at the interface. Over a period of about one hour, the prisms self-assemble into open structures of progressively increasing size (as shown for the case of T/L = 1/25 in Fig. 2).

3.4.2 Polarity in T/L = 1/50, 1/25, and 1/10 prism interface attachment

Fig. 3 shows 1270 x 1270 μm regions of open networks formed by prisms of the four T/L ratios synthesized. Each row in Fig. 3 corresponds to a specific T/L ratio (row 1 shows an open network formed by T/L = 1/50 prisms, row 2 is for T/L = 1/25 prisms, row 3 is T/L = 1/10, and row 4 is T/L = 1/5). The networks span several millimeters in space and are visible to the naked eye. For the three thinnest T/L ratios, the network's steady-state microstructure is comprised of a mix of dense, close-packed regions (with numerous prisms bound edge-to-edge), long strands, and large voids. On the other hand, relative to the thinner prisms, the network self-assembled from T/L = 1/5 prisms contains significantly fewer prisms in close-packing configurations, less chaining, smaller voids, and a generally more homogeneous prism density throughout the image.

In the course of imaging the open networks in Fig. 3, the location of the microscope's focal plane relative to the air-water interface was varied and an interesting feature of the pair binding was observed. Upon varying the focal plane slightly above and below the interface, we observe that T/L = 1/50, 1/25 and 1/10 prisms are pinned to the interface in such a way that their centers-of-mass either sit slightly above or below the interface. The second and third columns of

Fig. 3 show this kind of imaging in the same 1270 x 1270 μm region of the open network as imaged in the first column. In column one, the microscope's focal plane is located at the air-water interface. All prisms appear in-focus, as demonstrated by their sharp, dark edges and tips, as well as their bright bodies. In column two, the microscope's focal plane is located ~200 μm below the air-water interface. For the three thinnest prisms (T/L = 1/50, 1/25 and 1/10), some prisms remain sharply in-focus, with their dark edges and tips appearing thicker and even more visible than in column one and their bodies remaining bright, while all other prisms fall distinctly out-of-focus, with their tips becoming bright and their edges and bodies appearing darker and faded.

In column three, the microscope's focal plane is located ~ 200 μm above the air-water interface, in the opposite direction of the column two images. For the three thinnest prisms (T/L = 1/50, 1/25 and 1/10), the prisms that were in-focus in column two now appear out-of-focus, while the particles that appeared out-of-focus in column two now appear in-focus. (Additionally, a very small fraction of T/L = 1/50 prisms do not exhibit in-focus vs. out-of-focus polarity; they appear equally in-focus on both edges of the interface.)

Although the three thinnest prism populations are located above and below the interface, the thickest prisms (T/L = 1/5) do not exhibit such in-focus vs. out-of-focus polarity; these prisms all appear equally in-focus relative to one another in both columns two and three. The relative image quality for the T/L = 1/5 prisms appears better below the interface (column two) than above (column three), suggesting that all these prisms are situated slightly below the interface.

To further investigate the precise manner of prism interface attachment, we observe the prisms using eSEM (Fig. 6). Figure 6 confirms polarity in interface attachment for T/L = 1/50, 1/25, 1/10 but not for the thickest (T/L = 1/5) prism, exactly consistent with the results from changing the optical microscopy focal plane. eSEM images of T/L = 1/50 prisms are shown in Fig. 6a and b. Fig. 6a shows a prism whose center of mass lies below the gelled interface in the water phase, and Fig. 6b shows a prism whose center-of-mass lies above the gelled interface in the air phase. In addition, significant particle bowing along each of the three prism edges is observed. Referring back to Fig 1, this bowing is already apparent in the SEM images of the as fabricated particles. Apparently, this bowing is a permanent, reproducible feature of the thin prisms, and persists from the synthesis stage through to the assembly experiments. As discussed later, this bowing is critical to the pair binding mechanism.

Interface attachment of the T/L = 1/25 prisms are shown in Fig. 6c. The top face of a prism in the middle of the image is covered by the gelled interface (as evidenced by the rippling texture on top of this prism, which is consistent with the surface of the gelled water phase elsewhere in the image), while several other prisms in the image sit with their top faces uncovered by the interface (as evidenced by the smooth texture of the exposed faces of these particles, relative to the rippling surface of the gelled water phase).

The T/L = 1/25 prisms do not appear significantly bowed relative to the T/L = 1/50 prisms. Still, the curvature of the interface results in a polarity in prism-interface attachment: the covered prisms' centers of mass sit below the interface (in the gelled water phase), and the uncovered prisms' centers of mass sit above the interface (in the air phase). Polarity is again observed for T/L = 1/10 prisms, shown in Fig. 6d. Several prisms rest with their centers of mass below the interface, and the top face of the prism is covered by the surface of the gelled

interface, while other prisms sit substantially higher on the interface, with their top faces exposed to the air phase. T/L = 1/10 and 1/25 prisms appear very similar at the interface; they exhibit attachment polarity, yet significant bowing is not observable.

Polarity of the particle position relative to the interface is not at all visible for T/L = 1/5 prisms. Fig. 6e is representative of all observed T/L = 1/5 prisms; the interface is observed to rise at the corners of the prisms, and prisms all appear to sit at the same interface position, relative to both the interface and to one another.

In the ensuing discussion we define the polarity of the thin prisms as positive or negative. A prism with positive polarity refers to a prism whose center of mass sits above the interface in the assembly experiments, while a prism with negative polarity refers to a prism whose center of mass sits below the interface.

Interface attachment polarity is quantified - and its effect on open network structure examined - in Figs. 4 (T/L = 1/50) and 5 (T/L = 1/25). Each row of Fig. 4 and 5 shows one 1270 x 1270 μm region of an open network. In the first column, the focal-plane is located ~200 μm below the interface (as in the second column in Fig. 3). In the second column, the focal-plane is located ~200 μm above the interface (as in the third column in Fig. 3). In these first two columns, each prism is assigned a polarity, determined by the side of the interface for which they are observed to be in-focus. (For T/L = 1/50, 20% of prisms cannot be resolved as above or below the interface; these particles are therefore not assigned a polarity.) For T/L = 1/25, all prisms can be, and are, assigned a polarity.)

In the third and fourth column, the focal-plane is located at the interface (as in the second column of Fig. 3). In the third column, bonds between prisms with (a) the same polarity

(identified with red and blue connecting lines for bonds between pair-bonded prisms of negative and positive polarity, respectively) (b) the opposite polarity (purple connecting lines), and (c) indeterminate polarity (black connecting lines) are identified. The number of such bonds are counted in Tables 1 (Fig. 5) and 2 (Fig. 6).

In the fourth column, prism-prism bonds are identified by the relative orientation of the two particles, independent of the polarity state of each particle. Four types of bonds are observed: (a) tip-tip (green connecting lines), (b) tip-edge (pink connecting lines), (c) edge-edge (orange connecting lines; edges of triangles are in registry – in contact and flush with one another), and (d) edge-edge offset (brown connecting lines; half of the edge of each bonded triangles lie flush with one another, with the tip of one triangle located at the center of the other triangle's edge). These bonded states are also tabulated in Tables 1 (Fig. 5) and 2 (Fig. 6).

Each bond identified in Figs. 5 and 6 is sorted into Table 1's and 2's rows based on the polarity of the bounded prisms, and into Table 1's and 2's columns based on the observed pair bonded state. In Tables 1 and 2, 237 bonds are analyzed across six 1270 x 1270 μm regions of open networks of T/L = 1/25 and 1/50 prisms (three 1270 x 1270 μm regions per network). 17 bonds are between prisms with indeterminate polarity, and are not included in this analysis. Of the 220 remaining bonds, there is perfect agreement in the number of bonds between prisms with the same polarity (133 bonds) and prisms bound tip-tip or edge-edge (133 bonds), and there is also perfect agreement in the number of bonds between prisms with the opposite polarity (87 bonds) and prisms bound tip-edge or edge-edge offset (87 bonds).

Averaging over three locations in each network, and counting for 237 bonds total, bonds between prisms with the same polarity account for 48% of all bonds for T/L = 1/50 prisms and

64% of all bonds for T/L = 1/25 prisms, bonds between prisms with the opposite polarity account for 37% of all bonds for T/L = 1/50 prisms and 36% of all bonds for T/L = 1/25 prisms, and bonds between prisms with indeterminate polarity account for 15% of all bonds for T/L = 1/50 prisms and are not observed for T/L = 1/25 prisms. To assess if thin, polar prisms spread at an air-water interface are biased towards bonds between prisms of the same polarity, we ignore bonds between prisms of indeterminate polarity (which only arise for a small minority of the very thinnest of thin prisms), and assume a normal distribution of bonds between prisms of the same and opposite polarity – consistent with a null hypothesis that the system is not biased towards bonds between prisms of the same polarity. 220 bonds between prisms of either the same (133) and opposite (87) polarity are counted in Figs. 5 and 6, and the probably of such a distribution in an unbiased system is less than 0.2%.

3.4.3 Effect of thin prism (T/L $\leq$ 1/10) bowing on interface attachment

SEM and eSEM images (Figs. 1a and 4a and b) clearly show that T/L = 1/50 prisms are bowed. SEM images of T/L = 1/25 prisms (Fig. 1b) also show subtle bowing; however, this bowing is not obvious in the analogous eSEM images of T/L = 1/25 prisms at the air-gelled water interface (Fig. 4c). Optical micrographs also show evidence for bowing in T/L =1/50 (Fig. 6) and 1/25 (Fig. 5) prisms. That is, prisms of assigned polarity appear to have bright, central bodies and dark tips when in focus, and dark central bodies and bright tips when out of focus. This illumination contrast appears consistent with a difference in the position of the prism central body and tips relative to the microscope's focal plane; the bowing apparent in the electron microscopy is also consistent with these images. The few prisms with indeterminate polarity (e.g. T/L = 1/50, Fig. 6) do not exhibit such a contrast in illumination of tips vs. edges. The

contrast in illumination is also apparent in optical micrographs of T/L = 1/10 prisms (Fig. 3c); however, bowing is not obvious in either SEM (Fig. 1c) or eSEM images of these prisms at the air-gelled water interface (Fig 4d).

Inhomogeneity in prism surface wetting – which can be introduced during prism fabrication as described in the methods – is not the source of prism polarity. Thin prisms (T/L $\leq$ 1/10) fabricated with and without plasma treatment on one side both exhibit the two polarity states. The contact angle difference in the plasma treated particles is ~70˚ immediately following treatment. This insensitivity to plasma treatment suggests that the prism bowing is the primary driver of the observed polarity. .

The bowing specifies the curvature of the interface around the prism. This interfacial curvature in turn determines the capillary-driven attraction between the prisms. Figs. 4a and b show that prisms with positive polarity (on top of the interface) are bowed downwards (with tips pointing towards the water phase), and negative polarity (below the interface) prisms are bowed upwards (with tips pointing towards the air phase). In both cases, the interface appears pinned to the corner of the prism's edge and to the concave face. Thus, the curvature of the interface follows the curvature of the bowed prism. The result is that the interface curvature at the tips and edges of triangle is opposite for prisms of positive and negative polarity.

Fig. 7a shows a rendering of this interface pinning mechanism for a bowed T/L = 1/50 prism with negative polarity, which is created using Surface Evolver, a numerical simulation program which may be used to analyze capillary surfaces, as provided courtesy of my collaborator, Deshpreet Bedi. [25] The degree of the prism's bowing is imposed based on observations from eSEM, and the magnitude and range of interface curvature may be quantified. Prism bowing results in a capillary hexapole; the pinned interface rises at the tips of the triangles

and falls at the flat edges. The hexapole is quantified by a capillary potential landscape, which is computed from the magnitude and direction of interface curvature as function of distance from the prism's edge, as plotted in Fig. 7b. Overlapping landscapes for pairbinding prisms of the same, negative polarity are shown in Fig. 7c, which quantifies the capillary pair potential at a complete set of interface locations surrounding each prism. The capillary pair potential is plotted as a function of the prism's angular orientation and interprism separation distance in Fig. 7d.

3.4.4 Measurement and modeling of pairwise capillary potentials

As discussed in the literature [9,10,23], the strength of the pair particle capillary interactions vary as a function of the inter-prism separation and the relative orientation of the prisms. These pair interactions are predicted with Surface Evolver simulations of the capillary profile in the vicinity of two interacting prisms (Fig. 7c), and plotted as a function of the inter-prism separation and the relative orientation of the prisms (Fig. 7d). Time-evolved measurement of the inter-prism separation and angle of orientation as they undergo pairwise binding can be applied to characterize the pair potential interaction and verify the simulation predictions of Fig. 7. Pairwise capillary interactions are measured by observing the kinetics of prism-prism binding at dilute prism concentrations for both T/L = 1/50 and 1/25 (Fig. 8) prisms.

Fig. 8a and b show time series of the trajectories of T/L = 1/50 prisms which approach and bind due to capillary interactions. Fig. 8c and d show the analogous time series of two pair binding trajectories for T/L = 1/25 prisms. In each case, the centroidal separation and relative orientation are plotted (Fig 9). For both T/L ratios, two different kinds of binding trajectories are observed, depending on if the polarity of the prisms are the same or opposite. For the same

polarity, a trajectory leading to tip-to-tip binding is observed (8a and c); opposite polarity results in tip-to-midpoint edge binding (8b and d).

The Figure 8 binding trajectories shown are representative of all binding events observed. In the tip-to-tip trajectory, the prisms approach and first contact occurs at the tips. The prisms then rotate into a collapsed, fully flush edge-to-edge orientation (as seen in the final frame of Fig. 8a and c).

In the tip-to-midpoint edge trajectory, the prisms approach and contact one another in an orientation such that the tip of one prism binds at the midpoint of the other prism's edge. The prisms then rotate into an edge-to-edge orientation in which the two edges are offset from each other by L/2 (as apparent in the final frame of Fig. 8b and d).

The significant bowing of the T/L = 1/50 prisms allows characterization of the prism polarity even though the microscope's focal plane is located at the interface in Fig. 8a and b. The tip-tip event (with transition to edge-to-edge) occurs between particles with like polarity, while the tip-midpoint edge event (with transition to offset edge-to-edge) occurs between particles with opposite polarity.

The measured interprism separation for each of the four events shown in Fig. 8 is plotted in Fig. 9a. The interprism separation is defined as the distance between each centroid of the binding prisms; this separation is measured by image analysis for several seconds before the prisms contact one another. Fig. 9a shows that the time scale of prism-prism binding is significantly faster for T/L = 1/50 prisms as compared to T/L = 1/25 prisms.

This difference indicates that capillary attractions are much stronger at separation distances of up to several prism edge lengths for T/L = 1/50 prisms as compared to T/L = 1/25

prisms. By contrast, there is negligible difference in the time scale of tip-tip and tip-edge binding at fixed T/L ratio, an indication that the strength of both types of interactions are similar. The measured relative angular orientation of each of the prisms shown in Fig. 8 is plotted in Fig. 9b (T/L = 1/50) and 9c (T/L = 1/25). As illustrated in the binding event time series shown in Fig. 9d, a prism's angular orientation at time t is defined as the angle between the binding edge of the prism (the edge which lies flush against the corresponding bound prism following collapse) in its final collapsed state, and the position of this binding edge at that time. Prism angular orientation remains largely unchanged during prism-prism approach up until binding for all cases except the tip-tip trajectory for T/L = 1/50 (Fig. 9b). Tip-tip to edge-edge and tip-edge to edge-edge offset collapse occurs nearly instantaneously upon binding for T/L = 1/50 prisms, while collapse requires ~ 1 second for T/L = 1/25 prisms.

3.4.5 Assembly into open networks

As described in the introduction, thin prisms are potential building blocks for 2D open structures with enhanced mechanical properties. The pair-binding observations to this point indicate that self-assembly of thin, triangular prisms may result in 2D networks with both open (tip-tip and tip-edge pair-binding orientations) and close-packed (edge-edge and edge-edge offset pair-binding orientations) conformation. Thus, assessment of the self-assembled networks' structure, (specifically, assessment of network porosity) are needed to determine whether or not capillary binding of thin, triangular prisms yields macroscopic mechanical utility.

Recall time-evolved pair-binding of prisms into larger aggregates (Fig. 2). At early times (Fig. 2b and c), the aggregates consist of regions with close-packed prisms, which bond with

their edges flush to one another, and more open, porous regions, formed by bonds between particle tips. These small aggregates undergo time-dependent growth via aggregate-aggregate attraction and binding (Fig. 2d and e). These larger aggregates branch laterally in all directions, which yields further porosity within the aggregate structure. Aggregates continue to attract and bind to one another until steady-state structure is achieved, and all prisms are incorporated into a space-spanning, open network, as shown for all T/L ratios in Fig. 10. Each of the four images in Fig. 10 is a cropped, 3.8 x 2.5 mm spatial mosaic of either six or eight (either three-by-two or four-by-two) 1270 x 1270 μm^2 microscopy images. While the all self-assembled networks possess voids, the three thinnest prisms (T/L = 1/50, 1/25 and 1/10, which exhibit polarity), contain linear chains of triangles bound in close-packed edge-edge states (Fig. 10a – c). By contrast, the thickest prisms (T/L = 1/5, which do not exhibit polarity) contain fewer close-packed prisms, and no linear chains of edge-edge bonds (Fig. 10d). Thus, the networks self-assembled from the thinnest, polar prisms are significantly more phase separated, while the network self-assembled from the thickest, apolar prisms is more homogeneous in prism spatial-density.

3.5 Discussion

In the discussion that follows, we comment on the ramifications of the coupled prism polarity and hexapolar interactions of the thinnest prisms; specifically, that polarity of pair-binding prisms is predicative of both pair binding trajectory and of the final pair-bonded state. We then discuss the effect of prism polarity on open network structure and suggest a path to design a prism building block for an ordered kagome lattice.

3.5.1 Prism polarity is predictive of tip-tip vs. tip-edge binding trajectory

Figs. 5 and 6 show that for thin prisms (T/L = 1/25 and 1/50), the kind of prism-prism bond formed (Figs. 5 and 6, column four) may be predicted with 100% fidelity from the polarity of the two prisms participating in the bonding event (Figs. 5 and 6, column three). Bonds between prisms with the same polarity (positive-positive or negative-negative) always result in tip-tip or edge-edge bond orientations. Likewise, bonds between particles with the opposite polarity (positive-negative) always result in tip-to-midpoint edge or edge-edge offset bonding states. In addition to displaying this correlation pictorially in Figs. 5 and 6, this complete correlation is also demonstrated statistically in Tables 1 and 2. Across all regions imaged, there is no occurrence of a bond between prisms of the same polarity resulting in a tip-edge of edge-edge offset bond; likewise there is never an occurrence of a bond between prisms of the opposite polarity resulting in a tip-tip or edge-edge bond.

Inspection of pairwise binding trajectories of T/L = 1/50 and 1/25 prisms (Fig. 8) confirms that the polarity states of binding prisms determine the eventual bonded state. The high degree of bowing of T/L = 1/50 prisms allows a prism polarity state to be assigned even when the focal plane is located at the air-water interface: both prisms undergoing the tip-to-tip binding trajectory in Fig. 8a are of the same polarity, while the prisms in Fig. 8b undergoing the tip-to-midpoint edge binding trajectory are of opposite polarity.

Thus, prisms of the same polarity only access the tip-to-tip trajectory, meaning they only access the tip-tip and edge-edge binding states, while prisms of opposite polarity only access the tip-to-midpoint edge trajectory, meaning they only access the tip-to-midpoint edge and edge-

edge offset binding states. Our observations suggest that the tip-tip and tip-edge binding states only survive at steady-state when the collapse of the prisms into their edge-edge or edge-edge offset states is frustrated, due, for example, to jamming at high prism concentrations. Prism polarity – and its control over prism-prism binding trajectory – is also observed for T/L = 1/10 prisms, although evidence of the effect is not as obvious with optical microscopy (Fig. 3c, columns 2 and 3) and thus was not analyzed in the same way thinner prisms are in Figs. 5 and 6. The T/L = 1/5 prisms, on the other hand, lack polarity, and the predictable binding states observed for the thinner prisms are not observed here. Fig. 3d shows tip-tip and tip-edge bonds, although there is nothing predictable about the bond orientations or binding pathways. Furthermore, tip-edge binding is no longer offset by L/2, but rather, prism tips seemingly bind to random positions along the edge of other prisms. We conclude that for thick prisms a tip of one prism can bind to any point on the other's prisms edge with uniform probability.

3.5.2 Hexapolar interactions arise from interface-prism contact line bowing

Recall that the attachment of the interface to the T/L = 1/50 prism surface (experimentally observed in Fig. 4a and b, rendered in Surface Evolver in Fig. 7a) follows the curvature of the bowed prism, Therefore, for a prism with negative polarity (as rendered in Fig. 7a), the interfaces rises to the triangles tips and falls to the triangle's bowed edges. Conversely, for a prism with positive polarity, the interface must fall to the triangle's tips and rise to the triangle's bowed sides. tips and edges of triangle. Because capillary attractions occur when interface deformation is minimized, an approach vector between the tips of prisms of the same polarity – or a tip and edge of prisms of the opposite polarity –results in a minimization of interface curvature and capillary-drive tip-to-tip binding. In contrast, an approach vector

between a tip and an edge of prisms of the same polarity – or the tips of prisms with the opposite polarity – would result in an increase of interface curvature, thereby generating a repulsive capillary interaction.

Thus, consistent with the bond analysis in Figs. 5 and 6 and observation of pairwise binding events in Fig. 8, the principle of minimizing interface deformation prefers the tip-to-tip trajectory for prisms of the same polarity, and the tip-to-midpoint edge trajectory for prisms of the opposite polarity. Thin, triangular prisms therefore give rise to a capillary hexapole: the prism's three tips and three edges generate interfacial curvature of opposite sign, resulting in six distinct extrema of interface. These extrema are nodes of maximum capillary-induced attraction or repulsion.

Recall that although prism bowing is not directly observed for T/L = 1/25 prisms at the air-water interface, we suspect that a subtle amount bowing is present at this T/L ratio, due to observed bowing in SEM images of T/L = 1/25 prisms at the time of prism fabrication (Fig. 1b) and the correlation between prism polarity over bond (Fig. 5, Table 1). Smaller amounts of bowing would yield weaker capillary-driven attractions, as seen by comparing the kinetics of binding trajectories of T/L = 1/50 and 1/25 prisms in Figs. 9b-d.

As prism T/L ratio increases, so too does the prism stiffness, thereby making the introduction of bowing during the synthetic process less likely. At T/L = 1/10 evidence of prism bowing and polarity becomes limited. Once T/L reaches 1/5, prisms lack polarity, and all evidence of the hexapolar interaction is lost. This suggests that not only does prism bowing drive the formation of a capillary hexapole, but that prism bowing is the source of prism polarity and the source of the two distinct thin prism binding pathways.

3.5.3 Open network structure and the path to capillary-drive self-assembly of ordered open lattices

The open networks shown in Fig. 10 possess voids of irregular and nonrepeating size and shape. These structures are similar to open networks self-assembled from colloidal ellipsoids at fluid-fluid interfaces[7], which demonstrate enhanced rigidity as compared to close-packed arrays of isotropic spheres. Open structures whose voids are more regular in size and shape could possess interesting mechanical properties; such structures have to date largely eluded efforts to produced them by self-assembly; in the case of the equilateral triangular prisms studied here, the target open network would be the kagome lattice.

The kagome lattice unit cell is constructed from triangles bound tip-tip at a fixed angle. Therefore, the tip-tip repulsions and tip-edge attractions that arise from bonding of particles of opposite polarity would need to be suppressed if thin triangular prisms are to self-assemble into such a lattice, as would the rotation of bonding prisms of the same polarity into the edge-edge binding state. [11] Therefore, eliminating one of the two polarity states from the system would be an interesting direction for future work. Our results show that triangular prisms with $T/L \geq 1/5$ achieve this, though a method to eliminate tip-edge attractions and tip-tip to edge-edge collapse must be developed, perhaps through some combination of surface modification or control of curvature in the z-plane. [9,10,12] Alternatively, bowed prisms could uniformly exhibit tip-to-tip by imparting a uniform polarity state to all bowed prisms, perhaps by inducing uniform bowing at the interface with an applied field, and blunting of the prism tips may result in making the initial tip-tip bond permanent, without rotation into an edge-edge binding state.

3.6 Conclusion

We report capillary-driven binding of thin, triangular prisms of T/L between 1/50 and 1/5 into open networks at a flat air-water interface. The interface pins to either the top or bottom face of the three thinnest prisms (T/L = 1/50, 1/25, and 1/10). Interface pinning and physical bowing of the thin prisms results in (a) a capillary hexapole surrounding the prism, and (b) prisms sitting with their centers of mass above or below the interface in even proportion. Thin prisms whose centers of mass reside on the same side of the interface undergo capillary-driven binding via a tip-to-tip trajectory, and prisms whose centers of mass reside on the opposite side of the interface undergo a tip-to-midpoint edge trajectory. Thick prisms (T/L = 1/5) do not exhibit physical bowing and all do not exhibit any difference with regards to the relative position of their centers of mass to the air-water interface. Prisms of all thicknesses self-assemble into open networks with nonrepeating void structure that is indicative of enhanced mechanical rigidity. Networks self-assembled from the three thinnest, polar prisms contain close-packed, linear chains, which results in phase separation between particles and interface. Networks self-assembled from the thickest, apolar prisms contain fewer close-packed prisms and an absence of linear close-packed chains, and a more homogeneous prism density across the network structure. The results inform the design of thin prism building blocks for the design of ordered open networks at fluid-fluid interfaces.

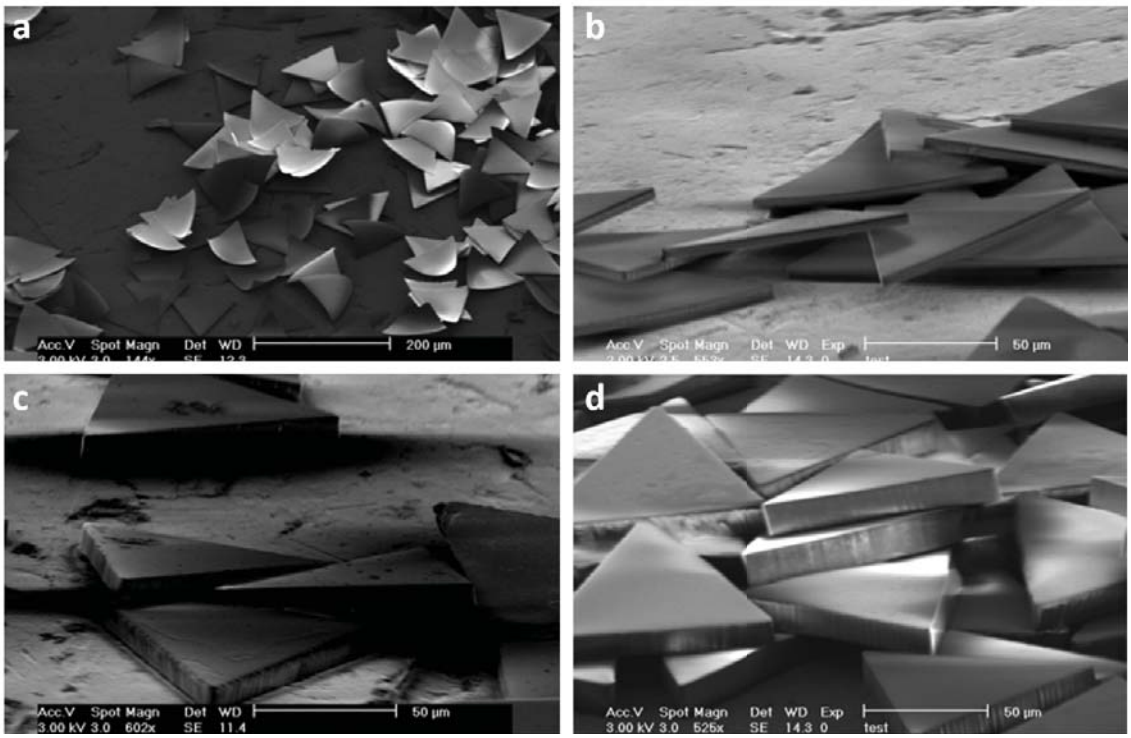

Figure 3-1. SEM images of thin, equilateral triangular microprisms from SU-8 epoxy resin. Equilateral triangle (edge length, L =120 μm) prisms of varying thickness (T) a) T ~ 2.5 μm, T/L = 1/50, b) T ~ 5 μm, T/L = 1/25, c) T ~ 12 μm, T/L = 1/10, d) T ~ 20 μm, T/L = 1/5

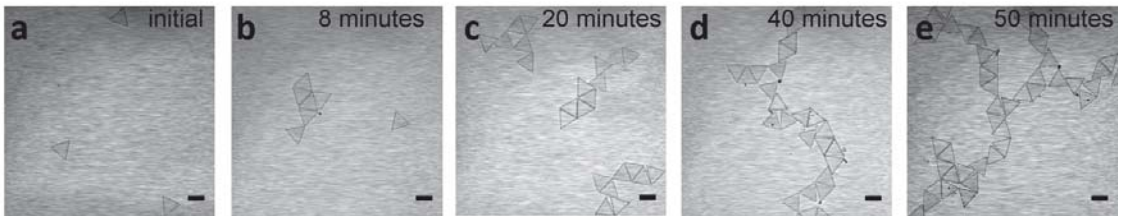

Figure 3-2. Optical microscopy time-series images of capillary-driven triangular prism (T/L ~ 1/25) binding at a flat air-water interface. a) Initial placement of prisms at interface b) 8 minutes after placement of prisms at interface c) 20 minutes d) 40 minutes e) 50 minutes. Scale bars are 100 μm.

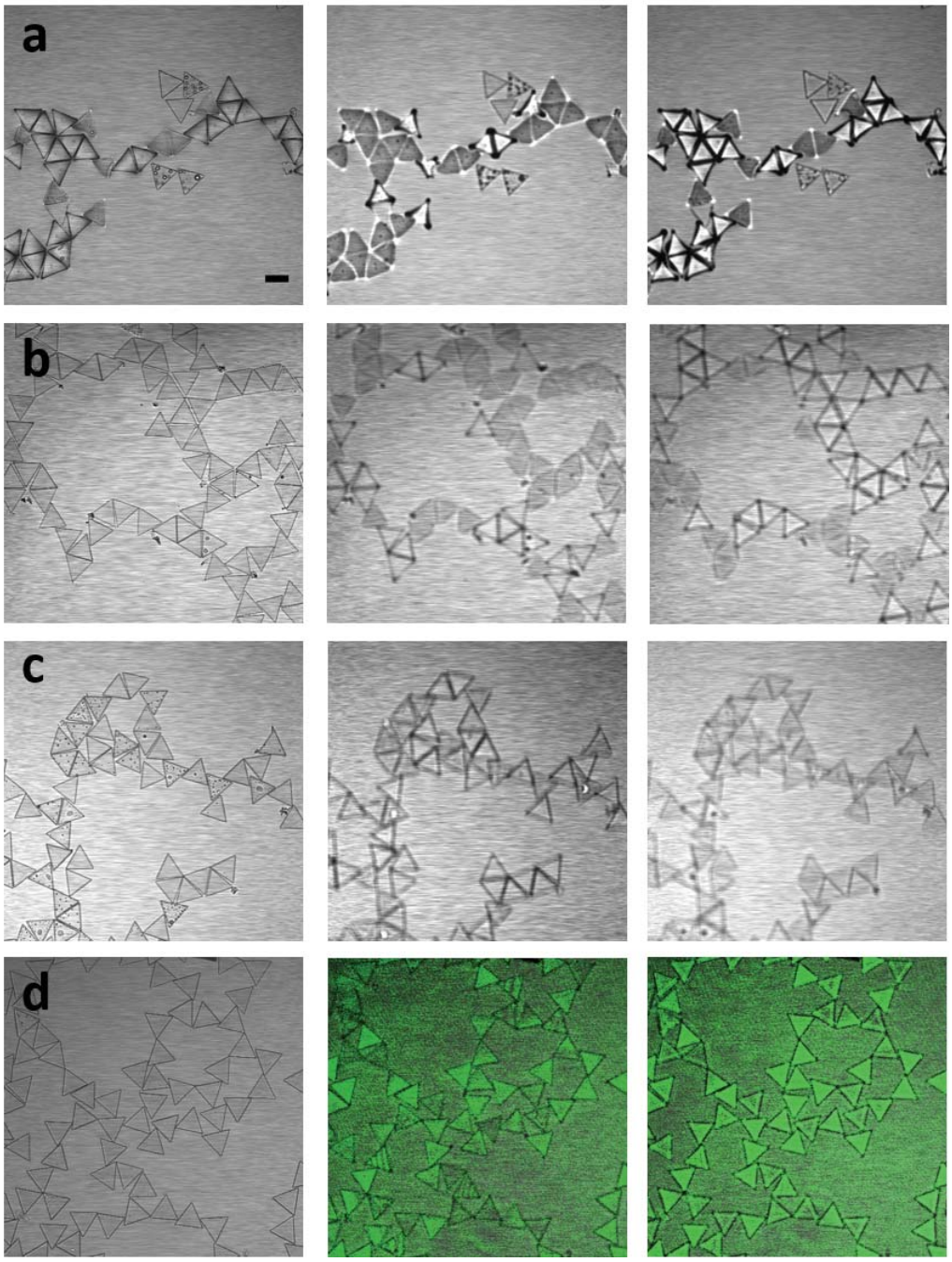

Figure 3-3. Optical and reflection microscopy images of 1270 x 1270 μm^2 regions of open networks. Networks are self-assembled via capillary-driven triangular prism binding. Row 1 (a) T/L ~ 1/50, row 2 (b) T/L ~ 1/25, row 3 (c) T/L ~ 1/10, row 4 (d) T/L ~ 1/5. Column 1: single frame image of portion of network (1270 x 1270 μm), focal plane at air-water interface. Column 2: same single frame image of portion of network as in column 1, focal plane ~200 μm below air-water interface. Column 3: same single frame image of portion of network as in columns 1 and 2, focal plane ~200 μm above air-water interface. Scale bars are 100 μm.

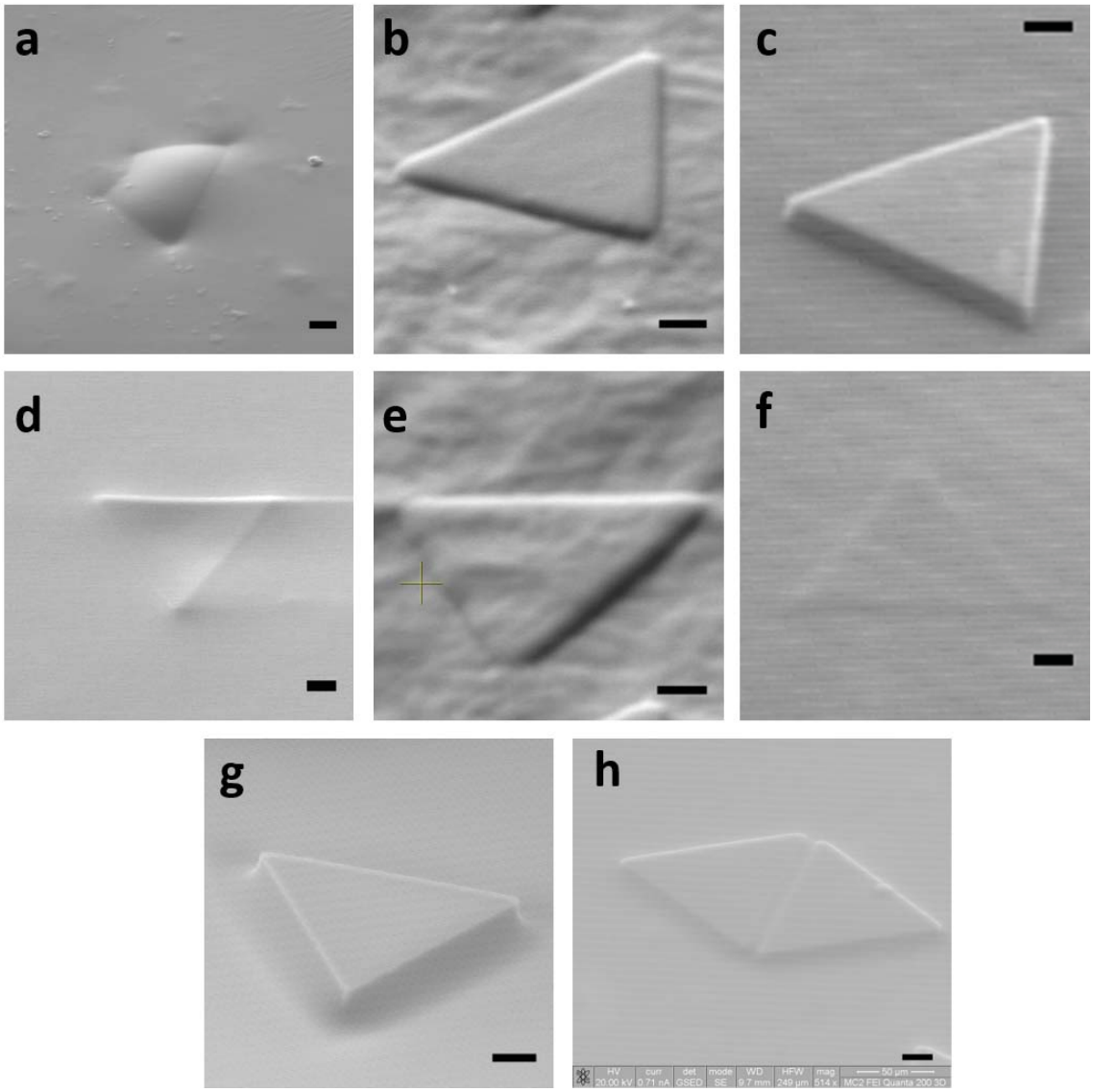

Figure 3-4. Environmental SEM images of triangular prisms, fixed at an air-gellan/water interface. Row 1: (a) - (c) prisms assigned positive polarity: (a) T/L = 1/50, (b) T/L = 1/25, (c) T/L = 1/10. Row 2: (d) - (f) prisms assigned negative polarity: (d) T/L = 1/50, (e) T/L = 1/25, (f) T/L = 1/10. (g) apolar T/L = 1/5 prism. (h) The same capillary-driven binding states are observed at air-gellan/water interface prior to prism immobilization as are observed with optical microscopy at non-gelled interfaces. Scale bars are 20 μm.

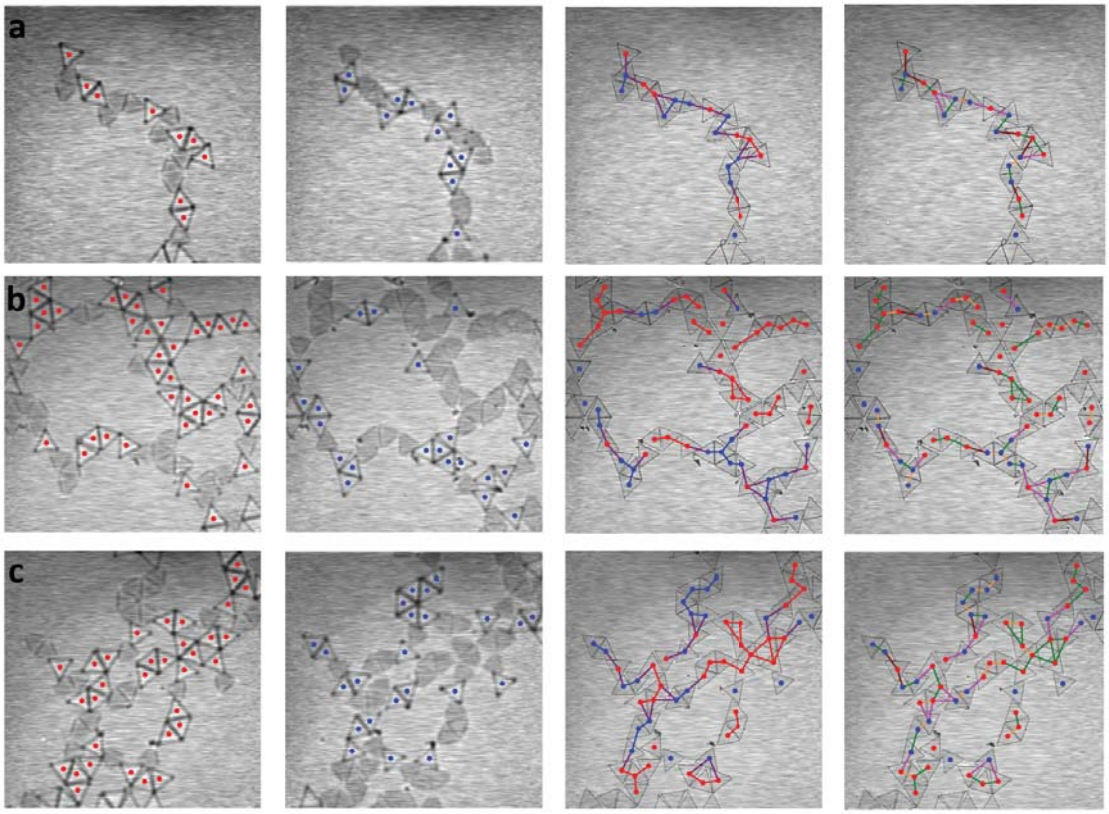

Figure 3-5. Identification of triangular prism binding states (T/L = 1/25). Each row of images (a) – (c) represents a different location within a network structure. The relative position of microscope's focal plane to the air-water interface is varied by column as follows: Column (1): Microscope focal plane is ~200 μm below the interface. In-focus prisms are identified with red markers. Column (2): Microscope focal plane is ~200 μm above the interface. In-focus prisms are identified with blue markers. Column (3): Microscope focal plane is at the interface. Bonds between prisms with the same polarity are identified with blue and red connecting lines, bonds between prisms with the opposite polarity are identified with purple connecting lines. Column (4): Microscope focal plane is at the interface. Prism-prism bonds are identified by their polarity-independent orientation: side-side (orange connecting lines), tip-tip (green connecting lines), side-side offset (brown connecting lines), tip-side (pink connecting lines). Bonds in Columns (3) and (4) are tabulated in Table (1). Scale-bar is 100 μm.

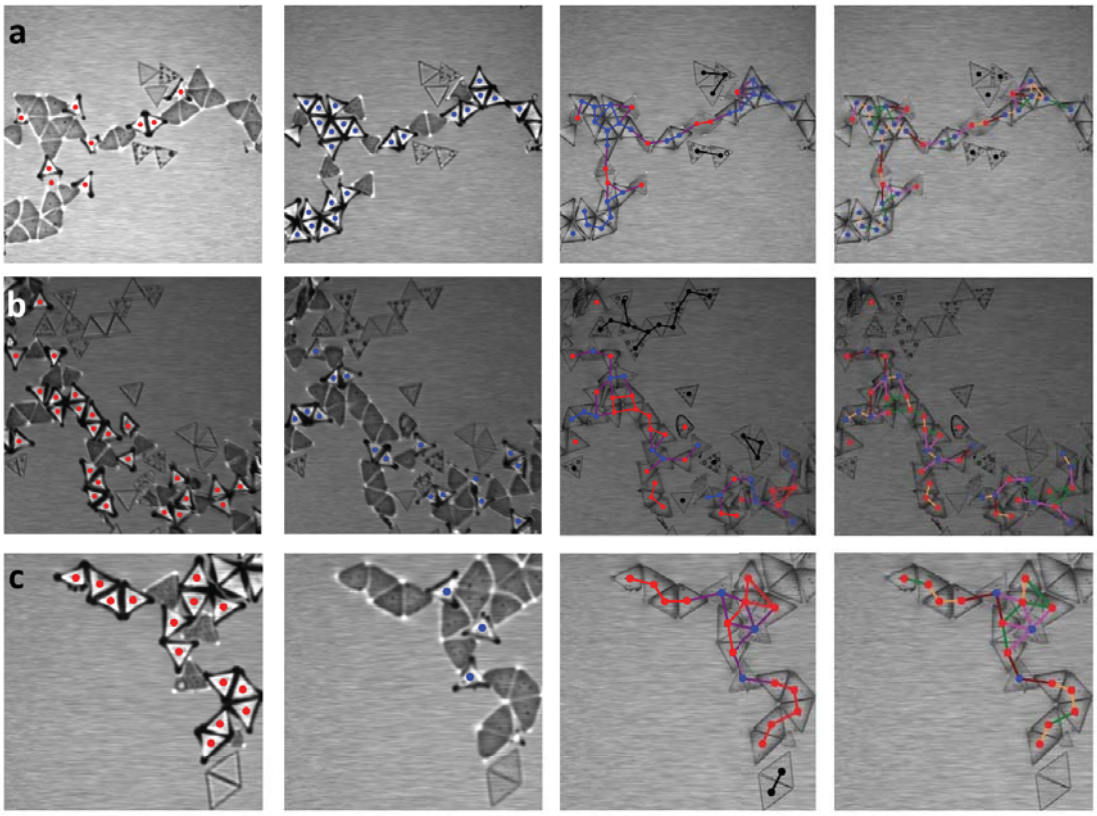

Figure 3-6. Identification of triangular prism binding states (T/L = 1/50). Each row of images (a) – (c) represents a different location within a network structure. The relative position of microscope's focal plane to the air-water interface is varied by column as follows: Column (1): Microscope focal plane is ~200 μm below the interface. In-focus prisms are identified with red markers. Column (2): Microscope focal plane is ~200 μm above the interface. In-focus prisms are identified with blue markers. Column (3): Microscope focal plane is at the interface. Bonds between prisms with the same polarity are identified with blue and red connecting lines, bonds between prisms with the opposite polarity are identified with purple connecting lines, bonds between prisms with indeterminate polarity are identified with black connecting lines. Column (4): Microscope focal plane is at the interface. Prism-prism bonds are identified by their polarity-independent orientation: side-side (orange connecting lines), tip-tip (green connecting lines), side-side offset (brown connecting lines), tip-side (pink connecting lines). Bonds in Columns (3) and (4) are tabulated in Table (2). Scale-bar is 100 μm.

Fig. No.	Relative polarity of bound prisms	No. of Bonds	% of each type of bond	tip-tip	edge-edge	No. of tip-tip + edge-edge	Correlation between relative polarity of bound prisms and bond orientation	tip-edge	edge-edge offset	No. of tip-edge + edge-edge offset	Correlation between relative polarity of bound prisms and bond orientation
5a	Same	10	50%	8	2	10	100%	0	0	0	0%
	Opposite	10	50%	0	0	0	0%	5	5	10	100%
	Indeterminate	0	0%	-	-	-	-	-	-	-	-
	Total	20									
5b	Same	32	66%	19	13	32	100%	0	0	0	0%
	Opposite	16	34%	0	0	0	0%	10	6	16	100%
	Indeterminate	0	0%	-	-	-	-	-	-	-	-
	Total	48									
5c	Same	36	67%	24	12	36	100%	0	0	0	0%
	Opposite	18	33%	0	0	0	0%	15	3	18	100%
	Indeterminate	0	0%	-	-	-	-	-	-	-	-
	Total	54									
Fig. 5 Total	Same	78	64%	51	27	78	100%	0	0	0	0%
	Opposite	44	36%	0	0	0	0%	30	14	44	100%
	Indeterminate	0	0%								
	Total	122									

Table 3-1. Comparison of prism-prism bond type based on polarity of bound prisms and polarity-independent prism orientation for T/L = 1/25. All data is tabulated from analysis described in Fig. 5. Bonds are sorted into rows by the relative polarity of the bound prisms (same, opposite, or indeterminate polarity and into columns by the polarity-independent orientation of the bound prisms. The correlation between the relative polarity of the bound prisms and the polarity-independent bond orientation is calculated for network location analyzed. All bond types and correlations are also totaled over all 3 network locations.

Fig. No.	Relative polarity of bound prisms	No. of Bonds	% of each type of bond	tip-tip	edge-edge	No. of tip-tip + edge-edge	Correlation between relative polarity of bound prisms and bond orientation	tip-edge	edge-edge offset	No. of tip-edge + edge-edge offset	Correlation between relative polarity of bound prisms and bond orientation
6a	Same	23	58%	10	13	23	100%	0	0	0	0%
	Opposite	14	35%	0	0	0	0%	8	6	14	100%
	Indeterminate	3	8%	-	-	-	-	-	-	-	-
	Total	40									
6b	Same	20	41%	9	11	20	100%	0	0	0	0%
	Opposite	20	41%	0	0	0	0%	14	6	20	100%
	Indeterminate	13	27%	-	-	-	-	-	-	-	-
	Total	53									
6c	Same	12	48%	6	6	12	100%	0	0	0	0%
	Opposite	9	48%	0	0	0	0%	5	4	9	100%
	Indeterminate	1	5%	-	-	-	-	-	-	-	-
	Total	22									
Fig. 6 total	Same	55	48%	25	30	55	100%	0	0	0	0%
	Opposite	43	37%	0	0	0	0%	27	16	43	100%
	Indeterminate	17	15%								
	Total	115									

Table 3-2. Comparison of prism-prism bond type based on polarity of bound prisms and polarity-independent prism orientation for T/L = 1/50. All data is tabulated from analysis described in Fig. 6. Bonds are sorted into rows by the relative polarity of the bound prisms (same, opposite, or indeterminate polarity and into columns by the polarity-independent orientation of the bound prisms. The correlation between the relative polarity of the bound prisms and the polarity-independent bond orientation is calculated for network location analyzed. All bond types and correlations are also totaled over all 3 network locations.

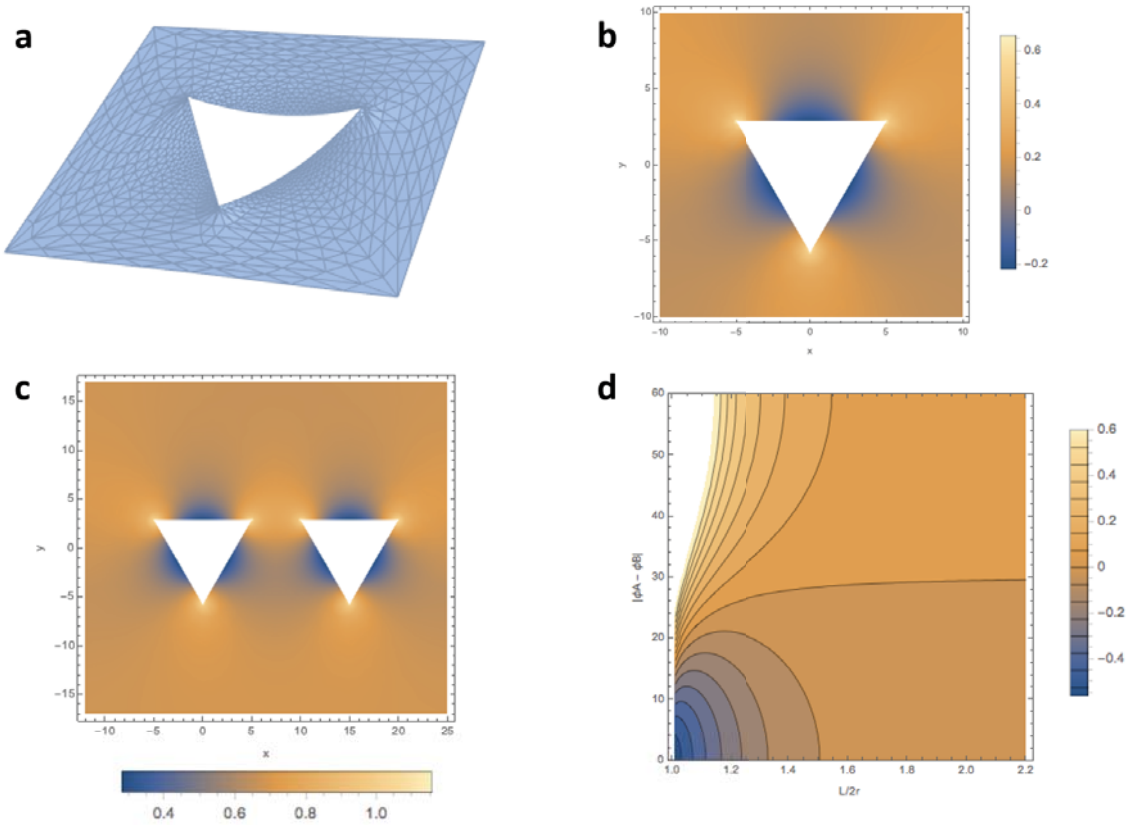

Figure 3-7 (contributed by Deshpreet Bedi). Modeling of interface height and capillary potentials for a T/L = 1/50 prism at a flat air-water interface. Surface evolver renderings of (a) interface attachment to a bowed T/L = 1/50 prism with negative polarity and (b) computation of interface height (positive values indicate a rising interface) as a function of distance from the prism's edge at all positions surrounding the prism. (c) Interface height landscape of two interacting T/L = 1/50 prisms with the same, negative polarity. (d) Pairwise capillary potential of two T/L = 1/50 prisms plotted as a function of prism-prism separation (L/2r) and relative angular orientation (ϕA-ϕB).

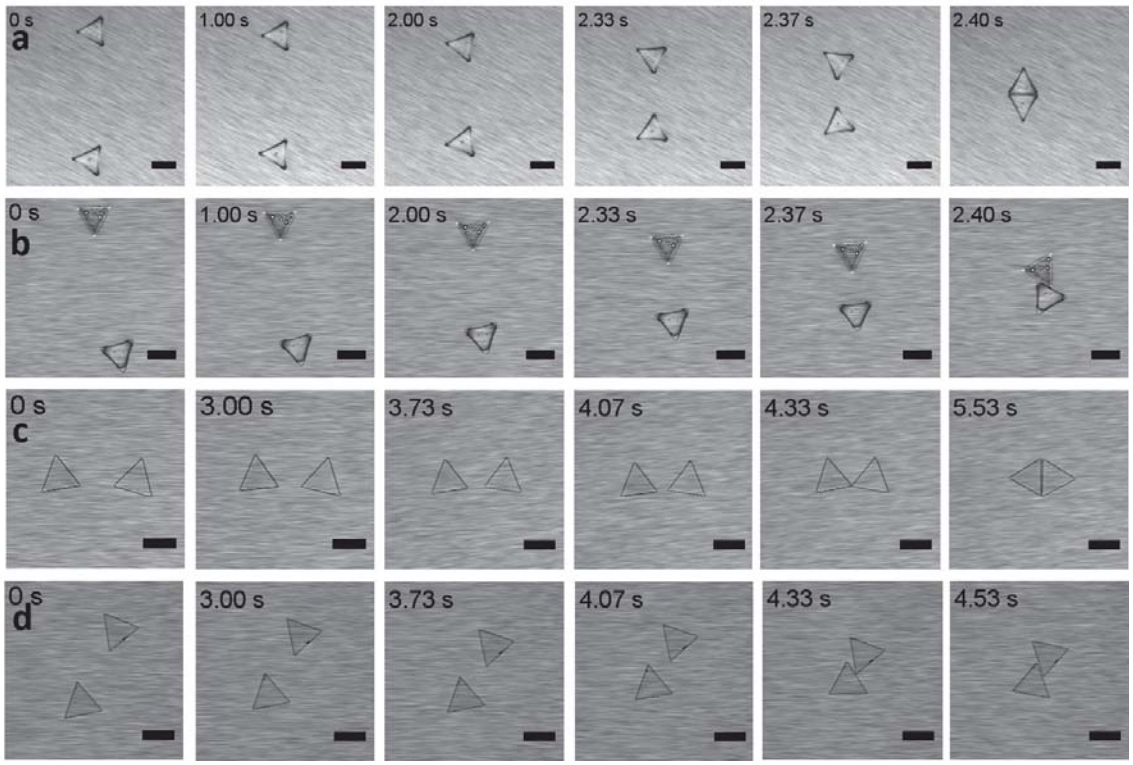

Figure 3-8. Characterization of pairwise interactions. Rows (a)-(d) Optical microscopy images of the 2 types of binding trajectories observed for polar prisms ($T/L \leq 1/10$), shown for $T/L = 1/50$ (rows (a) and (b)) and $T/L = 1/25$ (rows (c) and (d)). For prisms of $T/L = 1/50$ (rows (a) and (b)), contact occurs between the 5^{th} and 6^{th} images of each row. For prisms of $T/L = 1/25$ (rows (c) and (d)), contact occurs in the 5^{th} image of each row. Rows (a) and (c), tip-to-tip binding trajectory: the prisms approach and first contact occurs at the tips. The prisms then rotate into a collapsed, fully flush edge-to-edge orientation. Rows (b) and (d), tip-to-midpoint edge binding trajectory: the prisms approach and contact one another in an orientation such that the tip of one prism binds at the midpoint of the other prism's edge. The prisms then rotate into an edge-to-edge orientation in which the two edges are offset from each other by L/2. Scale bars are 100 μm.

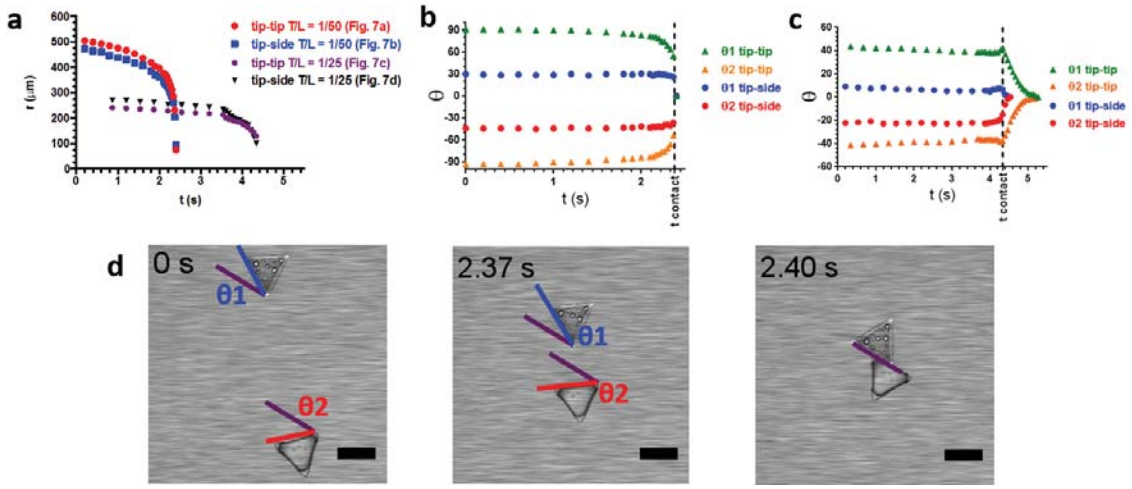

Figure 3-9. Analysis of Figure 3-8. (a) Time-evolution of center-to-center separation distance between 2 prisms approaching each other for each event shown in Fig. 8 rows (a)-(d). (b) and (c) time-evolution of relative angles of 2 prisms approaching each other for T/L = 1/50 and T/L = 1/25, respectively, for each event shown in Fig. 7 rows (a)-(d). Angles reported are between the binding edge and the binding edge's final, collapsed position. (d) Method of t1 and t2 measurement for tip-to-edge binding trajectory for T/L = 1/25 prisms (Fig. 8 row (a)).

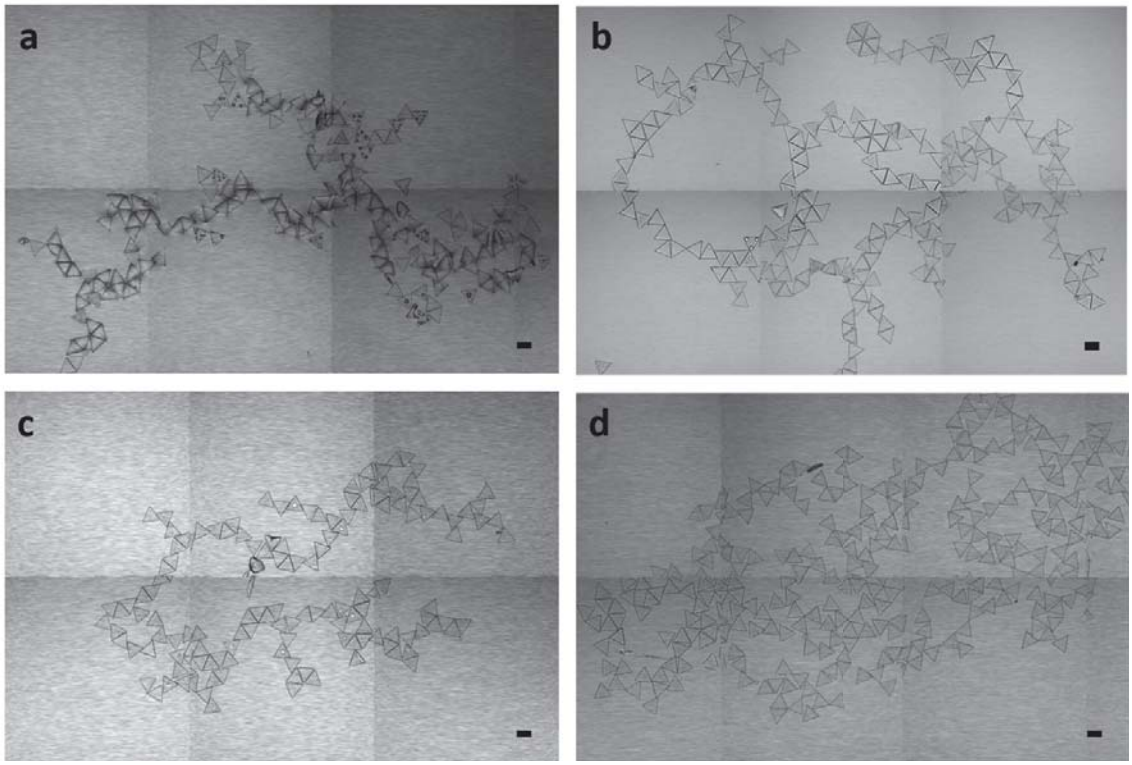

Figure 3-10. Self-assembled open networks from capillary-driven binding of thin triangular microprisms. (a) T/L = 1/50, (b) T/L = 1/25, (c) T/L = 1/10, and (d) T/L = 1/5 equilateral triangular microprisms. Scale-bars are 100 μm.

3.7 References

1. Bowden, N., Terfort, A., Carbeck, J. & Whitesides, G. M. Self-Assembly of Mesoscale Objects into Ordered Two-Dimensional Arrays. *Science* **276**, 233-235 (1997).

2. Bowden, N., Arias, F., Deng, T. & Whitesides, G. M. Self-Assembly of Microscale Objects at a Liquid/Liquid Interface through Lateral Capillary Forces. *Langmuir Langmuir* **17**, 1757-1765 (2001).

3. Pieranski, P. Two-Dimensional Interfacial Colloidal Crystals. *Physical Review Letters Phys. Rev. Lett. PRL* **45**, 569-572 (1980).

4. Onoda, G. Y. Direct observation of two-dimensional, dynamic clustering and ordering with colloids. *Physical Review Letters Phys. Rev. Lett. PRL* **55**, 226-229 (1985).

5. Horozov, T. S., Aveyard, R., Clint, J. H. & Binks, B. P. Order,àíDisorder Transition in Monolayers of Modified Monodisperse Silica Particles at the Octane,àíWater Interface. *Langmuir* **19**, 2822-2829 (2003).

6. Horozov, T. S., Aveyard, R., Binks, B. P. & Clint, J. H. Structure and Stability of Silica Particle Monolayers at Horizontal and Vertical Octane,àíWater Interfaces. *Langmuir Langmuir* **21**, 7405-7412 (2005).

7. Madivala, B., Fransaer, J. & Vermant, J. Self-Assembly and Rheology of Ellipsoidal Particles at Interfaces. *Langmuir Langmuir* **25**, 2718-2728 (2009).

8. Loudet, J. C., Alsayed, A. M., Zhang, J. & Yodh, A. G. Capillary Interactions Between Anisotropic Colloidal Particles. *Physical Review Letters Phys. Rev. Lett. PRL* **94**, 018301 (2005).

9. Lewandowski, E. P., Bernate, J. A., Tseng, A., Searson, P. C. & Stebe, K. J. Oriented assembly of anisotropic particles by capillary interactions. *Soft Matter Soft Matter* **5**, 886-890 (2009).

10. Lewandowski, E. P. et al. Orientation and Self-Assembly of Cylindrical Particles by Anisotropic Capillary Interactions. *Langmuir Langmuir* **26**, 15142-15154 (2010).

11. Sun, K., Souslov, A., Mao, X. & Lubensky, T. C. Surface phonons, elastic response, and conformal invariance in twisted kagome lattices. *Proceedings of the National Academy of Sciences* **109**, 12369-12374 (2012).

12. Kang, S.-M. et al. Capillarity-induced directed self-assembly of patchy hexagram particles at the air-water interface. *Soft Matter Soft Matter* **12**, 5847-5853 (2016).

13. Chen, Q., Bae, S. C. & Granick, S. Directed self-assembly of a colloidal kagome lattice. *Nature* **469**, 381-384 (2011).

14. Paulose, J., Meeussen, A. S. & Vitelli, V. Selective buckling via states of self-stress in topological metamaterials. *Proceedings of the National Academy of Sciences* **112**, 7639-7644 (2015).

15. Florijn, B., Coulais, C. & van, H., Martin. Programmable Mechanical Metamaterials. *Physical Review Letters Phys. Rev. Lett. PRL* **113**, 175503 (2014).

16. Buckmann, T., Thiel, M., Kadic, M., Schittny, R. & Wegener, M. An elasto-mechanical unfeelability cloak made of pentamode metamaterials. *Nat Commun* **5**, (2014).

17. Pelesko, J. A. *Self Assembly: The Science of Things That Put Themselves Together* (Chapman and Hall/CRC, 2007).

18. Whitesides, G. M. & Grzybowski, B. Self-Assembly at All Scales. *Science* **295**, 2418-2421 (2002).

19. Dong, J. et al. Effect of Triton X-100 on the stability of aqueous dispersions of copper phthalocyanine pigment nanoparticles. *Journal of Colloid and Interface Science* **362**, 33-41 (2011).

20. Mohammadi, M., Larson, E. D., Liu, J. & Larson, R. G. Brownian dynamics simulations of coagulation of dilute uniform and anisotropic particles under shear flow spanning low to high Peclet numbers. *The Journal of Chemical Physics* **142**, - (2015).

21. Souslov, A., Liu, A. J. & Lubensky, T. C. Elasticity and Response in Nearly Isostatic Periodic Lattices. *Physical Review Letters Phys. Rev. Lett. PRL* **103**, 205503 (2009).

22. Atwood, J. L. Kagome lattice: A molecular toolkit for magnetism. *Nat Mater* **1**, 91-92 (2002).

23. Cavallaro, M., Botto, L., Lewandowski, E. P., Wang, M. & Stebe, K. J. Curvature-driven capillary migration and assembly of rod-like particles. *Proceedings of the National Academy of Sciences* **108**, 20923-20928 (2011).

24. Paunov, V. N. Novel Method for Determining the Three-Phase Contact Angle of Colloid Particles Adsorbed at Air,àíWater and Oil,àíWater Interfaces. *Langmuir Langmuir* **19**, 7970-7976 (2003).

25. Brakke, K. A. The Surface Evolver. *Experimental Mathematics Experimental Mathematics* **1**, 141-165 (1992).

Chapter 4

Two-step continuous production of monodisperse colloidal ellipsoids at rates of one gram per day

4.1 Abstract

We report a two-step process for the continuous production of monodisperse polystyrene colloidal ellipsoids of aspect ratios up to 4.3 at rates that exceed 1.0 g per day. This production rate is nearly a 20x improvement over previous reported synthetic rates, which are based on batch processes. This scale up is accomplished by continuous production of a deformable polymer film with embedded colloidal spheres by evaporative processing of a dilute polymer solution. Then, in a second step, the film is continuously elongated at a temperature that stretches the embedded spheres into colloidal ellipsoids. The method is used to deform initially 1.0 μm polystyrene spheres into ellipsoids of variable aspect ratio, including ellipsoids of aspect ratio 1.31 $\pm$ 0.18, 3.03 $\pm$ 0.34, 3.89 $\pm$ 0.50, and 4.32 $\pm$ 0.52. For the case of aspect ratio 3.03 $\pm$ 0.34 ellipsoids, 850 mg of colloids were produced by producing and stretching a 3.3 meter long film of thickness 150 microns and width 10 centimeters in a total period of 16 hours. The realized yield of better than 1.0 g of colloidal ellipsoids per day opens up new possibilities for applications of monodisperse anisotropic colloids, such as self-assembly and optical

characterization of complex crystalline unit cells, as well as rheological characterization of both minimal gels and dense fluid suspensions of colloidal ellipsoids.

4.2 Introduction

Colloidal particles can undergo self-assembly into a variety of structures with useful functions. [1] Colloidal gels, which are self-assembled under conditions of strong, short-range attractive interactions, are one such example structure. Colloidal gels find application in the fields of consumer, agricultural, and pharmaceutical products. Concentrated colloidal suspensions with amorphous structure are used in architectural coatings and in ceramic formulations. [2] Colloidal crystals with close-packed structures yield optical properties such as iridescence and structural color. [3]

The function of each of these general structural classes – gels, dense amorphous suspensions, and crystals – can be augmented if the materials are produced from anisotropic colloids. For example, gels formed by depletion interactions of colloidal ellipsoids, as well as two-dimensional open networks of such ellipsoids, exhibit enhanced solid-like behavior as compared to similar structures self-assembled from colloidal spheres. [4-6] Similarly, dense, amorphous suspensions of rod-like fibers and tubular structures that are kinetically arrested due to either network cross-linking or particle jamming may break and reform upon application and removal of mechanical stress, resulting in viscoelastic behavior and mechanical rigidity. [2] Finally, crystalline unit cells self-assembled from colloids of anisotropic shape may possess symmetry that is more complex than [7-11] the simple face-centered and body-centered cubic (FCC and BCC) unit cells typically available from assembly of spheres. [12-14] Crystalline structures

assembled from colloids of anisotropic shape may possess the ability to scatter visible and infrared light in complex ways, which could yield new optical, photonic, and sensing applications. [15]

Additionally, anisotropic colloids often emulate natural and industrially relevant systems more closely than do systems of spheres. For example, gelation in both aqueous and organic solvents may occur via induced attractive interactions (either chemical interactions such as hydrogen bonding and network cross-linking, or simply by physical aggregation) between rod-shaped and helical solvent structures. This gelation yields viscoelastic rheological behavior. Gels of anisotropic colloids thus serve as physical model systems for liquid consumer products and other liquid soft matter systems. [2] Likewise, the complex crystalline unit cells described above draw their inspiration from instances in nature such as the iridescence of butterfly wings and animal camouflage, as described in the introduction to this dissertation. [3]

A key parameter affecting the structure and properties of such anisotropic colloidal systems is particle polydispersity, as particle jamming and kinetic arrest of crystalline unit cell induction and nucleation become increasingly likely as polydispersity increases. [16] Likewise, fundamental studies of glasses and gels use monodisperse particles in order to isolate and characterize the effect of colloid aspect ratio on system microstructure and mechanical properties.

One barrier to further progress is the lack of availability of monodisperse, anisotropic colloids in sufficient quantity for self-assembly studies and the evaluation of functional properties. To understand material requirements, consider that for a one-micron colloid, self-assembly of a 3D crystalline structure in an 8-well microscopy plate requires of order 10^{-2} grams of particles. A campaign of ~ 20 experiments therefore has a material requirement of order 10^{-1}

grams of particles. For rheological characterization of non-Newtonian properties of colloidal systems – which requires homogeneous sample volumes of at least 1 mL and particle volume fractions ranging between 5% (gels) and 50% (dense dispersions) – material requirements are increased to between 1 (gels) and 10 (dense dispersions) g of particles. Thus, processes to fabricate at least gram-scale quantities of monodisperse anisotropic colloids within a limited period are needed for such studies.

A few synthesis methods are capable of producing such quantities of monodisperse anisotropic colloids in less than a day of work. For example, emulsion polymerization methods, such as the polymerization of dimpled spheres from 3-trimethoxysilylpropyl methacrylate (TPM) and colloidal dimers, as well as top-down molding methods, such as the electrochemical etching/oxidation cycles of silicon wafers to produce silicon and silica rods. [17-19] These methods are however limited by material choice and by the family of anisotropic shapes that may be produced.

Alternatively, gram and kilogram-scale quantities of carbon nanotubes may be produced by chemical vapor deposition, arc discharge, and laser ablation, although in this case the particles are polydisperse. For example, commercially purchased carbon nanotube samples may vary in length by a factor of three and in diameter by a factor of two. This polydispersity has significant effects on nanotube mechanical and electrical properties. [20,21]

Monodisperse ellipsoids would be an excellent addition to the set of anisotropic colloids that could be synthesized at scales of one gram per day or greater. Ellipsoids are a building block that can be used to produce new functional properties in gels, suspensions, and crystals. For example, the enhanced rigidity exhibited by gels of ellipsoids as compared to spheres suggests that ellipsoids are excellent candidates to achieve gelation at very low volume fractions.

Moreover, dense suspensions of monodisperse ellipsoids may be less likely to form flocculates during application of shear stress. With regards to crystalline structures, highly dense, simple monoclinic unit cells with packing fractions exceeding that of cubic unit cells have been predicted, and would likely yield more complex scattering patterns than are afforded by cubic unit cells. [22-24]

Current ellipsoid production methods involve a series of batch procedures, which together take several days to complete. [5,14,25-34] Briefly, in these methods, colloidal spheres are cured within a thin polymer matrix, which may span up to tens of cm in length and width, at room temperature on a flat surface; curing of the film typically requires four or more days. Next, the film is cut into thin, uniform strips, each of which is elongationally deformed. The strip width – typically of ~ 1 cm – is set to ensure uniform stretching across the width of the film. The strips are then heated to temperatures that exceed the glass transition temperature (T_g) of the particles and are subsequently stretched by uniaxial deformation. The film becomes longer, narrower, and thinner as a result of the deformation; the embedded colloids are microscopically deformed into the ellipsoidal shape as a result of the macroscopic deformation.

Once stretched, the particles are held under tension while being allowed to cool to room temperature. As the temperature drops below the particle glass transition temperature, the ellipsoidal shape generated by the deformation is locked in. Then, the polymer matrix is dissolved in solvent, and the ellipsoids are released into solution. The current best available batch synthetic processes require several days to yield quantities of ellipsoids ~200 mg (equivalent production rate ~ 67 mg/day). These batch processes face hurdles in reaching gram-scale production rates required for self-assembly and functional studies such as rheology; specifically, the time and operational space needed to cure the increasingly large, defect free

films, as well as the sample volume throughput capacity of the stretcher apparatus as limiting factors. [29,32] Developing a continuous process to produce colloidal ellipsoids, which would more rapidly cure films and also possesses a throughput in the elongational phase, would address these limitations, and potentially extend production rates into new regimes.

In this paper, we report a process that concatenates the previously reported batch processes into a two-step, continuous process that produces gram-scale quantities of colloidal ellipsoids per day of operation. The process consists of two devices that each operates continuously; the first device cures colloidal spheres into a thin, deformable polymer matrix; the second device stretches this film and its embedded particles into ellipsoidal shape, by heating the film to temperatures greater than T_g of the particles. The device was used to produce 850 mg of polystyrene (PS) ellipsoidal colloids of aspect ratios between 1.31 and 4.32 over a 16-hour period. The standard deviation in the measures of ellipsoidal size is narrow, varying between 11.2 and 13.7% of the average aspect ratio across all trials, which is comparable to the previously reported size uniformity of the comparable batch processing methods. This production rate represents a 19x increase over the highest reported rate of ellipsoids produced by batch methods. This higher rate can support experimental studies of the assembly of anisotropic colloids into gels, suspensions and crystals. Additionally, the continuous operation of the device is scalable, and thus further development in production rate can be envisaged by increasing the width of the processing equipment and making the process more autonomous. [14,26,28-30,32-34]

4.3 Materials & Methods

Colloidal polystyrene (PS) ellipsoids are produced in a two-step process: the first process continuously produces a deformable poly(vinyl alcohol) (PVA) film with embedded PS spheres embedded in it (Fig. 1), the second process continuously stretches the film and spheres by uniaxial deformation at temperatures greater than T_g of both PS and PVA (Fig. 2). The operational parameters of both devices are digitally controlled (Arduino Uno CPU). All temperatures are monitored with thermocouples and regulated via feedback control within the electronics hardware.

4.3.1 Step 1: Continuous production of the deformable PVA film

In step 1, an aqueous mixture of PVA (10 wt. %) and $\leq$ 0.3 wt. % of spherical PS colloids is continuously dispensed onto a Teflon conveyer belt from a pressurized tank, and the conveyer belt carries the solution underneath a leveling bar and a series of four heat lamps. The heat lamps continuously evaporate water to cure the PVA and colloids into a 150 μm thick film embedded with PS colloids. At the end of the belt, the leading edge of the film is peeled from the belt with a razor and fastened, under tension, to an automated collection roller. The tension between the collection roller and the cured film at the end of the belt then continuously peels the cured film from the end of the belt as it is produced.

The PVA/PS solution is prepared as follows. DI water is added to PVA powder (Sigma, MW = 30,000 – 70,000 g/mol, 10 wt. %), in increments no larger than 100 mL of water to 10 g of PVA. The PVA and water is heated at 90 ˚C for several hours to enhance the saturation limit of the solution. The solution is then gently stirred (< 300 rpm, to avoid bubbling) on a hotplate

(~90 ˚C) overnight, at which point the PVA has dissolved. The hotplate's heating function is turned off, and the solution continues to stir until it has cooled to room temperature. $\leq$ 0.3 wt. % of either fluorescent (Thermo Fisher Scientific, Diameter = 1.0 $\pm$ 0.031 μm, 2% w/v) or undyed (Thermo Fisher Scientific, Diameter = 0.9 μm, 8% w/v, specification range 0.8 – 1.0 μm) sulfate-modified PS spheres are added in one aliquot and gently stirred to ensure a homogeneous distribution of colloids throughout the solution. Solution volumes between 150 and 515 mL are prepared, depending on the quantity of ellipsoids desired.

The prepared solution is loaded into a pressurized tank (V = 3.8 L, AllProducts Corp.). The tank is manually pressurized to 3 $\pm$ 1 PSI, and as shown in in Fig. 1c, the solution is dispensed onto a Teflon conveyer belt through Swagelok piping (OD = 0.3175 cm). The dispense rate of PVA solution is controlled by the pressure of the tank (pressurized via an in-house air supply), and by an automated valve (Parker Fluid Controls, 2-way Normally Closed Solenoid Valve). After passing the valve, the Swagelok piping passes through a splitting junction, where the piping forks, and then rejoins in a "U" geometry; this U-shaped region of piping is suspended several centimeters over the conveyer belt (Fig. 1c). 7 holes are present on the underside of the U-shaped section piping, and the solution dispenses from these holes onto the conveyer belt as it is pumped through this region. Splitting the piping, and thus the solution flow, into the U-shaped geometry ensures even distribution of the solution across the middle 10 cm of the 20.5 cm-wide belt. The edges of the belt are unconstrained and the solution dispense rate is monitored to ensure the solution does not spread off to the edges of the belt (as discussed in the next paragraph).

The motorized conveyer belt is powered by a stepper-motor (Dongzheng Motor Co., Planetary Geared Motor Stepper) and passes the solution through a thin gap (1 mm thick)

between the belt and a rectangular aluminum-leveling bar (1 x 1 x 10 cm^3), which produces a solution of a uniform height of several millimeters thick across its width. The solution height is greater than the gap between the bar and the belt, because the solution adheres to the flat, back edge of the bar after it passes through the 1 mm gap. The belt and solution then pass underneath four heat lamps in series, (Phillips Clear BR40, 125W) which cure the solution – through evaporation – until it forms a malleable, solid film, which is rolled up off the Teflon belt.

The most challenging operating parameter to control is the PVA/PS solution dispense rate. The ideal dispense rate (a) maintains a sufficient reservoir of PVA on the belt (before passing under the leveling bar) to prevent solution backflow during the curing process, but conversely (b) does not exceed a rate at which the reservoir overflows the belt's capacity. The high surface tension of the PVA solution makes this control challenging, as the presence of trace amounts of PVA in overflow regions (regions of the belt where PVA is driven off the unconstrained edge of the belt, due to a combination of gravity and solution spreading due to pressure gradients), creates a pathway for all of the PVA on the belt to flow off the belt's edge.

For the particular conveyor belt speed that ensures good production rates (0.63 cm/min) we empirically determined the ideal dispense rate to be approximately 50 mL/hr, which maintains a reservoir 2-3 mm thick, several cm wide, and extends ~3-5 cm behind the bar. If the solution spreading extends 7 cm behind the bar or extends 5 cm beyond the width of the bar, it reaches overflow areas, and the entire production run is lost. Additionally, the pressure of the tank may either fall (due to the tank emptying during processing) or rise (due to the in-house air pumping into the tank faster than solution is being emptied from the tank) by several hundredths of PSI per minute, and so the tank pressure must be controlled at all times. The PVA solution process is controlled by an operator so that the pressure is within 3 ± 1 PSI; this limit maintains

the reservoir within the size constraints indicated above. (The wide operating range of the tank's pressure exists because the optimal operating pressure may vary from one production run to the next, potentially due to clogging which emerged in the Swagelok piping from dried PVA used in previous fabrications.)

The relationship between the speed of the conveyer belt, the spacing of the heat lamps, and temperature of the lamps is set by an evaporation mass balance. We observe that longer drying times at lower temperatures yield more uniform films that are more likely to be free of major defects such as bubbling and ribbing instabilities, which arise more frequently during faster drying at higher temperatures. The optimized operating conditions were a conveyer belt velocity of 0.63 cm/min – which moves the solution ~100 cm from its dispense point to the collection roller in 158 minutes. 15 cm separate the front of the leveler from the center of the first lamp, and the centers of each subsequent lamp in the process are also spaced 15 cm apart.

The thermal energy input to the film by the heat lamps is controlled by maintaining a constant air temperature approximately two centimeters above the surface of the film. The air temperature is monitored with four thermocouples, each suspended by copper wire between the heat lamps and the belt (one thermocouple per heat lamp). Two thermocouples can be seen in Fig. 1 (one underneath the first heat lamp in frame (c) and one underneath the fourth heat lamp in frame (d)). Air temperature is regulated via the digital feedback control system, which automatically switches the heat lamps on and off to maintain the air temperatures under each lamp of (in order of the heat lamp/thermocouple that the film passes under) 82, 77, 63, and 87 °C.

When the leading edge of the film reaches the end of the belt, it is manually peeled from the belt with a razor blade and taped under tension to a motorized collection roller (Fig. 1d).

This tension peels subsequent lengths of the film off the Teflon belt and collects the film on the roller. After all of the PVA solution has been delivered, we raise the leveler so as to prevent adhesion between the leveler and the back edge of the film, which can cause defects within the drying film. Using this method, we have produced uniform films of up to 3.3 m in length with no major defects (Fig. 3). After processing is complete, the tank and Swagelok piping are flushed with ~20 mL of warm water, in order to mitigate future clogging of the delivery module by dried PVA.

4.3.2 Step 2: Continuous stretching of PVA film and its embedded PS spheres by uniaxial deformation at $T>T_g$

The film is prepared for elongational deformation by first drawing horizontal gridlines across its width. The gridlines, spaced 3 cm apart, are used to characterize the degree and uniformity of the elongational deformation imposed on the film. Second, we trim the outer edges of the film (~10% of the total width at each edge) to eliminate defects such as curling, and thickness non-uniformity, which arose in the first step and which can cause uneven stretching in the second step. [35,36] We ensure the film's width is uniform to ensure uniform elongational strain of both the film and the embedded colloids. Finally, the film is sealed with a thin layer of silicone oil (Dow Corning, Base component of Sylgard 184 Elastomer Kit, 99% purity), which minimizes film dehydration at elevated temperatures. Film dehydration can cause the mechanical failure of the film during stretching.

After preparation, the film's lagging edge is uniformly fastened with duct tape across its width to the stretching apparatus's feeding roller, and the film is tightly wound onto this roller.

43 cm – the length of the film's path between the feeding and stretching rollers - is left unwound as a leading edge, which passes through an insulated oven and is ultimately fastened across its width to a stretching roller. The feeding roller is placed sufficiently far from the oven (several cm) so as to prevent heating of the film while still wound onto the roller. The stretching roller is located sufficiently far from the oven (2-3 cm) to allow the film to cool to room temperature while under tension, so as to mitigate particle relaxation towards its initial spherical shape.

Near the leading edge of the oven, the film is pulled over a roller housed within the oven (Fig. 2c), which is free to rotate. This roller serves to smooth ripples and imperfections that arise during stretching. An example of such defects, which arise during stretching, is shown in Fig. 2d. Specifically, tension propagates though the film as it comes off the feeding roller, before it enters the oven, and generates ripples across the film's width. The feeding, smoothing, and stretching rollers are all equal in diameter (3.175 cm). The oven's spatial dimensions are 31 x 31 x 27 cm^3. The oven's frame is built from a commercially obtained erector kit (80/20 Inc.), and its floor, walls, and removable top are constructed from aluminum sheet metal, 0.3175 cm thick. A circular opening is cut in the removable top, where a heat gun (Genesis, 750/1500 W, Dual Temp Heat Gun) is positioned to bring the oven to operating temperature. A rectangular piece of sheet metal is braced between the top edges of the erector set directly below the heat gun in order to prevent direct application of heat to the film. The interior of the oven's floor, walls, and removable top are covered with fiberglass insulation (Owens Corning, EcoTouch Pink Insulation, ~1 cm thick).

Once the film is loaded, the oven is brought to its operating temperature of 120 °C, which is the operating temperature used in numerous reports of the PVA filmed stretching process during batch fabrication. [33,34] After the operating temperature is reached, the roller rotation is

initiated at constant, programmed rates. The stepper motor-powered stretching roller is capable of turning with an angular velocity between 1 and 7.8 times the angular velocity of the feeding roller. The feeding roller's angular velocity ranges from 0.024 to 0.053 cm/s. The film possesses end caps (fore and aft) that are not subjected to uniform stretching. The leading end cap is 35 cm in length (length of the film's path from the oven entrance-to-stretching roller) and lagging end cap is 43 cm in length (length of the film's path from the feeding roller-to-stretching roller). These end caps (which may or may not contain particles, see below) are discarded because they do not receive the target elongational deformation.

4.3.3 Film and colloid characterization

The stretched film is removed from the stretching roller. The gridline spacing is measured to characterize the elongational deformation (stretching) at all positions of the film, other than the end cap regions. Regions that deviate from the mean stretch ratio by more than 20% - which arise on occasion due to minor film defects – such as holes or tears in the film which may arise due imperfections in the belt surface, or debris which is unintentionally incorporated into the film during processing – are manually removed from the film for separate characterization. The uniformly stretched region is then placed into a beaker of isopropanol (IPA) and stirred to remove silicone oil from the film. After approximately 1 hour of stirring, the IPA is replaced, and the process is repeated at least twice more.

After silicone oil removal, film width measurements are recorded at ten evenly spaced points along the length of the film. The PVA matrix is then dissolved via stirring in DI water at room temperature for several hours, releasing the ellipsoids into solution. PVA is removed from

the solution via five centrifugation cycles (ThermoFisher Sorvall Legend X1R Centrifuge) at 5000g for 10 minutes. Ellipsoid major and minor axis length and aspect ratio are characterized with SEM (FEI Quanta 3D FEG) of 50 independent particles. Ellipsoid stability in bulk solution is characterized via direct imaging of Brownian motion of individual ellipsoids with confocal microscopy (Nikon A1Rsi, 100x objective, NA = 1.4).

4.4 Results & Discussion

4.4.1 PS colloid and PVA film strain mechanics during continuous uniaxial deformation

The film's measured elongational strain is plotted vs. the applied uniaxial strain in Fig. 4a. In continuous uniaxial extension, the applied uniaxial strain is equivalent to the ratio of the velocity of the film at the end of the stretching process to the velocity of the film at the beginning of the stretching process. [37] Here, this ratio of velocities is described by the ratio of the angular velocity of the stretching roller to the feeding roller, and strains of 1.4, 2.9, 5.6, and 7.8 are applied to continuously produce the elongation of the colloid-embedded film. To measure the film's elongational strain, we rely on the gridlines that are drawn on the film prior to stretching. The film's measured elongational strain is equivalent to the applied uniaxial strain, except for at the highest applied strain rate, where the mean measured elongational strain lags the expected strain by 8%.

Any discrepancy between the applied uniaxial strain and the elongational strain of the film must be due to either slippage of the film on the rollers or relaxation of the film after initial stretching. Such nonidealities are likely to propagate to the deformation of the embedded PS colloids, and so we seek to both quantify the effect of any error and to isolate its source with the

intention of mitigating these effects in future studies. From experimental observation, we verify that no slippage occurs: for the trial at the highest strain, the film's leading edge and roller were both marked at the point where they initially came into contact after the film was initially loaded into the stretching device. After stretching, it was observed that the marks did not move relative to one another. We thus conclude that the source of the 8% error between the applied and measured film elongational strain is due to film relaxation.

The measured colloidal ellipsoid aspect ratio is plotted vs. the film's elongational strain in Fig. 4b for both this report of continuous stretching, and reports from literature of batch stretching. [26,33] The continuously stretched ellipsoid aspect ratios are measured from the SEM images (Figs. 4d-g). Particle aspect ratios of 1.31 $\pm$ 0.18, 3.03 $\pm$ 0.34, 3.89 $\pm$ 0.50, and 4.32 $\pm$ 0.52 are produced by varying the applied strain. The ratio of the measured standard deviation in aspect ratio to the average aspect ratio remains in a narrow range of 11.2 – 13.7% across all applied strains, which is similar to reports of measured ellipsoid polydispersity from batch methods. After washing, the ellipsoids are released into a solution of DI water, and their stability is verified via direct observation of individual colloids undergoing Brownian motion (Fig. 4c, Movie S1).

At the two lowest applied strains, particle aspect ratio increases linearly at the same rate as the measured elongational strain of the film. At higher applied strains, particle aspect ratio plateaus. Across all strains, the measured aspect ratios are lower than that of those obtained at similar strains during batch processing of colloidal PS ellipsoids, where the aspect ratio exceeds the imposed strain. [26,33]

4.4.2 Colloidal ellipsoid yield compared to batch methods

We demonstrated the capacity to produce gram-scale quantities of colloidal ellipsoids in a single day of operation by operating the process for 16 consecutive hours – 12 hours of film fabrication (step 1) followed by 4 hours of stretching (step 2, including film prep time) at an applied strain of 5.6. This production yielded 850 mg of ellipsoids of aspect ratio 3.03 $\pm$ 0.34. Rendering this rate of production on a 24-hour basis yields a particle production rate of 1.27 g of ellipsoids per day. To achieve this yield, 515 mL of PVA/PS colloid solution was processed into a 330 x 9.8 cm piece of film.

In this production run, we deliberately made the lagging 60 cm free of colloids, in order to not sacrifice any particles in the lagging endcap. To accomplish this, 415 mL of an aqueous 10 wt. % PVA, 0.3 wt. % PS ellipsoids solution was first processed into the leading 270 cm of the film. Immediately after all of the particle-laden solution was dispensed, an additional 100 mL of an aqueous, colloid-free 10 wt. % PVA solution was processed, adding an additional 60 cm of particle-free film onto the lagging end of the film. The final film was 330 cm x 9.8 cm x 150 μm, and 70% of PS colloids were successfully harvested as uniform ellipsoids. If we had not added the particle-free lagging endcap, our fractional yield would have decreased from 70% to 59%. Theoretically, the leading end cap may also be made particle-free in the same way, increasing our fractional yield up to a theoretically possible 80%, with only the particles at the curled edges of the film needing to be sacrificed upon edge removal.

Table 1 compares our rates of continuous colloidal ellipsoid production to the rates reported from previously published accounts of batch ellipsoidal synthesis. To our knowledge, the highest rate of ellipsoid production using these batch processes is reported in ref. 29. In this study, ~ 200 mg batches of PS ellipsoids were produced over an estimated 3 day processing

period (the manuscript reports 2-3 days for film curing), resulting in a particle yield of 67 mg per day. The rate of ellipsoid production afforded by our semi-continuous process is then 19x greater than this best reported yield from batch processes.

Our enhanced production rate owes primarily to the rate at which we are able to process the PVA/PS solution: the two continuous devices processed twice the amount of solution (515 mL vs. 260 mL) over a period that was about 3-4.5 times shorter (2/3 day vs 2-3 days) than the equivalent batch process. Additionally, our highest achieved yield of 70% approximately doubles the 33% fractional yield reported in ref. 29. This improved batch yield is due to the smaller (relative) area of the continuously processed film's edges and endcaps relative to the typical batch film. These edges and ends stretch nonuniformly and must be discarded. Refinements of the batch method could address the problem of fractional yield; however, though to our knowledge, quantitative assessments of such improvement have not been reported. [28,32] Even if the fractional yield of the batch process is improved, the continuous process is still able to produce films at a faster rate, because of the method of curing.

As described in the introduction, there are ramifications for a greater than one gram per day yield of colloidal ellipsoids for studies in self-assembly of complex, dense crystalline unit cells and rheology of minimal gels and monodisperse, dense suspensions of anisotropic colloids. Assuming a 1 mL sample volume, 1.27 g of colloidal ellipsoids is sufficient material for 24 rheological measurements of a colloidal gel's viscoelastic properties ($\phi \sim 5\%$), or two rheometer measurements of a dense suspension's ($\phi \sim 50\%$) viscoelastic properties. Turning to colloidal self-assembly, 1.27 g of colloidal ellipsoids is sufficient material to supply hundreds to thousands of observations of colloidal crystallization ($\phi \sim 0.5$) in an 8 well-plate, with its volume of ~ 0.1 mL. Thus, one day of semi-continuous ellipsoid production ameliorates the need for

repeated and laborious multi-day batch syntheses, as would be needed to generate the same amount of material that can be generated in a single production run with the two-step continuous process.

4.4.3 Current limitations of the two-step continuous production method and potential process improvements

Fig. 4b shows that the aspect ratio of the ellipsoids produced by continuous stretching reached a plateau of 4.32 $\pm$ 0.52 with increasing elongational strain rates. The maximum aspect ratio currently realized therefore falls significantly short of the aspect ratios of ~ 10 that have been reported for batch synthesis methods. [29] If the aspect ratio vs applied strain curve continues to plateau at higher strains, then applied strains of 20 (nearly three times the highest strains applied here) or higher may be needed to achieve aspect ratios of 5 or higher.

At the highest elongational strains applied in this work (5.6 and 7.2), we observe that the film can become embrittled and prone to fracture, especially if it becomes dehydrated. Thus, simply applying a higher ratio of angular velocities between the stretching and feeding rollers seems more likely to cause film failure then to achieve the desired high aspect ratios. Moreover, such large elongational strains are not apparently required for the analogous batch processes.

Because the continuously processed film's measured (macroscopic) elongational strain does not exhibit the same plateau as the (microscopic) elongation of the ellipsoids, it is likely that the PS colloids experience relaxation from higher to lower aspect ratios – independent of the film elongational strain mechanics - either during the deformation, or after, prior to cooling below the particle T_g. That is, the microscopic ellipsoidal shape is generated by a combination of

affine deformation and relaxation, as commonly observed in the case of polymer blends. Therefore, the most promising path to achieving higher particle aspect ratios likely lies with arresting the colloid relaxation, either by freezing the colloids rapidly while they are still under tension, or by ensuring robust adhesion between the particles and film, which is observed during batch processing. [26] We speculate that the longer exposure of our continuously processed film to silicone oil (as compared to batch processes), may adversely affect adhesion of the colloids to the PVA matrix. In this reported continuous processing, the film is coated with silicone oil for as many as twenty minutes prior to stretching, and the stretching process itself may take several hours to complete, depending on the length of the film. During batch processing, the film and particles are placed in an oil bath for, at most, several seconds prior to and during stretching. [26, 29, 30, 32-34] Thus, silicone oil may penetrate the film more thoroughly during continuous processing. Because the silicone oil coating procedure is essential to ensuring mechanical integrity of the film during continuous stretching, modification of the sulfate-modified PS surface groups may be required to ensure more robust adhesion between the colloids and the PVA matrix.

Additionally, a yield of 1 g per day of processing falls short of the 10 g yield that would be necessary for a campaign of, say, 20 bulk rheology experiments of dense suspensions (ϕ~50%) of colloidal ellipsoids. The greatest scope to increase the production level by another order of magnitude would be to intensify the rate of PVA/PS solution processing in the film formation step (continuous step 1). That is, to reach this 10 g yield, one would need to produce the PVA film with embedded colloids at faster rates. The simplest way to process the solution at a faster rate would be to make the film wider, as all of the optimized process parameters (other than the width capacity of the equipment) could be held constant without further refinement.

The solution processing rate scales proportionally with film width. Within the existing device, we can envisage an increase in width of no more than about 2x. Other methods are therefore needed to increase the production rate beyond this limit.

Intuitively, the rate of solution processing could also be increased by (i) making the film thicker, or (ii) by increasing the rate of evaporation by processing at higher temperatures, thus allowing the conveyer belt speed to be increased. However, when these process changes were tested (i) by increasing the space between the leveling bar from 1 to 2 mm, and, in a separate trial, (ii) by increasing both the thermocouple temperatures and the conveyer belt speed by ~20%, we observe mechanical defects such as bubbling and ribbing instabilities when evaporation occurs through solution that is too thick, or when evaporation occurs too quickly.

Other possibilities to expedite the rate of film production may include rapid fabrication of the PVA matrix by melting PVA powder, then molding it into a uniform thin film via extrusion, and separately introducing the PS spheres before the solid PVA matrix reforms, or UV-curing with a photocurable elastomeric matrix, though chemical and physical stability challenges (in the extrusion process, for example, introducing the PS spheres at a point where the PVA is still in a liquid state, but at a low enough temperature that the colloids would not be deformed, or in the UV-curing process, ensuring chemical inertness between the embedded colloids and the matrix material) would likely need to be addressed.

In addition, currently, the process must be continually monitored by an operator to manually control the PVA/PS solution delivery rate so that a sufficient reservoir of solution on the belt is maintained without allowing solution overflow. Ideally, this step in film production can be made autonomous, such that it could run unattended, with only brief operator checks several times daily for safety, much like a chemist performing a multi-day reaction in a flask.

Such autonomous operation would require more precise control of the solution delivery rate than is currently afforded by manual control of the tank's internal pressure, and perhaps a feedback control between the amount of PVA/PS solution on the belt and the solution dispense rate. Adaptations such as these proposed improvements would exploit the inherent scalability in time of the continuous process, thereby realizing the true potential of the jump from a batch to continuous synthesis process.

Finally, the process may also be adapted to continuously stretch colloidal spheres of other materials into an ellipsoidal shape. For example, poly(methyl methacrylate) (PMMA) ellipsoids are currently fabricated by batch uniaxial extension of films of polydimethylsiloxane (PDMS) laden with PMMA spheres at $T > T_g$, in a process that is conceptually similar to the batch fabrication of PS ellipsoids. Challenges in adapting the process to different systems are related to the fundamental physical and chemical properties of the different materials. In the case of the PDMS/PMMA system, the primary challenge is in the curing of the PDMS matrix. Unlike the PVA matrix, which cures by evaporation, the PDMS matrix is cured via covalent PDMS cross-linking. For the PDMS batch curing process, effective cross-linking requires optimal concentrations of cross-linker and catalyst reagents, and a two-step curing process, which involves a step change in temperature. [5,25,27] To scale this curing process for continuous processing, cross-linking must not begin until the PDMS/PMMA solution is delivered to the conveyer belt, and sufficient energy must be delivered to the film so as to enhance the rate of curing without adversely affecting cross-linking chemistry. Additionally, a sharp step-change in temperature must be introduced within the process; it is unclear whether the current spacing of the series of four heat lamps in our continuous process would accomplish this. Nevertheless, scale-up of uniaxial deformation processes to new colloid-embedded elastomeric films for the

fabrication of ellipsoidal colloids is likely achievable through material-specific optimization of process geometry and operating parameters.

4.5 Conclusion

In this work, we scale-up the rate of colloidal ellipsoid production via uniaxial extension of colloidal spheres embedded in an elastomeric matrix by concentrating a series of batch processes into a two-step, semi-continuous process. Through our semi-continuous processing, we demonstrate the capacity to fabricate 1.27 g of ellipsoids/day, which represents a 19x improvement as compared to the best-reported yields from analogous batch methods. Our process has been demonstrated to produce ellipsoids up to aspect ratio 4.32 ± 0.52. This limiting aspect ratio appears to result from relaxation of the colloids during and immediately after the elongational deformation. We identify paths to increase both the production rate and aspect ratio of the continuous production process, through incremental improvements. The equipment for the two-step continuous process is straightforward to construct, and the control systems are derived from commercially available hardware and open source software; the method is therefore easy to replicate elsewhere. The fabrication rates demonstrated here open up new avenues for the functional characterization of colloidal gels, suspensions, and crystals, produced from ellipsoids colloids.

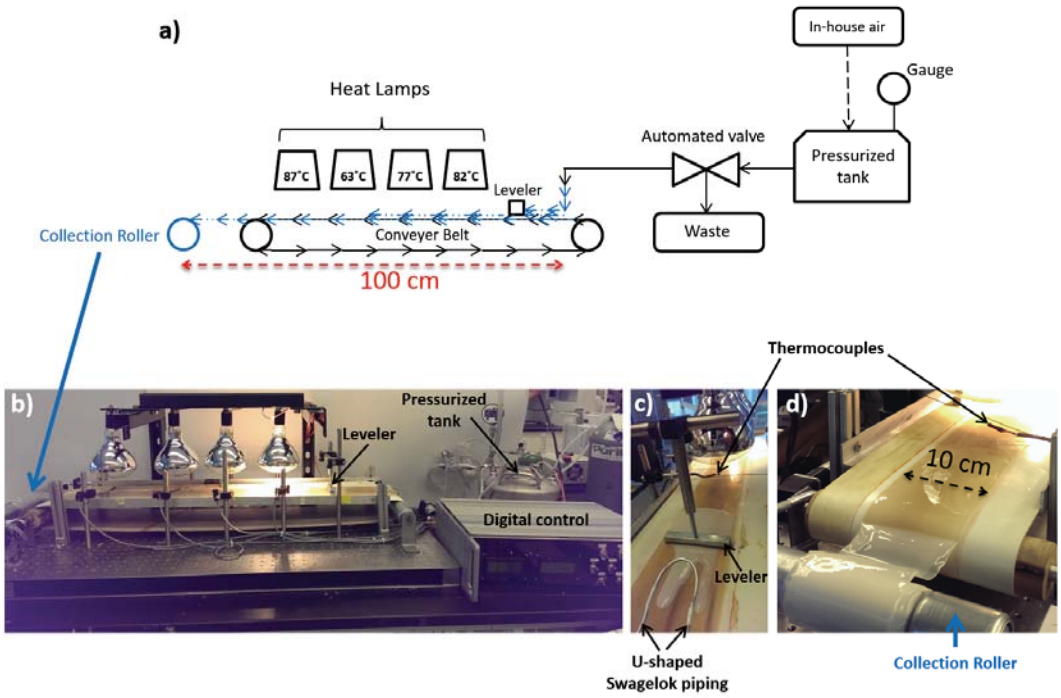

Figure 4-1. Continuous production of PVA film embedded with PS colloidal spheres. (a) Process flow diagram and (b) photograph of the processing equipment. A pressurized tank is charged with an aqueous solution of 10 wt% PVA, $\leq$ 0.3 wt% PS colloid spheres to an operating pressure of 3 $\pm$ 1 PSI. The solution is pumped through Swagelok tubing and (c) dispensed onto a motorized conveyer belt. The dispensed solution passes under a leveling bar, and is subsequently cured by 4 heat lamps in series (82, 77, 63, and 87 ˚C). The temperature maintained by the heat lamps is monitored with thermocouples (suspended by copper wire between the heat lamps and the belt, one is visible in frames (c) and (d)) and regulated via feedback control with an open source electronics hardware and software (Figure S1), which turns the heat lamps on and off to maintain process temperature. (d) At the end of the belt, the cured film is peeled off the belt and attached to a motorized collection roller.

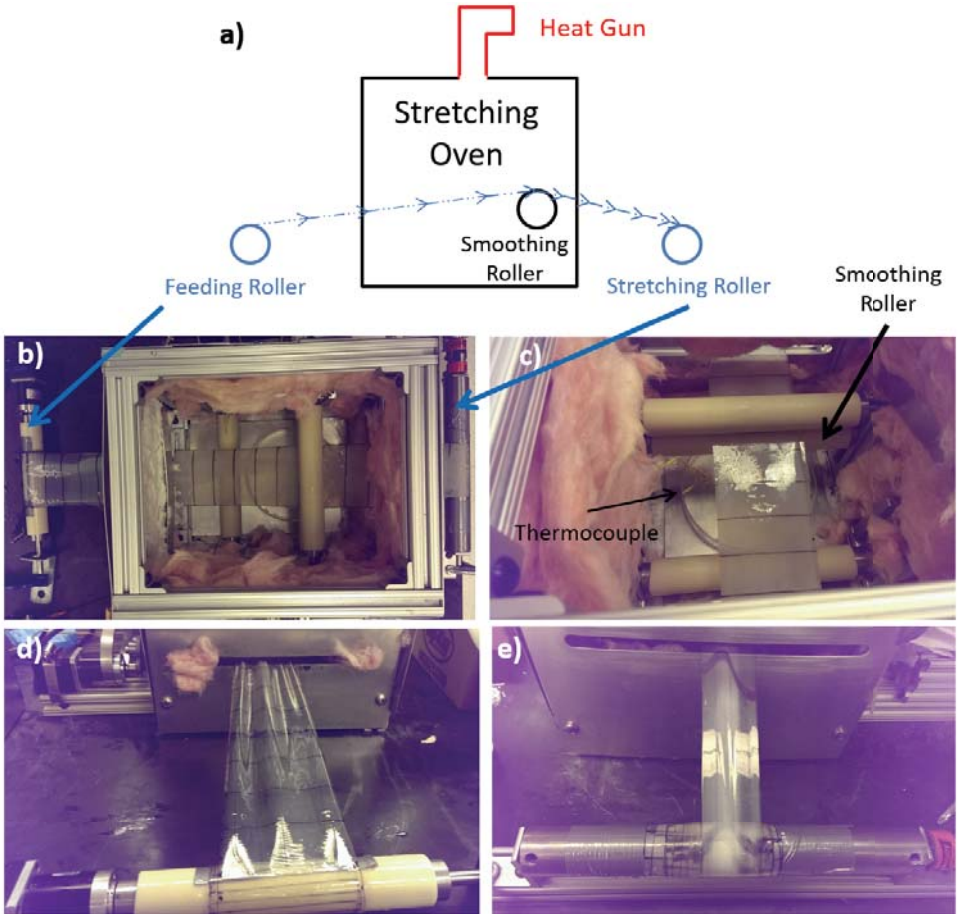

Figure 4-2. Continuous stretching of PS colloid-embedded PVA film at T > T_g. (a) Process diagram and (b) top-down photograph of the film loaded into the equipment prior to stretching. The film is securely fastened across its width to, and tightly wrapped around, a feeding roller. Its leading edge passes through an oven, is pulled under light tension over a freely rotating smoothing roller, and is securely fastened across its width to a stretching roller. (b) and (c) Three rollers are pictured in the oven: a single roller which the film passes over and a pair of rollers which the film passes between. Only the bottom roller in the pair of rollers is used in the stretching process described here; neither of the other rollers make contact with the film. After loading the film, the oven is closed and brought to process temperatures (T = 120 C) with a heat gun. The temperature is monitored with a thermocouple (yellow wire visible in (b) and (c)) and regulated via feedback control with an open source electronics hardware and software (Figure S1). Once process temperature is achieved, the stretching and feeding rollers begin turning at an angular velocity ratio of between 1 and 7.8. (d) Photograph of the film coming off of the feeding roller and entering the oven during stretching. Ripples appear in the film during stretching. (e) Photograph of the film exiting the oven onto the stretching roller. The film has narrowed and elongated, and the ripples from (d) have been eliminated by the internal smoothing roller. The wavy pattern of the gridline owes to the rippling of the film prior to smoothing. The pattern's shape is repeated along the length of the film, and is thus indicative of uniform stretching across the width of the film.

Figure 4-3. Photograph of the largest piece of film produced by Step 1. The film is 330 cm long, 10 cm wide, and ~150 μm thick. 515 mL of PVA solution was processed in the fabrication of this film. The leading 270 cm (415 mL solution) contains a colloid particle concentration of 3.0 mg/mL, the lagging 60 cm (100 mL solution) was processed with no particles in order to keep particles out of the nonuniformly stretched lagging endcap.

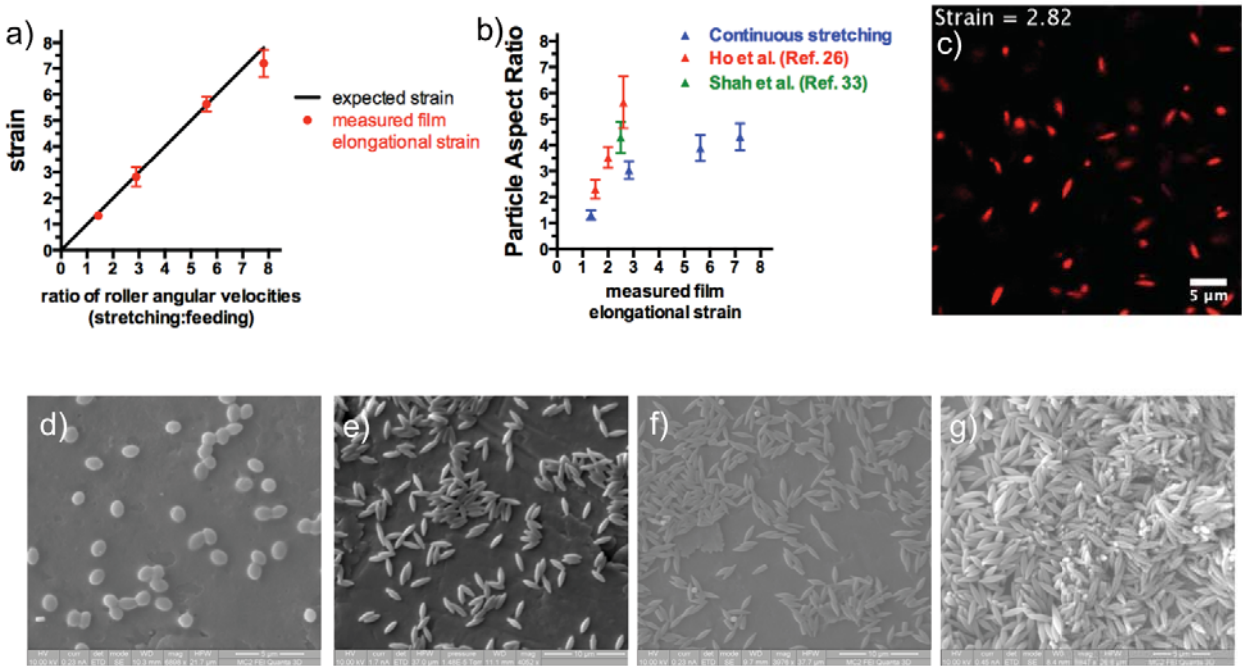

Figure 4-4. Colloidal ellipsoids and Elongational strain of PVA film produced by continuous uniaxial deformation using the equipment shown in Figure 4-2. (a) Measured elongational strain of the PVA film as a function the ratio of the angular velocity of the stretching roller to the feeding roller. The expected elongational strain of the film is equal to the ratio of the roller velocities. (b) Particle aspect ratio as a function the elongational strain of the PVA film (plotted in (a)). Aspect ratio for continuously stretched colloids initially increases linearly with film elongational strain, but plateaus at higher strains. Also plotted are particle aspect ratios produced during batch processing by stretching between moving clamps (Ref. 26 and 33), which do not plateau and consistently exceed the aspect ratios produced by continuous stretching. (c) Confocal microscopy image of ellipsoids produced at a strain of 2.82 stable and dispersed in DI water. (d)-(g) SEM images of colloidal ellipsoids. Aspect ratios are (d) 1.31 $\pm$ 0.18, (e) 3.03 $\pm$ 0.34, (f) 3.89 $\pm$ 0.50, (g) 4.32 $\pm$ 0.52.

Method	Year	Volume elastomer-particle solution (mL)	particle mass/elastomer-particle solution volume (mg/mL)	Aspect Ratios	Yield per batch (mg)	batch processing time	yield per day (mg/day)	highest fractional (%) yield
Ho and Ottewill	1993	70	0.8		56 x %yield (unknown)	1 day		
Madivala et al.	2009	260	2.3	1.25 - 10	200	3 days	67	33%
Shah et al.	2012 2013 2014	8	0.8	2-7	2.08	1 day	2	33%
Crassous et al.	2014	515	0.8	2.1 - 8.8		4 days		
Palangetic et al.	2016	496	0.56		276 x %yield (unknown)	4 days*		
Semi-continuous Processing (this work)	2017	515	3.0	1.31 - 4.32	850	2/3 day	1270	70%

* estimate based on reported curing time for similar-sized film from Crassous et al.

Table 4-1. Comparison of PS colloidal ellipsoid production rates and aspect ratios from seven previous reports of batch fabrication (rows 1 – 5) and our reported two-step, continuous process (row 6). Our report is highlighted in yellow, as is the highest reported (to our knowledge) yield of colloidal ellipsoids from batch processing. Yield per day is reported as the mass of particles yielded per batch on a 24-hour time scale of processing. The final column reports the highest fractional (percent) yield, which is defined as the highest reported ratio of the number of uniform ellipsoids obtained to the number of colloidal particles embedded in the elastomeric matrix for each process. The 4-day batch processing time for the report from Palangetic et al. is not reported, but rather, estimated based on reported curing times for similar-sized films in Crassous et al.

4.6 References

1. Cheng, Z. et al. Phase diagram of hard spheres. *Materials & Design* **22**, 529-534 (2001).
2. Solomon, M. J. & Spicer, P. T. Microstructural regimes of colloidal rod suspensions, gels, and glasses. *Soft Matter Soft Matter* **6**, 1391-1400 (2010).
3. Marlow, F., Muldarisnur, Sharifi, P., Brinkmann, R. & Mendive, C. Opals: Status and Prospects. *Angewandte Chemie International Edition Angewandte Chemie International Edition* **48**, 6212-6233 (2009).
4. Manley, S. et al. Limits to Gelation in Colloidal Aggregation. *Physical Review Letters Phys. Rev. Lett. PRL* **93**, 108302 (2004).
5. Mohraz, A. & Solomon, M. J. Gelation and internal dynamics of colloidal rod aggregates. *Journal of Colloid and Interface Science* **300**, 155-162 (2006).
6. Wilkins, G. M. H., Spicer, P. T. & Solomon, M. J. Colloidal System To Explore Structural and Dynamical Transitions in Rod Networks, Gels, and Glasses. *Langmuir Langmuir* **25**, 8951-8959 (2009).
7. Pfleiderer, P. & Schilling, T. Simple monoclinic crystal phase in suspensions of hard ellipsoids. *Physical Review E Phys. Rev. E PRE* **75**, 020402 (2007).
8. Beltran-Villegas, D. J., Schultz, B. A., Nguyen, N. H. P., Glotzer, S. C. & Larson, R. G. Phase behavior of Janus colloids determined by sedimentation equilibrium. *Soft Matter Soft Matter* **10**, 4593-4602 (2014).
9. Damasceno, P. F., Engel, M. & Glotzer, S. C. Crystalline Assemblies and Densest Packings of a Family of Truncated Tetrahedra and the Role of Directional Entropic Forces. *ACS Nano ACS Nano* **6**, 609-614 (2012).
10. Damasceno, P. F., Engel, M. & Glotzer, S. C. Predictive Self-Assembly of Polyhedra into Complex Structures. *Science* **337**, 453-457 (2012).
11. Vacha, R. & Frenkel, D. Relation between Molecular Shape and the Morphology of Self-Assembling Aggregates: A Simulation Study. *Biophysical Journal* **101**, 1432-1439 (2011).
12. Pusey, P. N. et al. Hard spheres: crystallization and glass formation. *Philosophical Transactions of the Royal Society of London A: Mathematical, Physical and Engineering Sciences* **367**, 4993-5011 (2009).
13. Pusey, P. N. & van, M., W. Phase behaviour of concentrated suspensions of nearly hard colloidal spheres. *Nature* **320**, 340-342 (1986).
14. Shah, A. A., Ganesan, M., Jocz, J. & Solomon, M. J. Direct current electric field assembly of colloidal crystals displaying reversible structural color. *ACS Nano* **8**, 8095-8103 (2014).
15. Glotzer, S. C. & Solomon, M. J. Anisotropy of building blocks and their assembly into complex structures. *Nat Mater* **6**, 557-562 (2007).

16. Schope, H. J., Bryant, G. & van, M., William. Effect of polydispersity on the crystallization kinetics of suspensions of colloidal hard spheres when approaching the glass transition. *The Journal of Chemical Physics The Journal of Chemical Physics* **127**, 084505 (2007).

17. Mock, E. B. & Zukoski, C. F. Emulsion Polymerization Routes to Chemically Anisotropic Particles. *Langmuir Langmuir* **26**, 13747-13750 (2010).

18. Sacanna, S., Irvine, W. T. M., Rossi, L. & Pine, D. J. Lock and key colloids through polymerization-induced buckling of monodisperse silicon oil droplets. *Soft Matter Soft Matter* **7**, 1631-1634 (2011).

19. van, K., Carlos M., Johnson, P. M., van, d. M., Jan E. A. M. & van, B., Alfons. Synthesis of Monodisperse High-Aspect-Ratio Colloidal Silicon and Silica Rods. *Langmuir Langmuir* **20**, 11201-11207 (2004).

20. Joselevich, E., Dai, H., Liu, J., Hata, K. & H., W., Alan (eds Jorio, A., Dresselhaus, G. & Dresselhaus, M. S.) 101-165 (Springer Berlin Heidelberg, Berlin, Heidelberg, 2008).

21. Shehzad, K. et al. Effect of the carbon nanotube size dispersity on the electrical properties and pressure sensing of the polymer composites. *Journal of Materials Science* **51**, 11014-11020 (2016).

22. Donev, A., Stillinger, F. H., Chaikin, P. M. & Torquato, S. Unusually Dense Crystal Packings of Ellipsoids. *Physical Review Letters Phys. Rev. Lett. PRL* **92**, 255506 (2004).

23. Frenkel, D. & Mulder, B. M. The hard ellipsoid-of-revolution fluid. *Molecular Physics Molecular Physics* **55**, 1171-1192 (1985).

24. Pfleiderer, P. & Schilling, T. Simple monoclinic crystal phase in suspensions of hard ellipsoids. *Physical Review E Phys. Rev. E PRE* **75**, 020402 (2007).

25. Keville, K. M., Caruthers, J. M. & Franses, E. I. Characterization of dimensions of ellipsoidal microparticles via electron microscopy. *Journal of Microscopy* **142**, 327-340 (1986).

26. Ho, C. C., Keller, A., Odell, J. A. & Ottewill, R. H. Preparation of monodisperse ellipsoidal polystyrene particles. *Colloid Polym Sci* **271**, 469-479 (1993).

27. Mohraz, A. & Solomon, M. J. Direct Visualization of Colloidal Rod Assembly by Confocal Microscopy. *Langmuir Langmuir* **21**, 5298-5306 (2005).

28. Crassous, J. J. et al. Field-induced assembly of colloidal ellipsoids into well-defined microtubules. *Nature Communications* **5**, 5516 (2014).

29. Madivala, B., Vandebril, S., Fransaer, J. & Vermant, J. Exploiting particle shape in solid stabilized emulsions. *Soft Matter Soft Matter* **5**, 1717-1727 (2009).

30. Madivala, B., Fransaer, J. & Vermant, J. Self-Assembly and Rheology of Ellipsoidal Particles at Interfaces. *Langmuir Langmuir* **25**, 2718-2728 (2009).

31. Mukhija, D. & Solomon, M. J. Translational and rotational dynamics of colloidal rods by direct visualization with confocal microscopy. *Journal of colloid and interface science* **314**, 98-106 (2007).

32. Palangetic, L. et al. From near hard spheres to colloidal surfboards. *Faraday Discussions Faraday Discuss.* **191**, 325-349 (2016).

33. Shah, A. A. et al. Liquid crystal order in colloidal suspensions of spheroidal particles by direct current electric field assembly. *Small* **8**, 1551-1562 (2012).

34. Shah, A. A., Schultz, B., Zhang, W., Glotzer, S. C. & Solomon, M. J. Actuation of shape-memory colloidal fibres of Janus ellipsoids. *Nat Mater* **14**, 117-124 (2015).

35. Siemann, U. in *130* 1-14 (Springer Berlin Heidelberg, 2005).

36. Penwell, R. C. & Chow, T. S. Minimizing curl induced upon drying layered solvent coated films. *Polymer Engineering & Science Polym Eng Sci* **25**, 367-373 (1985).

37. Macosko, C. W. *Rheology: Principles, Measurements, and Applications* (Wiley-VCH, 1994).

Chapter 5

Conclusion and future work

The objective of this work was to characterize the kinetics and precise mechanisms of an established colloidal self-assembly method, explore the self-assembly and pair-binding behavior of a new class of microfabricated particles, and support the experimental study of colloidal ellipsoids in bulk solution through semi-continuous, high throughput fabrication of these shape-anisotropic colloids.

In Chapter 2, we measured the kinetics of the assembly of colloidal spheres in a DC electric field, and the kinetics of the subsequent particle relaxation upon the removal of the field. First, the kinetics of particle electrophoretic deposition and osmotic pressure-driven relaxation were measured at a range of Pe by characterizing $\phi(z,t)$ using a novel combination of confocal microscopy and image analysis. $\phi(z,t)$ was then modeled by reparameterizing a 1D convection-diffusion transport model from the sedimentation literature. Variables that needed to be reparameterized were the particle mobility function ($K(\phi)$) in an electrophoretic system, the free particle convective mobility (U_0), and the compressibility factor ($Z(\phi)$) for our charged sphere system. The model was successfully validated at Pe ~ 0.2 where crystalline sediments were formed. Crystallinity spreads through the sediment with time-evolved, 1D-propagation of a crystalline front up the electrophoretically deposited sediment. The growth rates of the front were measured at both Pe conditions where crystalline sediments are obtained. Comparison of

the measured front growth rates to characteristic volume fraction growth rates, as predicted by the validated transport model, show that the crystal front grows with characteristic volume fractions corresponding to equilibrium fluid-crystalline phase transitions.

The validated model informs the kinetic design of reversible assembly applications; it predicts the time needed to grow and melt crystals of a given size, which predicts the time needed to turn properties owing to a crystalline structure "on" and "off". To extend this work, the model should be validated for systems that are more pragmatic for applications. For example, the one-hour time scale needed to induce crystallization is significantly longer than could be afforded by a commercial display application. By increasing the initial volume fraction to a value near the equilibrium fluid-crystalline phase transition volume fraction ($\phi \sim 35\%$), the kinetics of this reversible assembly could be greatly enhanced. Challenges would be largely experimental, such as ensuring stability of the colloids in dense suspension, as well as avoiding a glass transition in such a crowded suspension.

Additionally, the $K(\phi)$ function (Fig. 2-11) suggests that electrophoretic colloids are more mobile in concentrated suspensions than are colloids at equilibrium. Specifically, at $\phi \geq 35\%$, solvent backflow and interparticle hydrodynamic and electrostatic interactions retard particle mobility at equilibrium approximately 10 times more than they do the mobility of electrophoretic particles, primarily due to a cancelling of interparticle hydrodynamic and electrostatic effects between electrophoretic particles. [1] Retardation of particle mobility at these high volume fractions is the source of kinetically arrested non-equilibrium structures such as dense, amorphous glasses. Thus, mitigation of mobility retardation, perhaps through application of DC electric fields to dense suspensions, may represent a tool for annealing kinetically-trapped colloids into ordered crystals.

In Chapter 3, we observed capillary-driven binding of thin, triangular prisms at a flat air-water interface. At small T/L ratios (T/L $\leq$ 1/10), physical bowing of the prisms led to two observed prism polarity states; the prisms' center of mass sat either above or below the air-water interface. For both polarity states, the interface pins to the corner of the edge and the concave prism face, which results in a capillary hexapole; the interface curves in opposite directions at the prism's three tips and three sides. The coupled effect of polarity and hexapolar interactions results in two different pair-binding trajectories: a tip-to-tip binding trajectory between prisms with the same polarity, and a tip-to-edge binding trajectory between prisms with the opposite polarity. In both trajectories, prisms ultimately collapse into flush edge-edge contact. Thicker prisms (T/L = 1/5) are not bowed, and thus neither prism polarity nor evidence of hexapolar interactions are observed. Prisms of all T/L ratios self-assemble into "disordered" open networks – open networks with voids that are nonrepeating in their size and shape. The effects of inhomogeneity in prism wetting – imparted to the prisms with plasma treatment during their fabrication – is unclear, although prism polarity and hexapoles arise at thin T/L ratios with or without plasma treatment.

The merits of using microfabricated particles instead of colloids at interfaces is in the ability to control capillary anisotropy with particle shape, which permits targeting ordered structures for self-assembly. Equilateral triangles are the fundamental building block of the ordered kagome lattice, and thus realizing the full potential of triangular prisms calls for assembly of this target structure. The kagome lattice is constructed entirely of tip-tip bonds between the triangle building blocks, and the angle between all adjacent edges of all bound triangles must be equal to 120. [2] Thus, self-assembly of the kagome lattice from capillary interactions of thin triangular prisms requires (a) elimination of multiple polarity states (and thus

the tip-edge binding trajectory) and (b) tip-tip bonds which rotate and permanently bind into a conformation which yields the 120 angle between adjacent edges of bound triangles. As demonstrated by capillary-driven binding of right cylinders, condition (b) may be achieved through the introduction of curvature in the z-plane. If the prism's flat edge were curved in this z-plane, and the tips of the triangle were flattened, an excess of interface area would induce permanent tip-tip binding in the required orientation. [3,4] Fabricating such a prism might be achievable with advanced microfabrication techniques, such as 3D-printing or polymer molding. Our study in chapter 3 elucidates the challenge presented by criterion (a), and suggests that multiple polarity states may be eliminated by making prisms sufficiently thick. Thus, fabrication and placement of thick ($T/L \geq 1/5$) prisms with edges curved in the z-plane at a fluid-fluid interface satisfies criteria (a) and (b), and may yield an ordered kagome lattice. Alternatively, control over the polarity of thin prisms – perhaps through application of an external field – may also satisfy criterion (a), and blunting the tips of the prisms to make initial bonding permanent may satisfy criterion (b).

While self-assembly of the kagome lattice was not achieved in chapter 3, open networks with a structure indicative of mechanical rigidity were fabricated. To fully demonstrate the utility of these networks, enhanced rigidity of the networks as compared to close-packed arrays of isotropic spheres must be demonstrated, and the networks must be self-assembled at substrates that may benefit from these enhanced mechanics. The network's mechanical properties may be characterized relative to close-packed arrays of spheres by comparing the time-evolved and maximum-observed surface pressure sustained by each structure during 1D compression in a Langmuir-Blodgett trough. The open network's structure could also be observed with microscopy during compression, in order to characterize buckling and failure mechanisms of the

voids. [5,6] The networks, and their enhanced mechanics, could be delivered to the interface of oil-in-water or water-in-oil emulsion droplets by microfluidic droplet fabrication. [7] Preliminary results of network self-assembly at the interface of isopropanol droplets in a continuous CHB/Decalin phase are shown in Fig. 5-1. The droplets shown were manually (non-continuously) produced, and their synthesis is not yet repeatable. Once the synthesis of this particle stabilized-emulsion is perfected, open network-stabilized droplets may be subjected to atomic force microscopy (AFM) stresses. The maximum sustainable stress of these droplets may be compared to the same AFM measurements of unstabilized droplets and traditional Pickering emulsions (droplets stabilized by close-packed colloidal spheres). Mechanically rigid emulsion droplets would be of interest in the development and manufacturing of highly stable emulsion-based consumer products.

In Chapter 4, we demonstrated the two-step, continuous fabrication of colloidal ellipsoids. The first step continuously cures PS spheres into PVA films, and the second step continuously stretches the spheres and film, at temperatures exceeding their glass-transition temperature, via uniaxial extension between two cylindrical rollers. Using this method, we produced 850 mg of ellipsoids over 16 continuous hours of processing – a production rate of 1.27 g of ellipsoids per 24-hour day. This production rate represents a 20x increase over the best reported quantity yields from traditional batch processing. The increased production rate primarily owes to the rate at which we are able to cure PVA/PS aqueous solution into thin film; our process cured twice as much solution 4.5 times faster than the reported highest-yielding batch process. Our fractional yield is also double that of the best-reported fractional yields, although it is unclear if these reports have been surpassed. These increased production rates make possible comprehensive rheological characterization of minimal gels formed by colloidal

ellipsoids, and also make self-assembly studies with colloidal ellipsoids more rapid and less tedious.

The primary limitation to our process is our inability to achievable aspect ratios beyond 4.32 ± 0.50. Unique phases and unit cells are increasingly accessible as ellipsoids aspect ratio is increased, and it would be desirable to improve this process to achieve as high of aspect ratios as possible. A reasonable target in an aspect ratio of 10, which is achievable via the standard batch synthetic method. This limitation we believe is caused by relaxation of the film and particles at high strains, and thus future work should center around mitigating this relaxation. Possible solutions are some combination of increasing the time that the film is cooled between exiting the oven and reaching the final roller, and rapidly cooling the film as it passes out of the oven, perhaps with a chamber cooled by a dry ice bath.

Finally, increasing the rate of ellipsoid production by an additional order of magnitude would permit comprehensive rheological characterization of minimal gels and dense suspensions of ellipsoids, as well as facilitate more rapid experimental progress in the self-assembly of such ellipsoids. Such production rates could be achieved either by producing particle-embedded film faster (increasing the width capacity of the processing equipment) or by producing film for longer times (making the film production step autonomous or staggering shifts of several operators for several days on end).

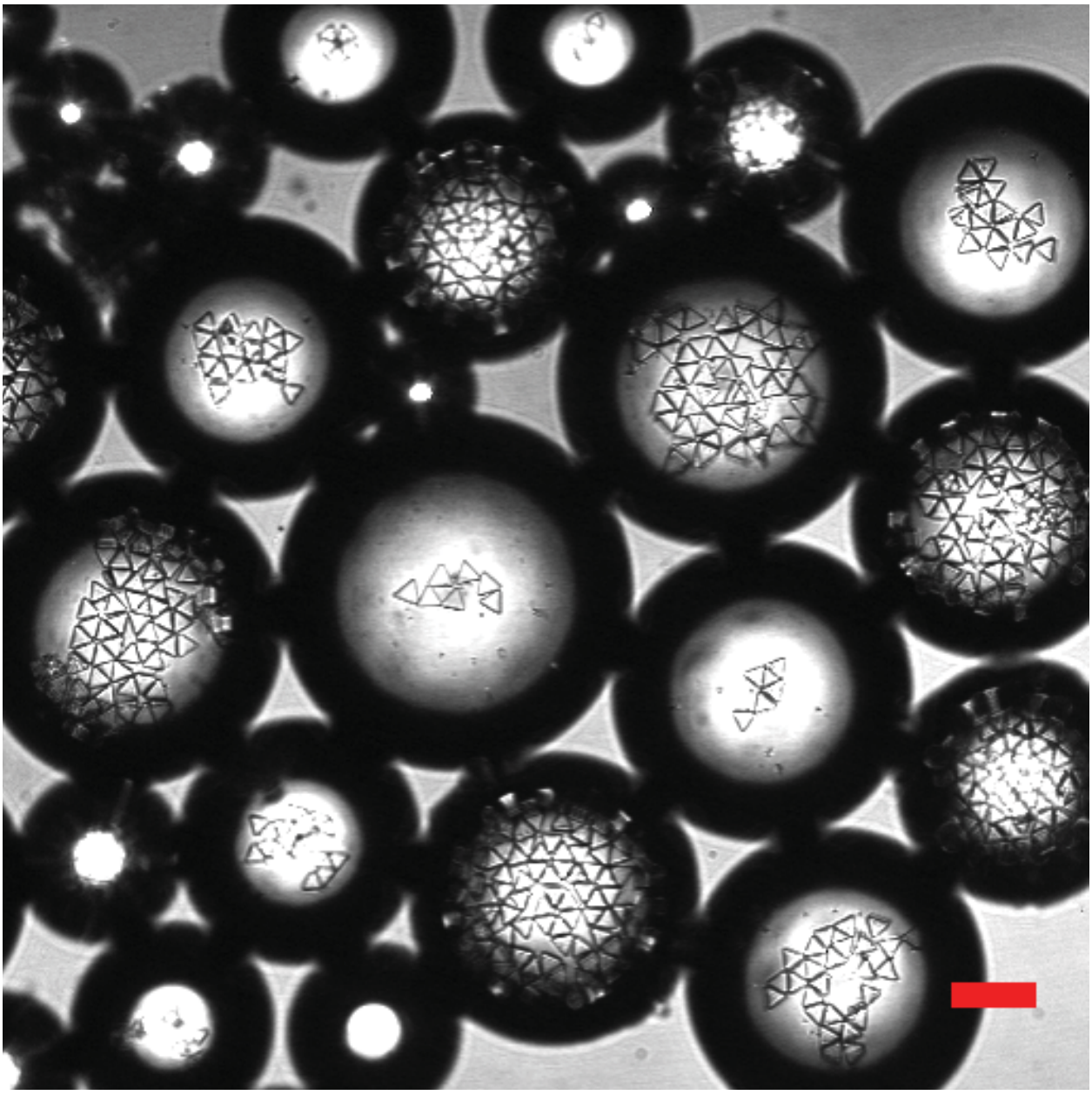

Figure 5-1 (Contributed by Megan Szakasits). Isopropanol-in-oil (CHB/Decalin) emulsion, stabilized by thin, triangular prisms, which adsorb to the droplet interface. The prism edge length (L) is 30 μm, and their thickness (T) is 5 μm. Prisms self-assemble into both close-packed and open structures. Scale bar is 100 μm.

5.1 References

1. Zukoski, I. V., C.F & Saville, D. A. Electrokinetic properties of particles in concentrated suspensions. *Journal of Colloid and Interface Science* **115**, 422-436 (1987).

2. Sun, K., Souslov, A., Mao, X. & Lubensky, T. C. Surface phonons, elastic response, and conformal invariance in twisted kagome lattices. *Proceedings of the National Academy of Sciences* **109**, 12369-12374 (2012).

3. Lewandowski, E. P., Bernate, J. A., Tseng, A., Searson, P. C. & Stebe, K. J. Oriented assembly of anisotropic particles by capillary interactions. *Soft Matter Soft Matter* **5**, 886-890 (2009).

4. Lewandowski, E. P. et al. Orientation and Self-Assembly of Cylindrical Particles by Anisotropic Capillary Interactions. *Langmuir Langmuir* **26**, 15142-15154 (2010).

5. Razavi, S. et al. Collapse of Particle-Laden Interfaces under Compression: Buckling vs Particle Expulsion. *Langmuir Langmuir* **31**, 7764-7775 (2015).

6. Madivala, B., Fransaer, J. & Vermant, J. Self-Assembly and Rheology of Ellipsoidal Particles at Interfaces. *Langmuir Langmuir* **25**, 2718-2728 (2009).

7. Kim, Y. Beyond Equilibrium Assemblies: Applying Light, Flow, and Confinement. *Chemical Engineering* **PhD**, (2016).

Dissertation Errata

Acknowledgements

I would like to thank Leo Pavlovsky, who led the design of the continuous film fabrication device described in Step 1 and an initial iteration of the continuous film stretching device described in Step 2. I would also like to thank Eric Viges, who led the mechanical and electrical design of all equipments described in this chapter, and Yanliang Liu, whose fundamental polymer knowledge was crucial to optimizing the performance of both continuous film fabrication and stretching.